THE UNIVERSITY *of* EDINBURGH

THE UNIVERSITY
of EDINBURGH

Optogenetic manipulation of cellular energetics in *Escherichia coli*

Tommy Schmidlechner

A thesis submitted in fulfilment of the requirements
for the degree of Doctor of Philosophy

May, 2024

Abstract

Optogenetics is a powerful research tool due to the unrivalled spatiotemporal precision and non-invasiveness of light. Proteorhodopsin from SAR86 γ-proteobacterium (PR), a light-driven proton pump, has previously been used to power the swimming of bacteria, showing that the major electrochemical ion gradient of the cell, the proton motive force (PMF), can be controlled optogenetically. But what is the extent of the control we have? My objective is to investigate the optogenetic control of cell physiology and energetics, and study bacterial responses to fluctuations in PMF using PR and other types of microbial rhodopsins.

I introduced a set of microbial rhodopsins to physiologically wild-type *Escherichia coli* strains, characterised their expression and probed the PMF of cell populations under the light control of the successfully expressed microbial rhodopsins. The PMF of the cell has been shown to be proportional to the rotation of the bacterial flagellar motor, which can be detected under a microscope as the spinning of cells tethered to a solid surface via flagella, and as swimming of cell populations, whose average speed can be measured using differential dynamic microscopy.

The expression of the algal and archaeal rhodopsins either caused light-independent growth defects, followed by spontaneous loss-of-function mutations in their genes, or caused no defects, but also lacked any detectable functional expression. Both bacterial rhodopsins, PR and *Parvularcula oceani* xenorhodopsin (PoXeR), display light-dependent PMF control in anaerobic conditions, showing that these outward and inward proton pumps can be used in wild-type cells for optogenetic PMF generation and depletion, respectively. Both are unable to cause

significant light-dependent effects in respiring cells, although they show a light-independent increase in oxygen consumption rate. I also observed various PMF regulatory behaviour in response to changes in the environment. This work charts the use of microbial rhodopsins in bacteria and gives direction for future efforts on optogenetic control of bacterial electrophysiology.

Lay summary

Bacteria are an essential part of our lives. Some make up a part of our body, helping us digest food and protect us from infections, while other bacteria can make us sick. Bacteria are also useful for research about how living organisms work and can be used as microscopic factories for producing medicine, recycling waste and so much more. That is why it is useful to be able to control bacteria, so we can use them to our advantage while preventing them from causing harm.

The most common way to control bacteria is through chemical compounds like antibiotics, sugars, and various drugs. These work well for most purposes, but sometimes the situation requires more finesse. As chemicals in water-based environments, where bacteria typically live, they tend to move around by diffusion, ending in potentially unwanted areas and often making it difficult to remove them afterwards without replacing the entire environment. This is where the growing field known as optogenetics shines.

Optogenetics is a group of techniques where light is used to control a particular function of a cell, such as telling a nerve cell to send a signal or a bacterium to start producing something. Using light, we can control precisely and reversibly when and where something occurs, enabling us to control bacteria in many ways we could not before.

In my project, I studied a group of optogenetic tools known as microbial rhodopsins, which use the energy from light to move ions in and out of the cell. Just like alkaline batteries that use the movement of electrons from one side to the other to power our appliances, cells like bacteria use the movement of ions across the cell membrane to power its functions. Because of this, microbial rhodopsins can use light

to either charge or deplete the energy of the cell. This way of controlling bacteria is still relatively new, and has mainly been used to control their movement using only one type of rhodopsin that charges the cell by pumping protons out of the cell. I created different bacteria to have more types of rhodopsins that can move different ions in different directions and at different speeds. Many of these rhodopsins did not work in my bacteria, and I discuss why this was the case and how to get around it in the future. But with the ones that worked, I further characterised their function in different conditions and used them to learn more about how bacteria regulate their energy. This work supports the development of new optogenetic techniques based on controlling the energy of bacteria.

Declaration

I declare that this thesis has been composed by myself and the work presented is my own except where explicitly stated otherwise. This work has not been submitted for any other degree or professional qualification.

Tommy Schmidlechner

May 18, 2024

Acknowledgements

I would like to thank my supervisors Teuta Pilizota and Luke McNally for their guidance and encouragement throughout my project. I would also like to thank my thesis committee members Helen Alexander and Nick Colegrave for being supportive and involved in my journey. Thanks to Jochen Arlt for the many hours you helped me with DDM and the microscopes, to Patricia Gonzales Iglesias for giving me a space in the lab near the microscope and to Elise Darmon for helping me with lab equipment when in need and checking how I am doing when I no doubt have looked stressed.

Thanks to the current and past members of the Pilizota lab for the good memories, especially for playtesting my prototype boardgame and for our bouldering session. To Lucas Le Nagard thanks for all the help with DDM and the microscope, and for the many interesting discussions. To Smitha Hedge, thanks for helping me get started when I joined the lab and for sharing your expertise with protein purification. To Amritha Janardanan, thanks for always being willing to help with electrical components and such. To Francesca Galdi, thanks for all the help with the bioreactor, for being a good lab bench neighbour and for all the chats.

I would also like to thank my colleagues in Ashworth for the many social gatherings, the graduate school administrative team for solving my every emergency and Daily Dose Of Internet for making my days *just a little better*.

Thanks to the Social Security Scotland Operational Research team for taking me in for an internship where I learned more about the nature of careers in data science and especially to Finlay Noble Chamings for being a great mentor. This

internship was the best part of my journey. I am grateful to Eastbio for funding the internship, and to the School of Biological Sciences for funding my PhD.

To my best friend Juhani, thanks for always being there for me from across the sea, and ready to celebrate New Year and Midsummer whenever I come back, as if I was never gone. You're a true friend.

To my parents Kaija and Richard, thanks for your constant support and interest in whether my "proteins are spinning well". Our weekly game nights, together with my partner and my brothers Jonatan and Christian, kept me going through the week.

Finally, to my wonderful partner Siyao, thank you for all your love, support, and companionship. I could not have done this without you, and now it's my turn to return the favour as you go through this same journey.

Contents

Chapter 1

Introduction

1.1 Motivation

Biological evolution is like a tinkerer who solves random problems using the most powerful existing supercomputer in the world: our planet. Through evolution, our planet creates endless nanomachines to fill biological needs by testing countless configurations of atoms according to the laws of nature. The acquisition of these molecular machines can mean the survival of an endangered species, the death of a patient hosting a pathogen, or be the key to a biotechnological breakthrough. As such, the power to control evolution is a remarkably powerful tool.

To research a particularly interesting evolutionary mechanic known as evolutionary rescue – the rapid genetic adaptation of a population facing extinction (Gonzalez et al, 2013) – studies use changing environments to challenge the survival of typically a fast-replicating micro-organism against a stressor. This is typically done by creating a stress gradient that increases either over time (Lindsey

et al, 2013; Moser & Bell, 2010) or space (Baym et al, 2016; Bisschop et al, 2019). However, environmental stress often varies in both time and space. For example, an antibiotic treatment causes a peak and decay of antibiotic concentrations that may spatially vary from tissue to tissue (Le, 2019). To forgo either the spatial or temporal heterogeneity is to ignore many important biological and evolutionary mechanisms. For instance, if environmental stress does not increase over time, individuals in the permissive environment face no evolutionary pressure while becoming an endless supply of genetic material. If the environmental stress never decreases, non-resistant individuals with potential stress-mitigating mutations do not get enriched for future stress. The existence of refugia requires spatial heterogeneity. Refugia are permissive environments connected to a restrictive environment, and they can establish source-sink systems that increase the amount of genetic material under evolutionary pressure (Perron et al, 2007; Hermsen et al, 2012). Therefore, evolutionary rescue should also be studied in a spatiotemporal model.

Changing environmental stress temporally while ignoring spatial aspects is easy; antibiotics can simply be added to a liquid culture or cells re-introduced to a new medium. To establish spatial patterns and preserve the spatial structure of the evolving population, the stressor must not freely diffuse everywhere and the population cannot be harvested to inhabit a new environment. This often renders the environment impervious to further modification. Recent developments have led to the rapid expansion of the field of optogenetics (Method of the Year, 2010; Wittmann et al, 2020), which makes it possible to control various cellular properties with light and its high spatiotemporal precision. Optogenetic tools have, for example, been used to control the movement of *Escherichia coli* by monopolising its proton motive force (PMF) generation to the light-driven outward proton pump proteorhodopsin (PR;

Walter et al, 2007; Tipping et al, 2012; Arlt et al, 2018; Arlt et al, 2019; Frangipane et al, 2018), enabling spatiotemporal self-assembly of the bacterial cell culture (Figure 1.1).

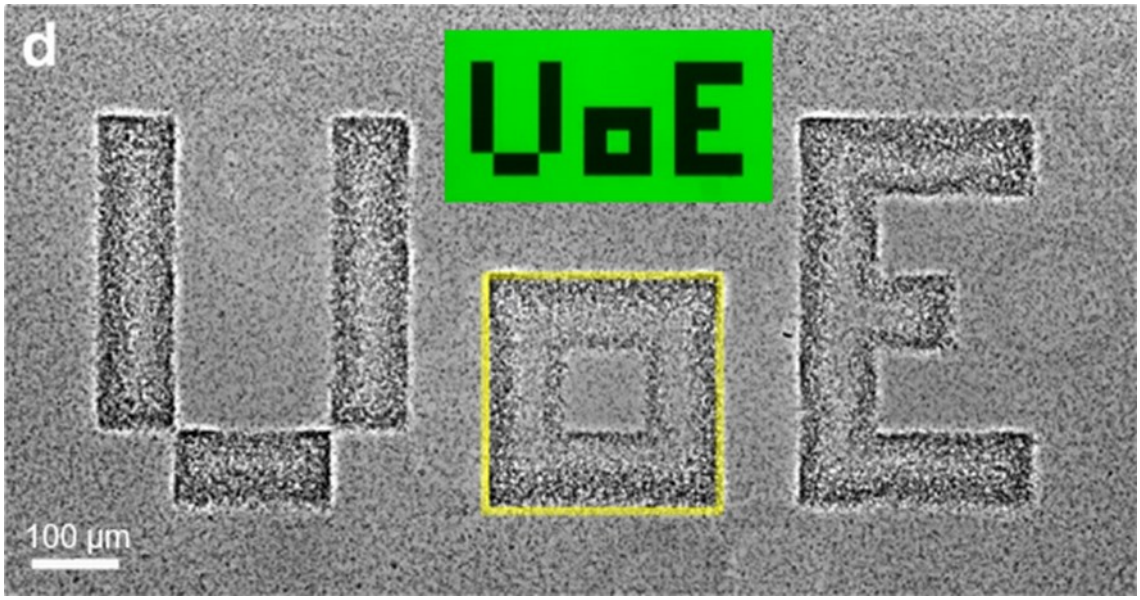

Figure 1.1: Bacteria self-assembling according to a projected light pattern. Nutrient-depleted PR-expressing E. coli are motile only in green light, and so accumulate in areas where no light is projected. Black and green box: the pattern of light projected onto the plate, where green represents green light and black represents no light. Yellow square: the edge of the letter “o” of the light pattern. The picture was taken after 6 minutes of pattern illumination. Modified from Arlt et al (2018).

Besides movement by bacterial flagellar motor (Gabel & Berg, 2003), PMF also drives ATP synthesis by F_1F_o ATP synthase (Berg et al, 2002) and active membrane transport through various transporters (Pinner et al, 1992). Since energy metabolism and membrane transport are crucial components of cell physiology, it may be possible to control aspects of bacterial physiology and thus fitness according to a projected light pattern, allowing us to study evolution under spatiotemporal patterns of environmental stress. Besides this, controlling the physiology of the cell using light has many potential biotechnological uses, such as converting electrical inputs into more types of biological outputs, and controlling the flux of specific ions can give us much insight about cell physiology, such as how the cell regulates and

uses its electrochemical ion gradients. Overall, the pioneering work presented here will make way for many future techniques involving the use of microbial rhodopsins in bacteria.

1.2 Evolutionary rescue

What makes evolutionary rescue particularly important is that, unlike traditional evolution that is often measured in millions of years, evolutionary rescue is involved in many processes occurring within our lifetime, even in days. The most relevant example would be the antimicrobial resistance of pathogens. The emergence of antimicrobial resistant infections occurs when a population of non-resistant pathogens avoids extinction via the selection and establishment of a resistant mutant sub-population, i.e., undergoes evolutionary rescue. The resistant sub-population can either be already present in the population, a concept known as standing genetic variation, or it can emerge during – and facilitated by – the environmental stress. In both cases, the emergence of resistance can occur either by horizontal gene transfer, i.e., the acquisition of genetic information from another organism, or by de novo mutations, which occur during cell division (Cantón & Morosini, 2011). Each process differs in how they lead to evolutionary rescue.

To establish a resistant mutant population, the mutant needs to outcompete the non-resistant population and avoid extinction by random fluctuation. Based on my simulations (Figure 1.2, Table B.1), the extinction probability, p_E of a population can be modelled as

$$p_E = F^{-n_0}$$

where F is the fitness of the population, measured as the ratio of proliferation to death, and n_0 is the initial population size. Based on this, the underlying principle of increasing the probability of evolutionary rescue is to either increase the fitness of the mutant or the initial number of mutants.

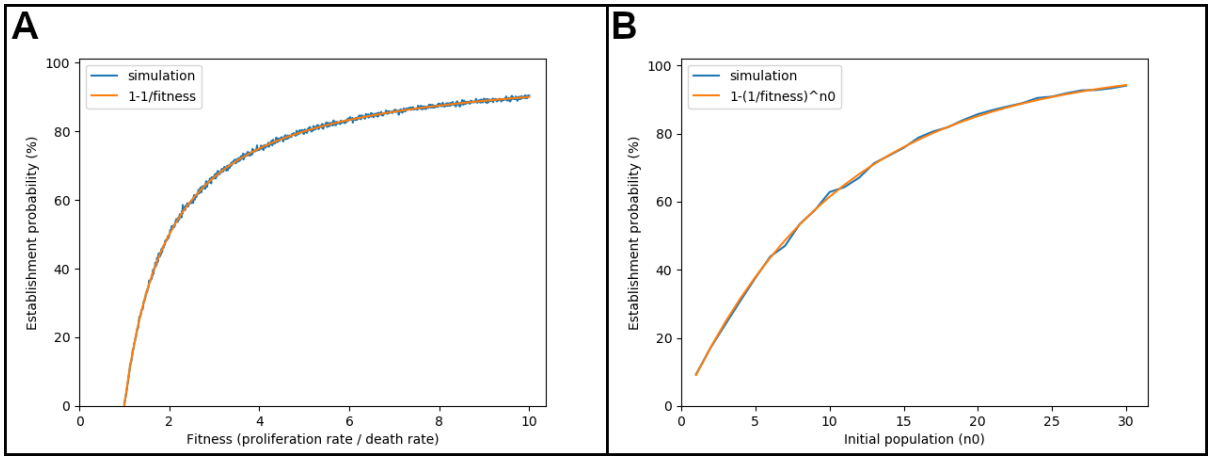

Figure 1.2. The number and fitness of mutants increase the probability of establishing a mutant population. (**A**) A simulation (104 repeats per point) of a single cell reaching a viable population size (100 cells), as a function of fitness, using the Gillespie algorithm. (**B**) A simulation (103 repeats per point) of a population (fitness = 1.1) reaching a viable population size (100 cells), as a function of initial population size, using the Gillespie algorithm.

The initial number of mutants due to standing genetic variation is determined by the equilibrium between the emergence and death of mutants, and population size. Emergence due to horizontal gene transfer largely depends on the presence of other organisms containing resistance genes in the environment. Emergence due to de novo mutations depends on the probability of obtaining a resistance mutation and the mutation rate. The probability of obtaining a resistance mutation depends on the type and magnitude of stress resistance, with a larger magnitude decreasing the probability of emergence (Moser & Bell, 2010). Mutation rate also depends on the environment, as stress increases the mutation rate in bacteria (Frenoy & Bonhoeffer, 2018). Finally, the death of mutants prior to stress largely depends on its competitive fitness against the non-resistant population, which again depends on the type and

magnitude of stress resistance, and the current level of stress. Upon the onset of critical stress, the increased mutation rate accelerates the emergence of mutants, and the mutants' competitive fitness increases to the point where it can attempt to spread, but the total population size starts to shrink towards extinction.

As these factors generally depend on the stress and resistance mechanics, and countless environmental factors involving spatial and temporal variables as described, it is important to have good control of the experimental environment when studying evolutionary rescue. The stressor should be able to be controlled in space, time and intensity. It should be capable of killing non-resistant cells, and an evolutionary path to resistance needs to exist. In this regard, the use of light and microbial rhodopsins can be implemented in a few different ways. The stressor could be the light-driven harmful rhodopsin activity such as opening a proton channel or inward pumping of protons, both resulting in the dissipation of PMF. The path to resistance could involve disabling the rhodopsin or acquiring a mechanism to counter its effect. Conversely, the stressor could be the light itself, which has been shown to be able to damage the cell membrane in aerobic conditions, resulting in a reduction in PMF (Krasnopeeva et al, 2019). Resistance to this could be through the repair of an inactivated gene of a beneficial rhodopsin such as the PMF-generating proteorhodopsin. These two approaches could also be used in combination by using rhodopsins with sufficiently distinct action spectra. The advantage of using a beneficial rhodopsin, however, is that it may be too easy to disable a single deleterious gene to become resistant, whereas the difficulty of repairing a disabled beneficial gene can be adjusted by the choice of mutations. This method may even allow us to design a variable level of resistance by requiring multiple mutations to restore full activity.

1.3 Cell energetics

At the center of *E. coli* energetics, PMF and ATP are key players powering various cellular processes. PMF is the electrochemical potential of protons across the cell membrane. This potential is the sum of two components, the concentration difference of protons and the electrostatic potential across the membrane, and can be described as

$$PMF = V_m + \frac{RT}{F}\ln\left(\frac{[H^+{}_{in}]}{[H^+{}_{out}]}\right)$$

where V_m is the membrane potential, R is the ideal gas constant, T is temperature, F is the Faraday constant and $[H^+]$ is the concentration of protons in and out of the cytoplasm. In 25°C, this can be simplified to

$$PMF = V_m - 59\ \Delta pH$$

where $\Delta pH = pH_{in} - pH_{out}$, showing that in neutral pH conditions, PMF mainly consists of membrane potential. Although this work will focus on proton motive force, the electrochemical potential of other ions can also play key roles, for example, in *Vibrio alginolyticus*, the synthesis of ATP is powered by sodium motive force instead of PMF (Dibrov et al, 1986).

Much like the movement of water through a dam, the movement of protons through the cell membrane due to PMF is harnessed by various molecular machines to power an otherwise energetically unfavourable action. As this potential difference exists across the cell membrane, its energy can be accessed by membrane proteins such as F_1F_o ATP synthase (Berg et al, 2002), bacterial flagellar motor (Gabel & Berg, 2003) and various membrane transport proteins (Pinner et al, 1992). ATP, on

the other hand, stores energy in its chemical bonds, and just like firewood, can be used to fuel reactions wherever it goes.

To generate and maintain a PMF, *E. coli* is thought to use proton antiporters to export other cations to increase the electric component of PMF while cycling protons in and out (Terradot et al, 2021). Hence, while the chemical component of PMF often contributes little to PMF, it is the export of protons that ultimately powers PMF. In aerobic conditions, the electron transport chain couples a chain of redox reactions, from higher to lower energy intermediates, to the outward pumping of protons. As mentioned, this electrochemical gradient is then largely used to power the ATP synthesis of F_1F_o ATP synthase. In anaerobic conditions, to compensate the absence of proton pumping by the electron transport chain, the function of F_1F_o ATP synthase is reversed such that it consumes ATP to pump protons out (West & Mitchell, 1974). Instead, the role of ATP production shifts to substrate-level reactions such as glycolysis. Further, as proton pumping by F_1F_o ATP synthase alone is insufficient, other processes such as the extrusion of fermentation end products (Michels et al, 1979) and hydrogen cycling (Trchounian et al, 2012) contribute to PMF maintenance.

Given the ability of F_1F_o ATP synthase to convert between ATP and PMF, these two energy forms are closely linked. Since ATP and ADP compete for the active site of F_1F_o ATP synthase, ATP synthesis in the high ATP and PMF conditions of a growing cell occurs at only 20% of its maximum rate (Meyrat & von Ballmoos, 2019), giving the homeostatic system the ability to increase its PMF consumption for ATP synthesis in addition to its ability to reverse the reaction. ATP homeostasis is one of the most stably regulated homeostatic systems, with population ATP concentrations remaining constant across a wide range of conditions and growth

rates (Figure 1.3 A & B; Radoš et al, 2022; Schneider & Gourse, 2004). Despite the tight regulation, ATP concentration varies significantly at different growth stages, being subject to a significant reduction during lag and stationary phase compared to exponential phase (Figure 1.3 C; Deng et al, 2021). Furthermore, ATP concentration in single cells undergoes significant fluctuation even during exponential growth (Figure 1.3 D), and a stable ATP concentration positively correlates with growth rate during individual cell cycles (Figure 1.3 E; Lin & Jacobs-Wagner, 2022), highlighting the importance of ATP homeostasis. It is worth noting that Lin & Jacobs-Wagner (2022) used the QUEEN ATP sensor, which has been shown to undergo changes, likely photoactivation, during time series imaging (Mancini & Pilizota, 2023). However, they ensured that the mean and SD of ATP measurements remained stable throughout the experiment, among other control experiments, meaning the observed ATP fluctuations were genuine.

So far, I have talked about cell energetics in respiring and fermenting cells, but when the cell is starved of nutrients such as amino acids, fatty acids or carbon, such as when entering stationary phase (Mouery et al, 2006), it undergoes significant physiological changes through a ubiquitous stress response known as the stringent response (Irving et al, 2020). When the cell is starved of nutrients, various enzymes get activated and start generating the nucleotide messengers pGpp, ppGpp and pppGpp by transferring a pyrophosphate group (PPi) from ATP (leaving behind AMP) to guanosine mono-, di- and triphosphate (GMP, GDP and GTP), respectively. For example, the stringent response enzyme RelA activates when bound to stalled ribosomes (Loveland et al, 2016), and is further stabilised by the subsequent binding of an uncharged tRNA (Kudrin et al, 2018). The resulting messengers, mainly ppGpp in *E. coli*, then affect a wide range of cell functions with

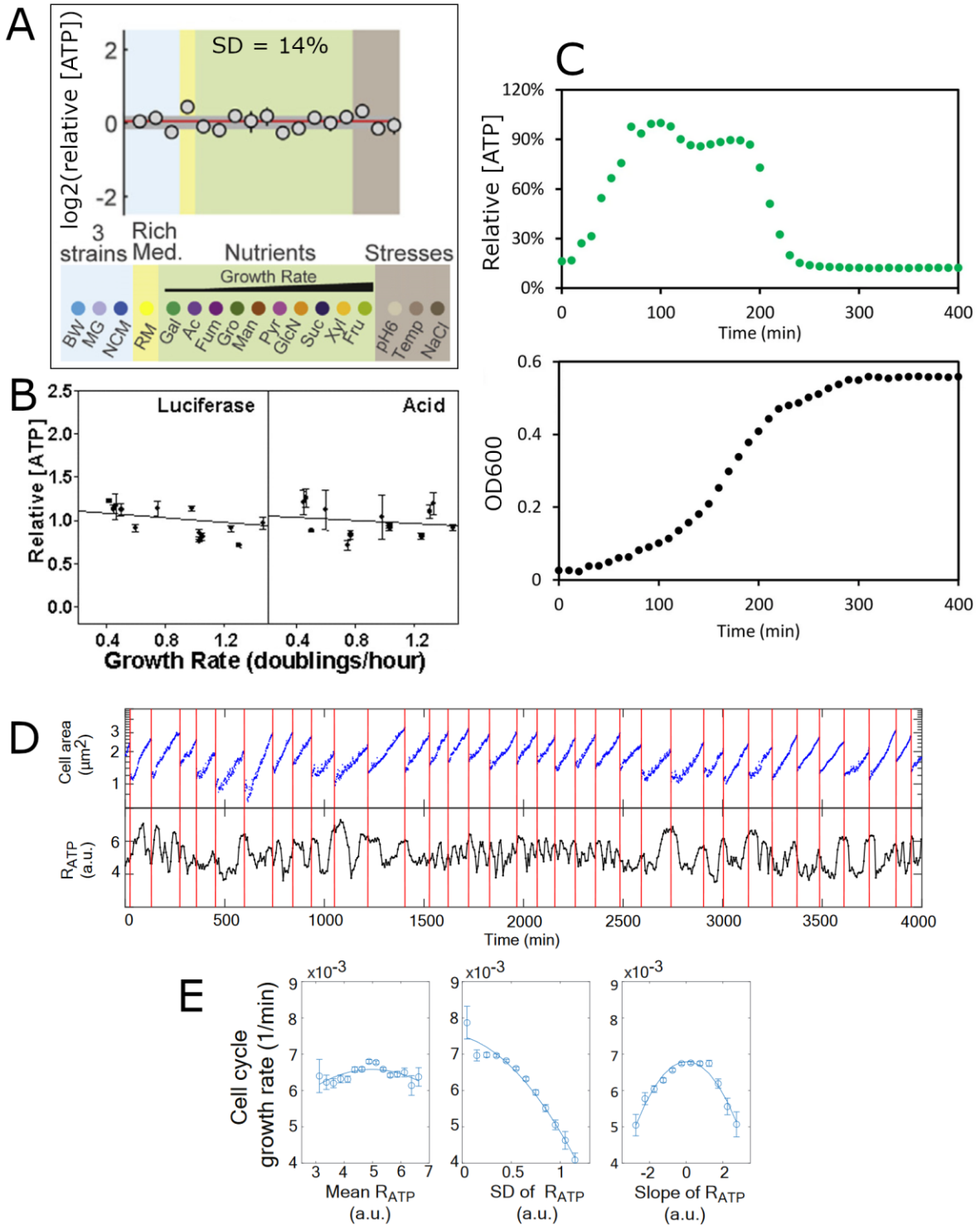

Figure 1.3: ATP homeostasis is important for cell growth. (**A**) ATP is one of the least varying metabolites on a population level, having only a 14% SD variation, relative to mean, across a wide range of conditions at exponential growth. Adapted from Radoš et al (2022). (**B**) Population level ATP concentration is stable across a wide range of growth rates, measured using two different methods. Adapted from Schneider & Gourse (2004). (**C**) Population level ATP concentration (top) depends on growth phase (growth curve on bottom). Adapted from Deng et al (2021). (**D**) Single-cell ATP concentration fluctuates with cell cycle and faster,

unknown processes. (**E**) Mean ATP concentration in single cells does not significantly affect their individual growth rate (left), but ATP fluctuation negatively correlates with growth rate (middle), whether the concentration is increasing or decreasing (right). D & E adapted from Lin & Jacobs-Wagner (2022).

the general effect of inhibiting cell growth, slowing down metabolism and steering gene expression towards nutrient uptake and biosynthesis (Irving et al, 2020). Crucially, the stringent response reduces ATP synthesis (Wang et al, 2019) and PMF (Verstraeten et al, 2015; Smirnova et al, 2018), which may play a role during my experiments, where cells occasionally experience nutrient limitation.

Considering the many ways ATP and PMF are regulated, it is difficult to predict how the optogenetic manipulation of just PMF or a different ion motive force affects ATP concentration and other physiological parameters, since they are all interconnected (Terradot et al, 2021), and the balance between each parameter will depend on how important it is to keep them at given levels in given conditions. This is why the optogenetic control of the wider cell physiology requires pioneering studies, such as this work, to chart the way and understand how cells respond to the optogenetic manipulation of ion gradients in different conditions.

1.4 Microbial rhodopsins

Rhodopsins are a family of membrane proteins that share a characteristic 7-transmembrane helix structure and bind a chromophore known as retinal. The photoisomerisation of retinal, powered by the absorption of light, leads to conformational changes in the rhodopsin, which drive a cycle of distinct protein states and result in the specific activity of a given rhodopsin. While microbial and animal rhodopsins share the main characteristics of protein structure and light-sensitivity, they have evolved distinctively different functions (Kojima & Sudo, 2023).

The physiological roles of microbial rhodopsins are not fully understood, but they are known to be able to support phototaxis (Foster et al, 1984) and phototrophy (Béjà et al, 2000).

Despite the structural similarities between different rhodopsins, subtle differences determine whether these conformational changes result in signal transduction (Royant et al, 2001), ion pumping (Béjà et al, 2000) or the opening of an ion channel (Deisseroth & Hegemann, 2017). Due to their ability to alter the membrane potential of the cell, the light-driven ion pumps and channels were quickly utilised to study neural signalling in eukaryotes (Nagel et al, 2005). Once shown that they have potential for more than just modulating cell signalling, microbial rhodopsins have been used to generate PMF in prokaryotes, mainly to control their motility (Walter et al, 2007; Tipping et al, 2012; Arlt et al, 2018; Arlt et al, 2019; Frangipane et al, 2018), but also for other purposes such as increasing the production of biohydrogen (Kuniyoshi et al, 2015). However, there is still much to learn about the utility of microbial rhodopsins in bacteria, especially considering that most studies exclusively use PR among the different types of rhodopsins, and others focus on studying the molecular mechanisms of the rhodopsins themselves rather than how they can be used to control bacteria. Studying the use of various microbial rhodopsins with the focus on cell energetics and physiology will enable many new ways of controlling bacteria.

Looking closer at light-driven ion pumps and channels, the advantage of an ion channel is that, for a single photocycle, there is no set limit of how many ions can cross the membrane while the channel is open (Figure 1.4), making them more effective at passing ions than a pump that moves one ion per photocycle (Figure 1.5). In return, a channel only allows ions to move along the electrochemical

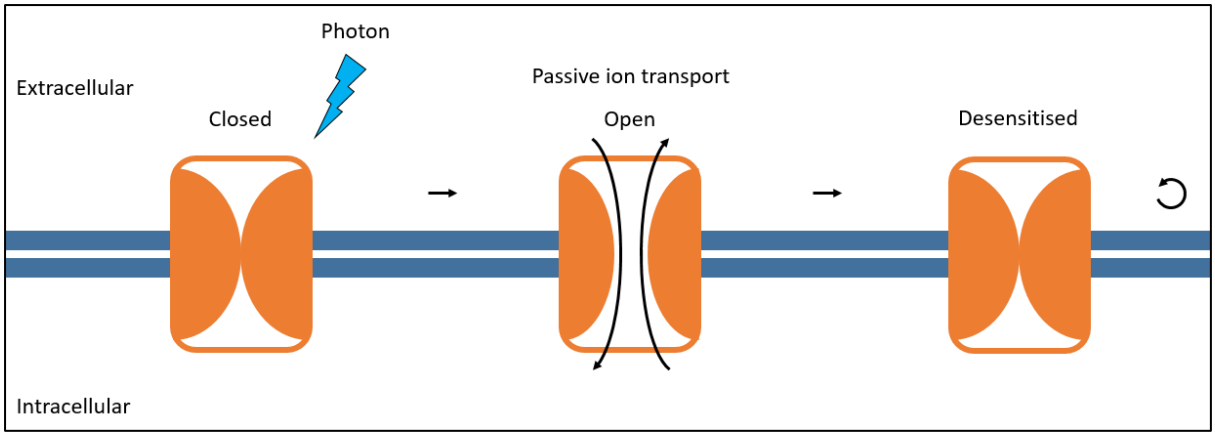

Figure 1.4: Three-state model of channelrhodopsin photocycle. The absorption of a photon opens the channel for a certain duration, allowing the passive transport of specific ions. After the channel closes, the rhodopsin enters a closed state where it is insensitive to light, before returning to the sensitive closed state. Figure based on Nagel et al (2003).

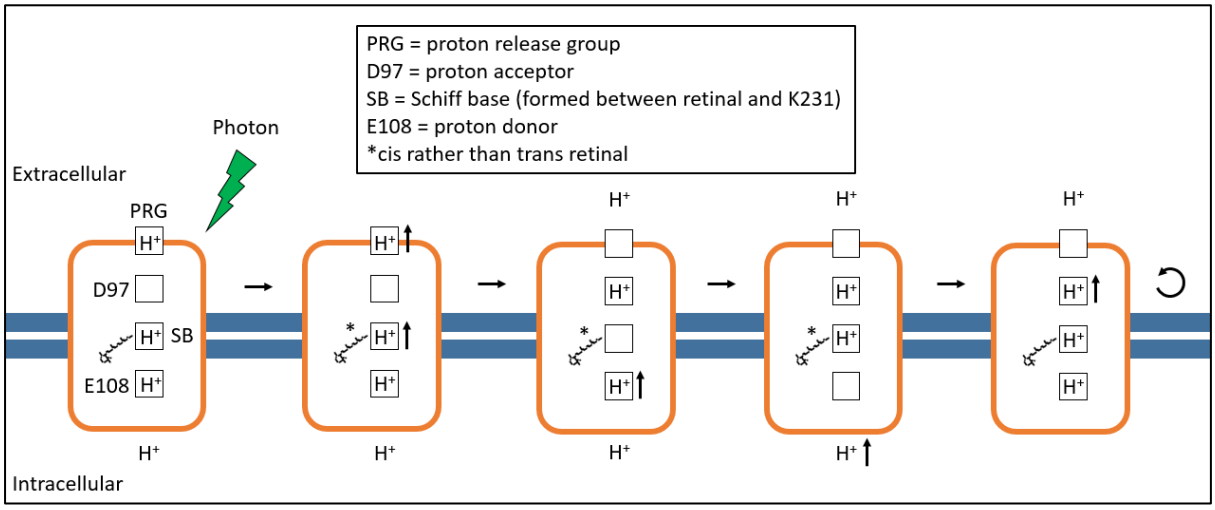

Figure 1.5: A Model of proteorhodopsin photocycle. The absorption of a photon at ground state causes the photoisomerisation of the bound retinal, resulting in an intermediate state known as K-state. This high-energy state then undergoes multiple relaxation steps to revert to ground state and resulting in the active transport of a proton. In M-state, the proton release group and the Schiff base have released a proton to extracellular space and a proton-accepting residue, respectively. In N-state, a proton-donating residue re-protonates the Schiff base, and O-state re-protonates the proton donor using an intracellular proton. Finally, the relaxation to ground state results in the deprotonation of the proton acceptor resulting in the initial configuration. The boxes in the figure represent residues that can be protonated or deprotonated and the upward arrows represent the movement of protons resulting from entering the next state. Figure based on Bamann et al (2014).

gradient, while a pump can transport ions against the gradient. Further, light-driven ion channels are less selective than pumps, generally being permeable to multiple types of anions or cations. In contrast, light-driven ion pumps generally transport ions by a series of reactions, forming a covalent bond with the transported ion at each intermediate state of the cycle (Figure 1.5), thus being more selective about which ions can pass through. Subtle amino acid differences can influence the stability of the photocycle intermediates, potentially affecting the dynamics of the cycle, the direction of pumping, the target ion, the absorption of light or even the conversion of a pump into a channel. As such, the natural variety in the biophysical characteristics of different microbial rhodopsins offers a great amount of choice for characteristics.

With the goal to achieve various control of cell energetics and physiology, we can utilise the many different biophysical characteristics of microbial rhodopsins to attempt this from many angles. First, to impose negative effects on cell energetics, the most effective way ought to be to permanently open an ion channel that can quickly deplete electrochemical ion gradients and membrane potential (Kühlbrandt, 2016). Due to the negative effects of long-term opening of ion channels, it is safe to assume that the natural function of these channelrhodopsins is to create transient signals, which also aligns with their use of modulating action potential generation in electrophysiological studies. However, since our goal is not to control cell signalling, but cell energetics by long-term ion channel opening, a standard channelrhodopsin may not be suitable. Therefore, I have chosen ChEF, a chimeric cation-conducting channelrhodopsin with an increased steady-state conductance that can remain more effective over long time periods (Lin et al, 2009). To achieve a more modest effect and with a higher certainty, I chose PoXeR, an inward proton pump that has already been expressed in *E. coli*.

To achieve the opposite effect, I chose to use PR, the well-characterised outward proton pump that has already been expressed in *E. coli* and used to generate a PMF to power the bacterial flagellar motor (Walter et al, 2007; Arlt et al, 2018). However, there is still more to learn about the potential of PR to control other aspects of cell physiology, such as its metabolism or growth rate. A different way to potentially achieve a positive effect on cell energetics is to pump negatively charged ions into the cell, producing a more negative membrane potential. As this only affects the electrical and not chemical component of PMF, it may behave differently from PR and reveal more information about the interplay between the homeostasis of membrane potential and PMF. Hence, I chose NpHR, a well-known inward chloride pump. To enable simultaneous control of two types of microbial rhodopsins, we can utilise rhodopsins that absorb light at the ends of the visible spectrum, especially on the red end due to the damaging property of short wavelengths. If there is poor or no overlap between the action spectra of two rhodopsins, it is possible to activate one without activating the other. For this, I chose ArchT, ChIEF and Chrimson. Like PR, ArchT is an outward proton pump, but with a red-shifted absorption spectrum. Chrimson is another cation channel but with a strongly red-shifted absorption spectrum. Lastly, ChIEF is nearly identical to ChEF, but a single amino acid change results in a narrower but blue-shifted absorption spectrum, reducing overlap with the absorption spectra of other rhodopsins. All this is summarised in Table 1.1.

Table 1.1: A summary of microbial rhodopsins used in this work.

Rhodopsin	Function	Absorption peak	Advantage
PR	Outward H^+ pump	525 nm	Well characterised
PoXeR	Inward H^+ pump	560 nm	Inward H^+ pump
ArchT	Outward H^+ pump	570 nm	Red-shifted absorption spectrum
NpHR	Inward Cl^- pump	575 nm	Cl^- pump
ChEF	Cation channel	490 nm	Improved steady-state conductance
ChIEF	Cation channel	450 nm	Narrow absorption spectrum
Chrimson	Cation channel	590 nm	Red-shifted absorption spectrum

1.5 Overview

With the purpose of developing optogenetic tools to study and control cell energetics, physiology and fitness, the aim of this work is to characterise the expression of different microbial rhodopsins in wild-type *E. coli* and their effect on the wider cell physiology.

In Chapter 2: “Materials and Methods”, I describe the techniques I used and developed, including standard molecular biology methods, cell cultures, protein expression experiments, motility measurement and data analysis.

In Chapter 3: “Expressing microbial rhodopsins in *E. coli*”, I present some unexpected biological processes encountered while creating the genetic constructs, and detail the success and effects of expressing each of the microbial rhodopsins in

this work. The chapter ends with a discussion on exogenous protein expression, the potential reasons behind failed rhodopsin expression and strategies to express rhodopsins with the desired biophysical characteristics.

In Chapter 4: “Optogenetic manipulation of cellular energetics”, I first describe the experimental requirements for measuring the motility of cells under optogenetic PMF control. This is followed by the various findings about cell physiology during optogenetic PMF manipulation and a discussion on the potential mechanisms behind these observations.

The initial plan was to follow Chapter 4 with evolutionary rescue experiments utilising the spatiotemporal control achieved by the optogenetic manipulation of cell fitness. However, this proved more work than could be achieved in one PhD project.

The thesis ends in Chapter 5: “Conclusions and future work”, where I summarise the main points and propose directions for future pioneering work.

Chapter 2

Materials and Methods

2.1 Strains, media and plasmids

2.1.1 Strains

For experiments measuring swimming speed using differential dynamic microscopy (DDM), I used the common wild-type *E. coli* K-12 (*F- λ- ilvG- rfb-50 rph-1*) laboratory strain MG1655 (Guyer et al, 1981). For tethered cell assay, which measures the rotation speed of bacteria tethered to a glass slide via flagella, I used the MG1655 derivate EK01, where the fliC gene has been replaced by $fliC^{sticky}$, causing the flagellar filament to stick to the slide (Krasnopeeva et al, 2019). For plasmid construction, I used NEB 5-alpha (*fhuA2Δ(argF-lacZ)U169 phoA glnV44 Φ80Δ(lacZ)M15 gyrA96 recA1 relA1 endA1 thi-1 hsdR17*), a commercial derivative of the commonly used *E. coli* K-12 cloning strain DH5α.

2.1.2 Buffers and media

To grow cells for DDM experiments, I used MOPS minimal medium (Neidhardt et al, 1974) without micronutrients, supplemented with 0.3% (w/v) glucose, 2% (w/v) casamino acids, 10 μM all-trans retinal and 50 μg/mL kanamycin. For DDM and tethered cell assay, I suspended cells in Berg's motility buffer (BMB), containing 6.2 mM K_2HPO_4, 3.8 mM KH_2PO_4, 67 mM NaCl and 0.1 mM EDTA, supplemented with 0–20 mM glucose.

To grow cells for plasmid construction, I used Lysogeny broth (LB), containing 1% (w/v) tryptone, 1% (w/v) NaCl and 0.5% (w/v) yeast extract, supplemented with either 50 μg/mL kanamycin or 100 μg/mL ampicillin, based on the selection marker of the plasmid. To grow cells for SDS-PAGE, I also added 10 μM all-trans retinal.

To prepare cells for SDS-PAGE and measuring absorption spectra, I used RIPA buffer containing 150 mM NaCl, 1% (v/v) Triton X-100, 0.5% (w/v) sodium deoxycholate and 0.1% (w/v) SDS, and HEPES buffer containing 50 mM HEPES, 200 mM KCl and 1 mM $MgCl_2$.

To test optimal growth conditions for motility and rhodopsin expression, I used the aforementioned MOPS minimal medium and LB, as well as Tryptone broth (TB), containing 1% (w/v) tryptone and 0.5% (w/v) NaCl, M63 minimal medium (Scott et al, 2010), containing 0.1 M KH_2PO_4, 0.5 mg/L $FeSO_4 \cdot 7H_2O$, 0.5 g/L $MgSO_4 \cdot 7H_2O$, 1 mg/L thiamine and 20 mM $(NH_4)_2SO_4$ adjusted to pH 7 and supplemented with 0.5% (w/v) of either glucose or glycerol, and EZ Rich Defined Medium (RDM; Neidhardt et al, 1974) supplemented with 0.3% (w/v) glucose. All of these also contain 10 μM all-trans retinal and 50 μg/mL kanamycin if not already mentioned.

For agarose gel electrophoresis, I used TAE buffer containing 40 mM Tris base, 20 mM acetic acid and 1 mM EDTA.

2.1.3 Plasmid construction

To express microbial rhodopsins in *E. coli*, I decided to use the plasmid pWR20, with a strong constitutive cytochrome C oxidase promoter from *Vibrio Harveyi* and the low-copy-number origin of replication p15A, as the expression vector (Pilizota & Shaevitz, 2012). I used a low-copy-number plasmid to protect the cells from the strain of exogenous protein overexpression such as resource overload (Moriya, 2015) and inclusion body formation (Jhamb & Sahoo, 2012). The constitutive promoter is useful because I want the cells to always express their rhodopsin, whose light-dependent activity can be controlled by the presence of the retinal chromophore and illumination instead of an inducer. However, I did not consider the light-independent effects of rhodopsins, which I will describe in the coming chapters.

To construct the plasmids, I replaced the GFP gene in pWR20 with the microbial rhodopsin genes in Table 2.1. The GFP gene was flanked by NdeI and BamHI restriction sites, so I added the same sites at the ends of each rhodopsin gene, using PCR, as primer overhangs by appending them in front of the corresponding primers. According to the manufacturer, cleavage with NdeI and BamHI-HF (NEB, USA) at the end of a DNA fragment requires the restriction site to be flanked by at least 3 extra base pairs, so I also included those in the overhang. Some of the rhodopsins were also missing start and stop codons, which I again added in the overhang. Finally, because some of the ends of the rhodopsin genes were very GC-rich, which would lead to the formation of primer secondary structures

that block annealing, I sometimes had to move the annealing site further away from the end and include the end of the gene in the overhang by introducing silent mutations that interfere with excessive annealing and secondary structure formation while retain the amino acid sequence of the protein. The resulting primers are listed in Table A.1 and illustrated in Figure 2.1.

Table 2.1: The origin of microbial rhodopsins used in this work.

Rhodopsin	**Plasmid**	**Source**
PR	pBAD-PR	Gift from Jessica Walter (Walter et al, 2007)
PoXeR	pET21a-PoXeR	Gift from Hideki Kandori (Inoue et al, 2016)
ArchT	pMSCV-ArchT-GFP	Addgene plasmid # 86536 (Zhuo et al, 2016)
NpHR	ChR2-2A-Halo	Addgene plasmid # 22047 (Han et al, 2009)
ChEF	AAV-oChEF-citrine	Addgene plasmid # 50975 (Lin et al, 2009)
ChIEF	AAV-oChIEF-tdTomato	Addgene plasmid # 50977 (Lin et al, 2009)
Chrimson	pAAV-CaMKII-Chrimson-GFP	Addgene plasmid # 62718 (Klapoetke et al, 2014)

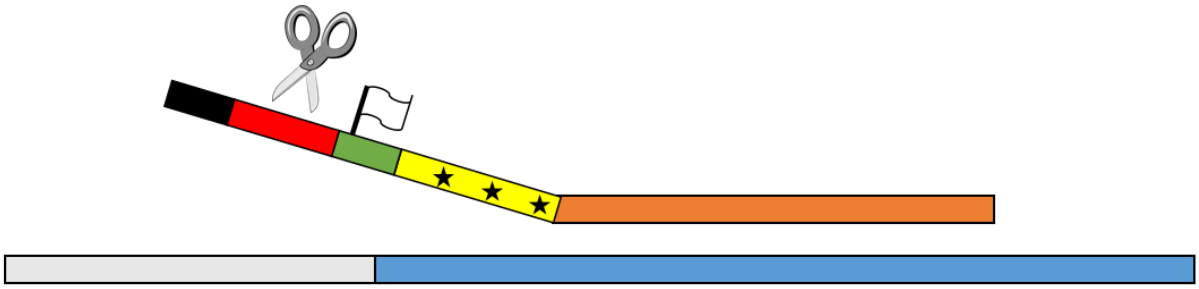

Figure 2.1: Primer design for editing and amplifying rhodopsin gene fragments. Bottom strand (plasmid template), from left to right: sequence before or after a rhodopsin gene (grey), the rhodopsin gene (blue). Top strand (primer), from left to right: extra bases required for cleavage (black), restriction site (red, scissors), start or stop codon if required (green, flag), silent mutations if required (yellow, stars), ~20 base complementary sequence for annealing (orange).

I created rhodopsin gene and pWR20 backbone DNA fragments using Phusion High-Fidelity DNA Polymerase (NEB, USA) according to the manufacturer's protocol in a 50 µL reaction using the provided HF buffer for pWR20, and GC buffer and DMSO for rhodopsins. I ran the PCR for 25 cycles with a 10-second melting and annealing time, annealing temperatures as detailed in Table A.1 and an extension time of 30 seconds. For pWR20, I used a 15-second annealing and 90-second extension time. I then purified the genes by separating them on a 0.8% agarose gel using electrophoresis, cutting the gel containing the genes and extracted the genes using Monarch DNA Gel Extraction Kit (NEB, USA) according to the manufacturer's protocol. Then, I digested these and whole pWR20 plasmids with NdeI and BamHI-HF (NEB, USA) according to manufacturer's protocol and purified the DNA fragments on a gel as before. This causes the ends of the backbone and fragments to have complementary single-strand overhangs that facilitate ligation. Finally, I ligated the gene fragments with pWR20 backbone using T4 DNA Ligase (NEB, USA) according to manufacturer's protocol using a 3:1 fragment to backbone molar ratio and transformed the product into NEB 5-alpha competent cells (NEB, USA) according to manufacturer's protocol.

2.1.4 Plasmid preparation

To prepare plasmids from liquid overnight cultures, I first used Zyppy Plasmid Miniprep Kit (Zymo Research, USA) according to manufacturer's protocol. This, however, resulted in poor yields, absorption spectra that do not match that of pure DNA, and often a white pellet at the bottom of the tube (Figure 2.2 A). After extensive testing and no apparent pattern for the cause of these, I switched to a

newly purchased QIAprep Spin Miniprep Kit (QIAGEN, Netherlands). The plasmids extracted using the new kit, following the manufacturer's protocol, were of expected quality and quantity (Figure 2.2 B), meaning that the old kit had most likely expired. The same happened with the gel extraction kit.

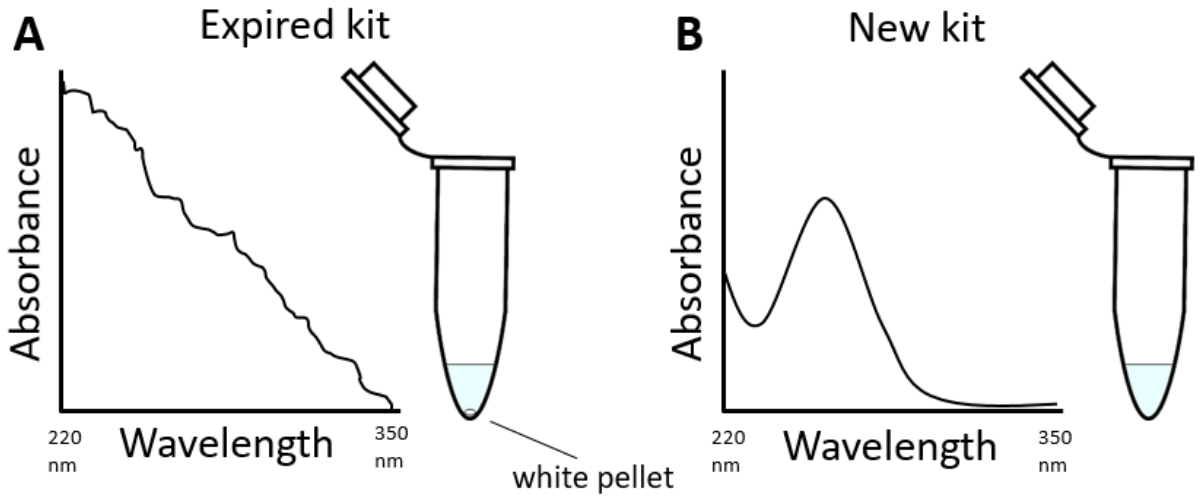

Figure 2.2: An illustrative description of the yield from two different plasmid extraction kits. (**A**) The absorption spectrum of the plasmid extracted with an expired kit is uncharacteristic of DNA absorption. The flow-through after eluting the plasmid from the spin column contains a white pellet, likely made of the material from the column. (**B**) The absorption spectrum with a new kit is characteristic of DNA absorption, and the flow-through has no unexpected pellet.

2.1.5 Colony PCR

To test if individual colonies contain rhodopsin genes, I performed colony PCR with one primer binding to the pWR20 backbone and one to each specific rhodopsin gene; if the gene was present, a PCR product would be formed and can be seen on an agarose gel. First, I picked individual colonies with a pipette tip and resuspended in 20 µL nuclease-free water. I used 5 µL of this to start a liquid culture in LB and boiled the remaining 15 µL in 98°C for 10 minutes to use the colony as a PCR template. I then used 2 µL of this template together with 5 pmol of each primer

(Table A.1) in a 25 µL reaction with Taq 2X Master Mix (NEB, USA) for 30 cycles of 20 seconds in 95°C, 20 seconds in 49°C and 60 seconds in 68°C.

2.1.6 Agarose gel electrophoresis

To prepare a gel for separating DNA, I dissolved 0.8% agarose powder in TAE buffer by heating in a microwave and periodically mixing the solution until dissolved. Once the temperature of the molten gel had cooled down to 50°C, I added SafeView Nucleic Acid Stain (Applied Biological Materials, Canada) to 1X concentration and poured the gel into a mould until solidified. I then submerged the gel in TAE buffer in a gel electrophoresis unit, loaded the gel with a size reference ladder and samples mixed with Gel Loading Dye, Purple (6X) (NEB, USA), and applied 100 V through the gel for 60 minutes.

I noticed that my DNA bands were quite faint, especially at lower size bands, so I conducted some further experiments and found that the SafeView stain migrates through the gel in the opposite direction compared to DNA (Figure 2.3 C). I then compared SafeView with GelGreen Nucleic Acid Stain (Biotium, USA) and found several key differences between the two stains (Figure 2.3 A). Firstly, SafeView is much less sensitive than GelGreen, which can be at least partly explained by the migration behaviour. SafeView also has significant fluorescence when not bound to DNA, which increases the background signal and makes it harder to detect faint DNA bands (Figure 2.3 A & C). Meanwhile, GelGreen fluoresces when bound to DNA while self-quenching in its absence, giving it a good signal-to-background ratio (Mao & Leung, 2015). I also noticed a UV shadow that can be attributed to the interaction between SafeView and Gel Loading Dye, Purple (Figure 2.3 A), which can hide the fluorescence of DNA bands.

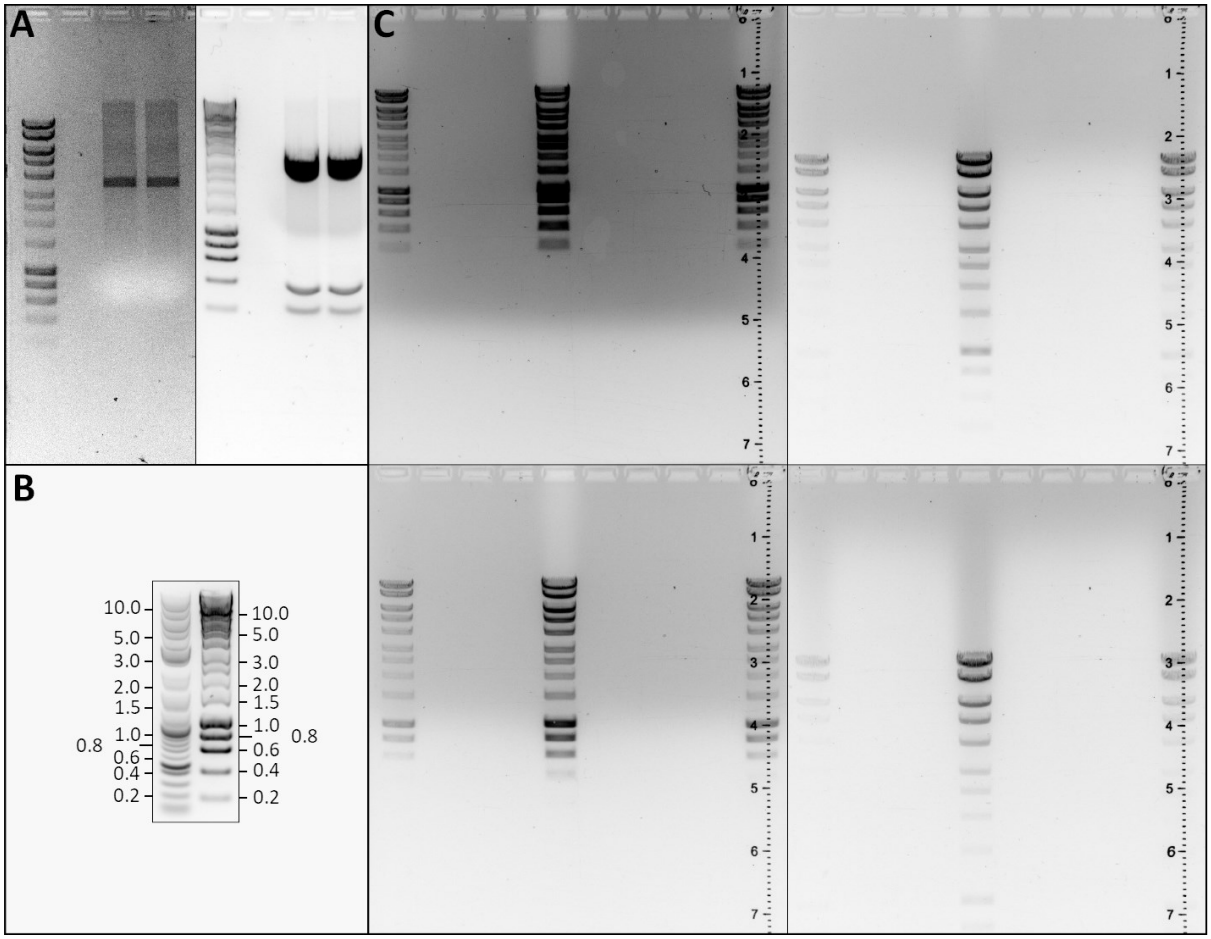

Figure 2.3: A comparison of SafeView and GelGreen nucleic acid stains. (**A**) 1 µg of BamHI-HF & NdeI digested pWR20 split into two lanes, accompanied with 5 µL (left) or 2.5 µL (right) HyperLadder 1kb (Meridian, USA). Left: gel stained with SafeView has poor sensitivity, high background signal and a UV shadow (white in the image). Right: gel stained with GelGreen has good sensitivity and low background signal, but irregular band shapes. (**B**) 5 µL QuickLoad 1 kb Plus DNA Ladder (left; NEB, USA) and 5 µL HyperLadder (right) were run simultaneously on a gel stained with GelGreen – bands of the same size have inconsistent migration distances. (**C**) 3 µL, 10 µL and 5 µL (from left to right) of HyperLadder was ran on a gel stained with SafeView. Top left, 30 minutes: the gel has been depleted of SafeView from 5 cm onwards and from where the DNA has migrated through. Bottom left, 45 minutes: the depletion zone has advanced to the 4 cm mark. Top right, 60 minutes: SafeView has been depleted from 2 cm onwards, and the smaller bands have become faint. Bottom right, 75 minutes: SafeView has been depleted from 1 cm onwards and can be seen leaving the DNA bands as the DNA leaves behind a receding trail of fluorescence. Most bands have lost most of their stain.

While GelGreen had superior sensitivity, it does have its own drawbacks. Firstly, the DNA bands with GelGreen have more irregular shapes (Figure 2.3 A & B), which can make it harder to determine the migration distance of the DNA band. More importantly, due to the large size that makes GelGreen non-permeable to cell membranes, it causes significant DNA concentration-dependent band shifts that also make it harder to estimate the size of the DNA bands (Figure 2.3 B). Both drawbacks can be prevented by not staining the gel until after electrophoresis.

2.1.7 Competent cells

To transform the plasmids into the non-commercial MG1655 and EK01 strains, I needed to make the cells competent, i.e., able to absorb foreign DNA. To do this, I first grew stationary phase cells in 50 mL LB at 37°C from OD_{600} of 0.04 to 0.5 and then incubated on ice for 20 minutes. Next, I pelleted the cells in a centrifuge at 1,000 x g and 4°C for 10 minutes and gently resuspended the pellet in 10 mL ice cold 0.1 M $CaCl_2$. After another incubation on ice for 60 minutes, I repeated the previous step with a reduced volume of 1 mL 0.1 M $CaCl_2$. After a final incubation on ice overnight, the cells were competent and ready for transformation using the same transformation protocol as the commercial NEB 5-alpha.

2.2 Microbial rhodopsin expression

2.2.1 Pigment test

The simplest way to test if a microbial rhodopsin is expressed and properly folded is by observing the colour resulting from the absorption of light by the rhodopsins. At high cell concentrations, some pigmentation may already be visible, but to increase the visibility of the pigmentation, I centrifuged cells in a liquid culture at 11,000 x g for 5 minutes to form a bacterial pellet that displays stronger pigmentation. For even better visibility, I exchanged the growth medium for the colourless BMB and repeat the centrifugation step.

2.2.2 Absorption spectra

For a more sensitive test of microbial rhodopsin expression, I measured the absorption of light through the sample. First, to negate the scattering of light through the sample, I had to lyse the cells. For this, I added one cOmplete Protease Inhibitor Cocktail tablet (Roche, Switzerland) to 50 mL HEPES buffer and resuspended bacteria in at least 1 mL buffer per 10^{11} cells with a minimum volume of 5 mL in 15 mL centrifuge tubes. I then incubated the cells with 0.1 mg/mL lysozyme in room temperature for 30 minutes, followed by 8 pulses of sonication for 20 seconds at full power using Soniprep 150 (MSE, UK) at 20 second intervals. I kept the sample in ice water and ensured no foam was produced during sonication. I centrifuged the cell lysate at 12,000 x g for 13 minutes to isolate the broken cells from the pelleted unbroken cells and then measured the absorbance of the supernatant from 400 nm

to 660 nm at 5 nm intervals using Infinite 200 PRO plate reader (Tecan, Switzerland).

To attribute the differences in the absorption spectra to the absorption of light by rhodopsins, I wrote a Python script (Table B.1) to produce differential normalised absorption spectra. First, I subtracted the mean absorption spectrum of the buffer without cell lysate from the spectra of the samples. Then, to eliminate spectral differences due to small differences in lysate concentration, I normalised each sample by fitting a line through the first and last three wavelengths and subtracting it from the absorption spectrum. Finally, I use the replicates of the lysate with no rhodopsins to get an average absorption spectrum that I subtract from all samples to get the differential normalised absorption spectra (Figure 2.4).

Despite normalisation, the differential spectra displayed apparent patterns in negative controls and within replicates, where differential signals were not expected (Figure 2.5, left), so I tried more ways to normalise the spectra. One, to simply divide each spectrum by its absorbance value at a single wavelength outside the range where rhodopsins can absorb light. Another, more elaborate, method was to measure the control lysate spectrum at various concentrations and interpolate the relationship between the absorption at a single wavelength to its full absorption spectrum, which can then be subtracted from each sample based on their absorbance at said wavelength. But due to the inconsistent shape of replicate spectra, all normalisation strategies resulted in different noise signals (Figure 2.5, middle & right), so I used the initial normalisation strategy that produced the smallest noise.

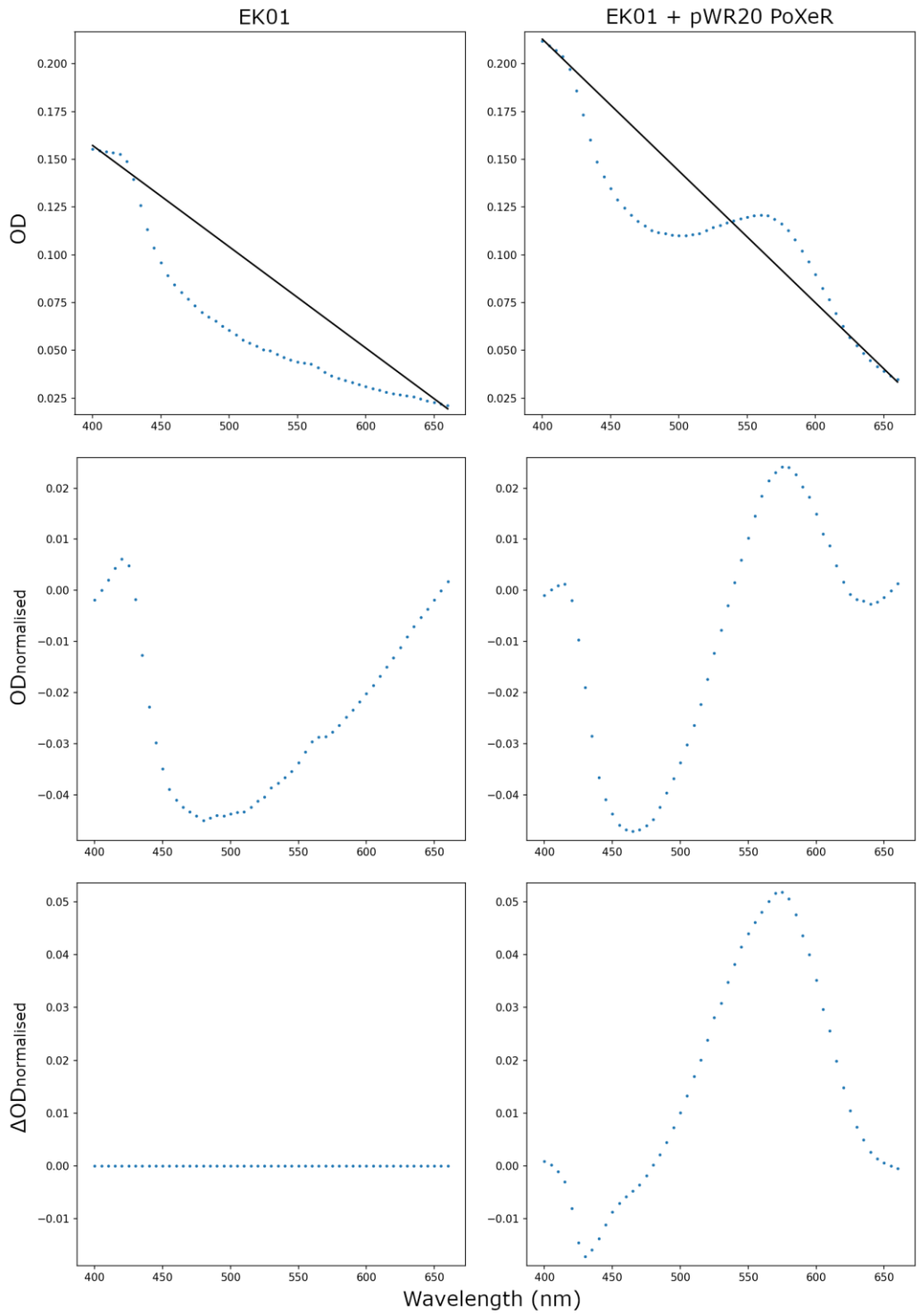

Figure 2.4: An overview of processing absorption spectra using line fitting. A line is fit through the ends of each spectrum (black line) and subtracted from the absorption spectra of the lysates (top) to produce spectra that are normalised for sample concentration (middle). The normalised control (middle left) is then subtracted from each spectrum to see the absorption due to rhodopsins (bottom).

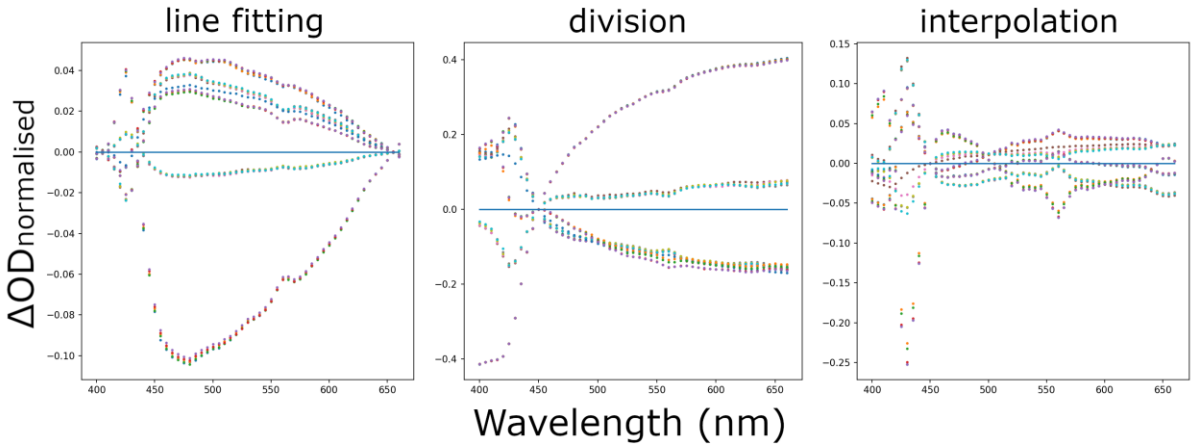

Figure 2.5: Differential absorption spectra have OD-dependent signals despite attempts to normalise the spectra. The absorption spectra of various rhodopsin-less cell lysates were normalised using the three different methods described above. Ideally, the differential spectra for rhodopsin-less cell lysates (coloured dots) should be zero throughout (blue line).

2.2.3 SDS-PAGE

To see if a rhodopsin was expressed but not properly folded, I tried to visualise the protein using SDS-PAGE. In the first protocol I followed, I pelleted 10^9 cells by centrifuging at 17,000 x g for 15 minutes, removed the supernatant and centrifuged for a further 2 minutes before resuspending the pellet in 100 µL RIPA buffer. I broke the cells by incubating them in 70°C for 5 minutes and separated the membrane from the cytoplasm by centrifuging the sample at 17,000 x g for 15 minutes and separating the pellet from the supernatant. I resuspended the membrane fraction in 50 µL RIPA buffer to solubilise the membrane proteins and digested the DNA in the cytoplasmic fraction by adding 250 units of Benzonase nuclease (Merck, Germany), and incubated both in 37°C for 30 minutes. I then mix the samples with NuPAGE LDS Sample Buffer (Invitrogen, USA), load them in a NuPAGE Bis-Tris precast gel and run the electrophoresis at 200V in NuPAGE MES SDS buffer for 40 minutes.

Finally, I stained the gel in 40 mL QC Colloidal Coomassie Stain (Bio-Rad, USA) overnight with gentle shaking and destained the gel in water for 1 hour.

This protocol did not work very well. The presumed membrane fraction that I separated from the supernatant formed an insoluble clump that I was not able to resuspend. Further, the soluble part of the membrane fraction gave essentially the same protein bands as the cytoplasmic fraction, but fainter. Since NuPAGE LDS Sample Buffer also contains a detergent, I tried to use it to replace RIPA buffer. This time, when I centrifuged the sample to separate the membrane from the cytoplasmic fraction, no pellet was formed. This meant that, firstly, the cells did not break properly in RIPA buffer, and secondly, this centrifugation speed was not sufficient to separate the membrane from the cytoplasm. Further, the new cell lysate was still highly viscous after incubation with Benzonase nuclease, meaning the DNA was not digested properly.

I noticed that Benzonase requires 1–2 mM Mg^{2+} for optimal activity, so I decided to use the same lysis protocol as for absorption spectra, since my HEPES buffer contains Mg^{2+} and this protocol had been working well. Now, to properly separate the membrane from the cytoplasm, I centrifuged the cell lysate at 130,000 x g for 90 minutes at 4°C and resuspended the pellet in NuPAGE LDS Sample Buffer. This time I had the membrane fraction, but I could still not see a band of the correct molecular weight that was different between the negative (no plasmid) and positive (PoXeR, which I knew is expressed) control, so I concluded that the signal of even strongly expressing rhodopsins is too weak using SDS-PAGE. Although this was not an important test, in hindsight, I probably still had too much carryover from the cytoplasmic fraction, which could hide the potentially weaker signal from the membrane fraction.

2.2.4 Growth analysis

To verify the growth defects that some colonies transformed with rhodopsins seemed to have, I first grew the cells to OD_{600} of 0.1 and grew 10,000X dilutions of these in a SPECTROstar Omega plate reader (BMG, Germany) in RDM at 37°C for 24 h while measuring OD_{600} at 5-minute intervals to get their growth curves and thus growth rates. Simultaneously, I used the same culture to inoculate LB agar plates with 100 and 1000 cells per plate. I grew the plates at 37°C overnight to assess the growth of individual colonies based on colony size.

To calculate the growth rate at a given time period on a growth curve (Table B.1), I used a rolling window of 9 data points to fit a straight line through $\ln(OD_{600})$ after subtracting the lowest OD_{600} of each sample from each point as the blank. To eliminate noisy data from beyond the detection threshold, I set a threshold value that all data points within a rolling window need to reach for growth rate calculation. Through trial and error, the erroneous values disappeared at a threshold of $OD_{600} \geq 0.02$. To calculate the growth rate at exponential phase, I took the average growth rate between the earliest and latest time point where growth rate is among the top 20 growth rates, as visualised in Figure 2.6. Due to the long rolling window, the growth rate 20 minutes before and later affect the growth rate calculation at a given point, limiting the optical density range for accurate growth rate measurement particularly for fast-growing cells. However, a shorter rolling window becomes more sensitive to device noise, which was a larger issue, and this was the best compromise.

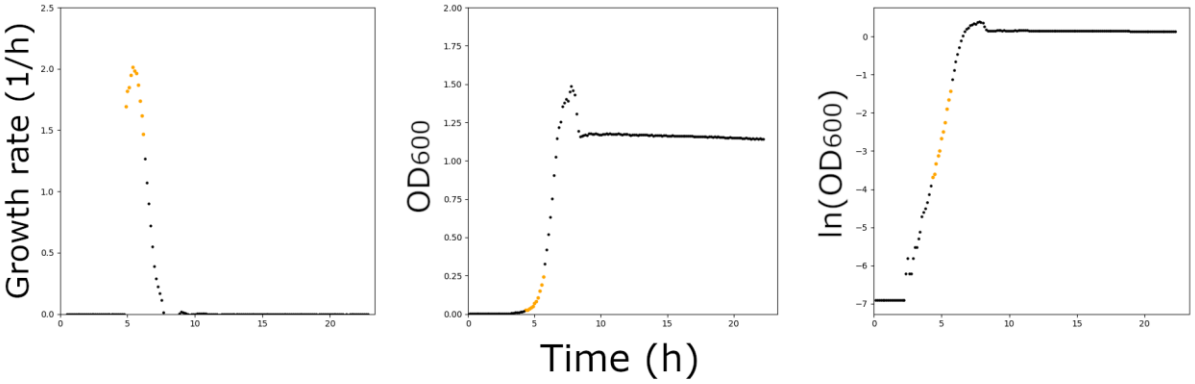

Figure 2.6: Exponential phase growth rate determination. The time points used to calculate exponential phase growth rate are plotted in orange for growth rate (left), optical density (middle) and the natural logarithm of optical density (right) over time.

2.3 Tethered cell assay

To study how the microbial rhodopsins affect cellular energetics, I used the rotation of the bacterial flagellar motor as a proxy for proton motive force (PMF), as the two have been shown to have a proportional relationship (Fung & Berg, 1995). My first method to measure the rotation was to record and analyse the rotation of single EK01 cells tethered to a glass coverslip from their flagella affected by the fliC^{sticky} mutation of the flagellar filament.

2.3.1 Cell culture

To measure flagellar rotation, I need the cells to have good gene expression related to motility. The motility of *E. coli* depends on its growth state and environment (Cremer et al, 2019), so I started with three growth conditions that have previously yielded motile cells in the lab. Starting from a frozen stock of stationary phase EK01 cells, I grew a 1) 10^5 dilution in RDM, as described in Section 2.1.2, at 37°C until OD_{600} = 0.2, 2) 10^3 dilution in LB at 37°C until OD_{600} = 2.0 or 3) 10^2 dilution in TB at

30°C until OD_{600} = 0.8. LB and TB are fast and convenient media, ideal for experiment optimisation, but their contents are undefined, and cells growing in them sequentially deplete different nutrients, undergoing many physiological changes (Sezonov et al, 2007). Hence, for data collection, RDM is preferable for reproducibility. I wrapped the flasks in aluminium foil to shield the rhodopsins from light before the experiment and used a shaker to improve the oxygenation of the culture.

2.3.2 Sample preparation

To reduce the radius of rotation of the motile cells, I sheared the flagellar filaments by using syringes to pass the sample through a pair of 26-gauge needles connected with 0.58 mm inner diameter polyethylene tubing between 0 and 80 times (Chen & Berg, 2000). I then loaded the sheared or unsheared cells into a self-assembled tunnel slide (Figure 2.7), incubated the cells in a humidity chamber for 10 minutes to allow the cells to attach to the slide while minimising evaporation, flushed the slide with a buffer or medium of choice to remove unattached cells and determine the extracellular conditions, and sealed the ends of the slide to stop evaporation and oxygen replenishment using CoverGrip Coverslip Sealant (Biotium, USA).

2.3.3 Data collection

To record the spinning of cells in response to illumination, I used a Nikon Eclipse E-200 microscope with a 40X objective (Nikon, Japan) to perform phase contrast microscopy, recording 100 frames per second. I illuminated the sample with the built-in 6V 20W halogen lamp with a longpass filter between the light source and the

sample. To induce light-powered ion pumping, I used the lamp at full power with FGL515, a 515 nm longpass filter (Thorlabs, USA), resulting in 2.88 mW/cm^2 light intensity at sample plane. This filter blocks the more damaging light of shorter wavelengths. To record the cells without inducing light-powered ion pumping, I used FGL645, a 645 nm longpass filter (Thorlabs, USA), blocking the light corresponding to the rhodopsin action spectra. Between recordings, if I did not need to induce light-powered ion pumping, I turned the lamp off. I maintained a single field of view throughout each individual experiment to allow the tracking of individual cells.

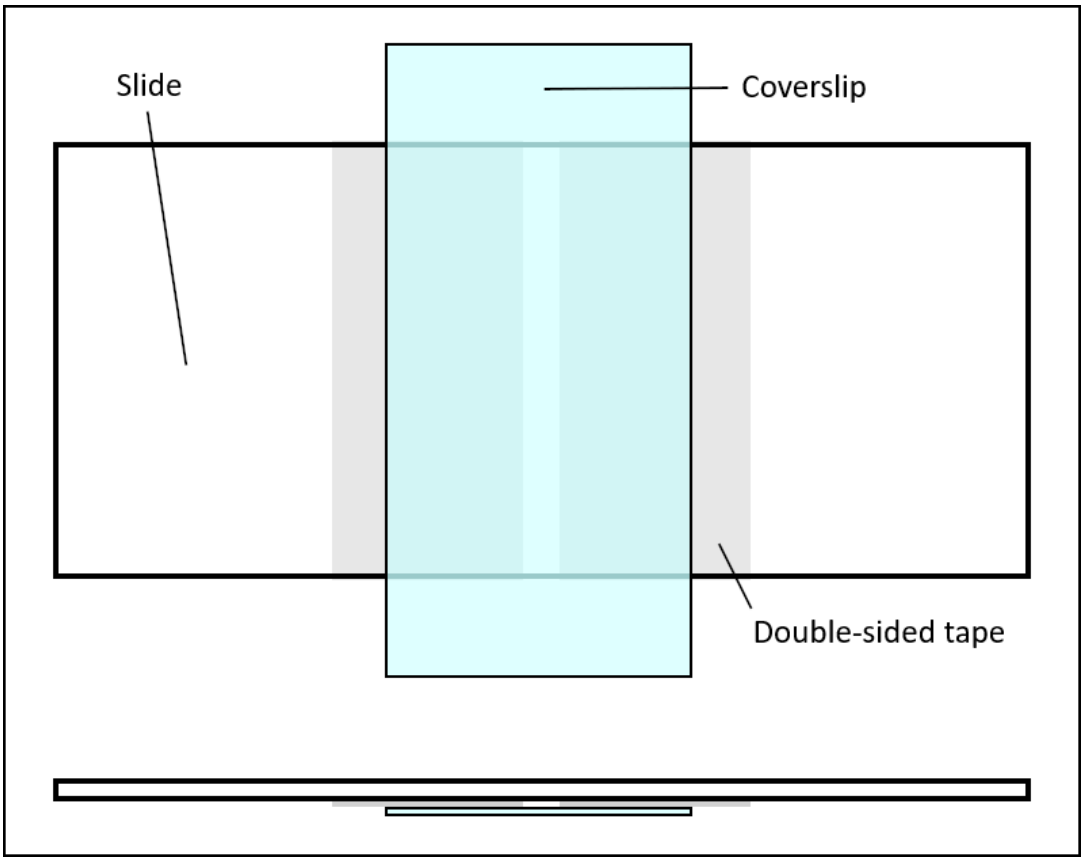

Figure 2.7: Tunnel slide schematics from the top and the side. A glass slide and a glass coverslip, attached with two pieces of double-sided tape approximately 4 mm apart, form a 100 µm high open-ended chamber between the tapes.

2.3.4 Data analysis

To analyse the rotation speed of individual cells, I made a cell tracker that consists of two separate parts. First, to convert the images into various measurements, I wrote an ImageJ script to process a large number of images as follows. To remove the granular noise from the image, I apply a 3x3 pixel median filter. Then, to separate cells from the background, I apply a manually selected threshold, generating a binary image. To add cells as regions of interest and further reduce noise, I run the Analyze particles plugin to select regions consisting of 50–200 black pixels whose circularity, defined as $4\pi(\text{area}/\text{perimeter}^2)$, is between 0 and 0.8, excluding cells at the edges. Finally, for each region from the original image, I use the roiManager to measure the minimum, maximum and mean pixel intensity, the area, the X and Y coordinates of the center of mass, the length and width, and the angle of the line that determines the length. This results in a csv file containing these measurements for each cell in each frame of a recording.

The second part of the tracker is a Python script (Table B.1). First, as the recording speed was not always stable, I used the image metadata to attach a time to each measurement. The image timestamp accuracy was limited to seconds, so I counted the number of images with the same timestamp to determine the time difference between images on the corresponding second. The first and last second were not full, so I assigned them the frame rate of the nearest full second.

Next, to track individual cells over time, I sorted the cell data by iterative grouping. I start the sorting process by calculating the distance of each cell to the first cell on the list based on the X and Y coordinates from the first script. I choose the nearest cell from each image, calculate new mean coordinates of this group of

cells and repeat the distance selection based on the new predicted center of rotation. At both selection steps, I unselect cells that are further away than the 90th percentile of cell lengths and more than 30% longer than the median cell length of the group. This is repeated until each cell has been assigned a group containing 1 or more cells. I assigned groups where the presumed cell appears in less than a selected threshold, for example 25%, of the images as noise. I then refine this rough grouping by training a random forest regressor model using the coordinates, length, width and angle as features to predict which group the cell belongs to, and apply the model back on the same data. If the prediction score was below 80%, the cell was assigned into the group with the second-best score, such that well grouped cells stay in the same group and loosely grouped cells switch groups until the best grouping is achieved. After each round of machine learning, I assign distant cells and lower-scoring duplicates as noise and calculate the root mean square prediction score to determine the best grouping arrangement. After 5 rounds, most cells are properly grouped as a single cell at different time points (Figure 2.9 B).

Now that the data from the first script was sorted by cell identity, I could extract cell rotation from the angle difference between consecutive images and calculate spinning frequency based on the calculated time stamps. However, the rotation data was sometimes noisy, so I wanted to smoothen the cumulative rotation curve with a mean or median filter. As the cells frequently change their spinning direction, such filter would flatten the peaks caused by switching. To solve this, I identified all positive and negative peaks and mirrored the values relative to each peak at a time, producing a curve with no peaks. A mean filter with a window size of 5 would now not dampen the peaks, after which I reversed the mirroring to return a smoothened cumulative rotation curve with unaltered peaks.

To get the mean rotation frequency of single cells and the population of cells over time, I have to exclude non-motile cells and times when motile cells do not spin, e.g., due to being stuck. To do this, I have to differentiate between motor-driven spinning and rotational Brownian diffusion. Jain & Sebastian (2017) have derived an equation for the probability density function of rotational Brownian diffusion for a small time step

$$PDF = \frac{1}{\sqrt{4\pi Dt}} e^{-\frac{\theta^2}{4Dt}}$$

where t is time, θ is rotation angle and D is the rotational diffusion coefficient of colloidal rods defined as

$$D = \frac{3k_B\ T\ ln\left(\frac{L}{W}\right)}{\pi\eta L^3}$$

where k_B is the Boltzmann constant, T is temperature, L and W are cell length and width, and η is viscosity (Heyes, 2019). To define non-Brownian rotation, I created a simulation of rotational Brownian diffusion by sampling this probability density function over many small time steps. From each diffusion simulation, I took the difference between the highest and the lowest cumulative rotational distance, i.e., the maximum rotational displacement (see red arrow in Figure 2.8 A), and defined rotation as non-Brownian motion for values with <1% chance to achieve in my simulation, i.e., above the 99th percentile. To determine the 99th percentile for each condition, I could run the simulation a thousand times and take the 99th percentile, i.e., the 10th highest value. However, sampling error near the ends of a distribution gets significantly higher (Roy et al, 2016). Sampling error generally decreases with the square root of sample size, so the accuracy could be improved, but is limited by computational power. Instead, I noticed that the probability distribution of the

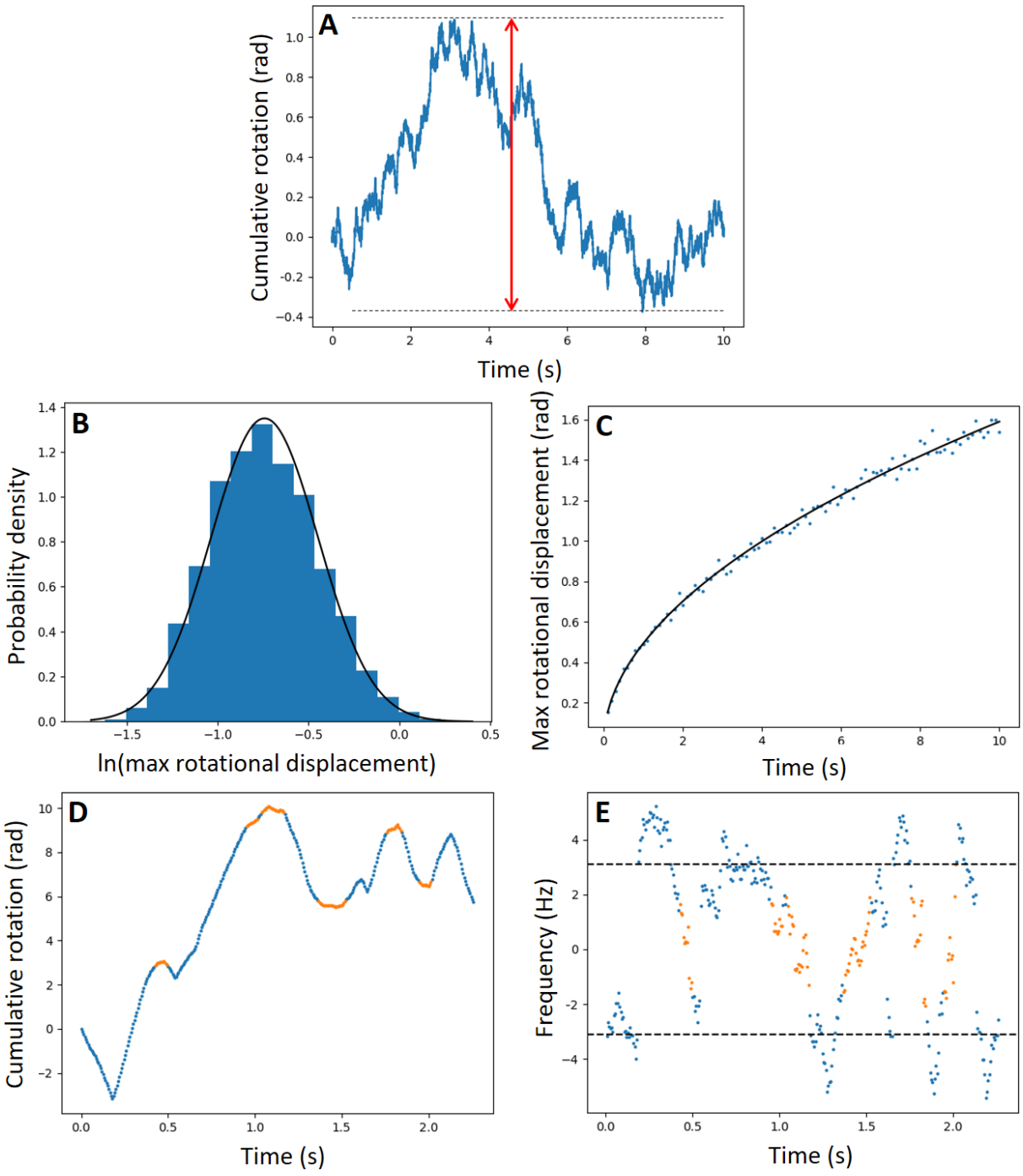

Figure 2.8: Motility filter for cell tracker analysis. (**A**) Cumulative rotation (blue line) by Brownian diffusion was simulated for various durations at 1 ms time steps, and maximum rotational displacement determined as the motion range (red line). (**B**) The density histogram of ln(maximum rotational displacement) (blue, n = 10,000) can be approximated by a normal distribution (black line). (**C**) The 99th percentile of maximum rotational displacement over diffusion duration (blue dots) follows $constant * \sqrt{time}$ (black line). (**D**) An example rotation trace, where motility (blue) is distinguished from non-motility (orange). (**E**) Same as (D), but the plotted value is rotation frequency, and the average frequency has been plotted on positive and negative axes (dotted line).

rotational displacement is approximately lognormal (Figure 2.8 B), meaning I can calculate the 99th percentile faster and more accurately using the mean and standard deviation of a smaller sample of simulations. Simulating and calculating the 99th percentile for various diffusion durations revealed that the value is proportional to $\sqrt{time}$ (Figure 2.8 C), meaning one simulation duration can be applied to rotation at all timescales. This proportionality held true regardless of cell size. Now, I defined the cell as fully non-motile if its maximum rotational displacement did not exceed the 99th percentile for the duration of the recording, and temporarily non-motile for all time periods where the simulated value was not reached for at least 9 images. As cell size data was extracted from the first script, the simulation can be run for each cell individually.

Filtering fully non-motile cells is easy, but separating temporary non-motile moments from slow rotation and direction switching is more challenging. However, my motility filter was able to do exactly this, as seen from an example trace where the cell sometimes switched directions with and sometimes without stopping in between (Figure 2.8 D & E). Testing my cell tracker on fabricated data with defined cell motility concludes that it works as intended, capturing the magnitude, direction and duration of rotation, as well as filtering Brownian motion (Figure 2.9).

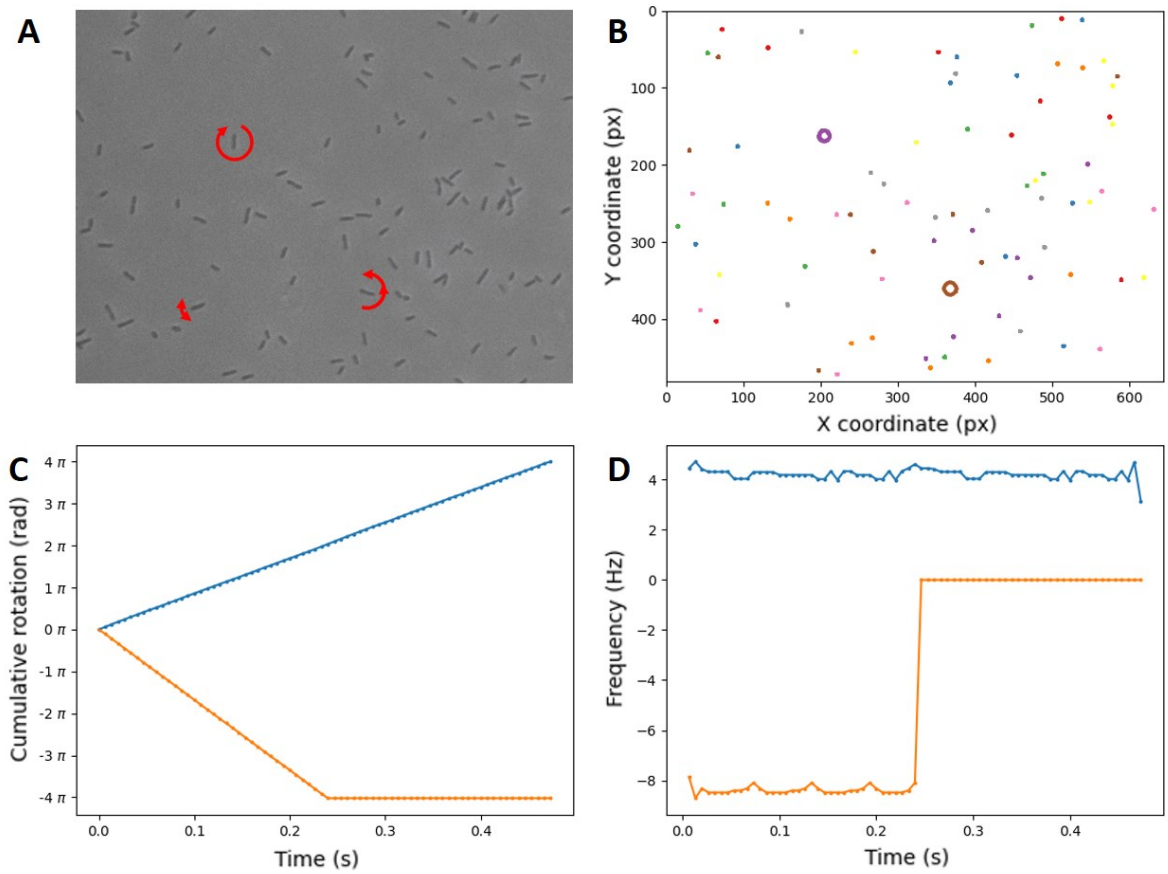

Figure 2.9: Cell tracker verification. (**A**) I created test data from a single image, where I rotated one cell 10° clockwise and one 20° counter clockwise per image, for a total of two rotations each (as indicated by arrows), and I rotated one cell randomly back and forth to simulate Brownian motion. The data consists of 72 images whose frame rate I defined as 150 per second. (**B**) A visualisation of cell grouping, where members of each group are plotted with the same colour from a repeating set of colours. All cells are correctly grouped together, although real data has more noise, which would be plotted in red. (**C**) The cell tracker analyses the cumulative rotation of each spinning cell while ignoring non-motile cells. The plotted cumulative rotation matches the data I created. (**D**) The cell tracker analyses the rotation frequency of each spinning cell, which, again, gives the same results as described in (A).

2.4 Differential dynamic microscopy

My next method to measure flagellar rotation relies on the roughly linear relationship between flagellar rotation and bacterial swimming speed (Magariyama et al, 1995). Differential dynamic microscopy (DDM) extracts the average swimming speed of a population of cells by analysing a series of low-magnification images as described later in this section.

2.4.1 Cell culture

To obtain highly motile cells, I grew 10^5 dilutions of frozen stock of MG1655 in supplemented MOPS minimal medium, as described in Section 2.1.2, at 37°C to OD_{600} of 0.3. Like for tethered cell assay, I shielded the samples from light. To maintain a source of OD_{600} = 0.3 exponential phase cells throughout the day, I used the turbidostat mode of the OGI microbioreactor Liquid Control Module (OGI Bio, UK). Later, to avoid bioreactor-related motility issues, I switched to a manual turbidostat, i.e., manually diluting the sample based on growth rate such that the sample reaches OD_{600} of 0.3 at 1–2-hour intervals.

2.4.2 Sample preparation

To ensure a constant initial supply of nutrients in my experiments, I introduced the cells to the experiment buffer as late as possible before data collection. To keep the majority of the nutrients untouched until then, I concentrated the sample to such high concentration that its contribution to the final volume was at most 10%, usually only 1–5%, meaning the sample usually starts with 95–99% of the nutrients of the

experiment buffer. To minimise the physiological changes occurring after removing the sample from exponential growth and caused by handling-induced stress, I stripped the concentration protocol to be as quick and gentle as possible. When using BMB + 1 mM glucose as the experiment buffer, I centrifuge 1.5 mL of sample at 2,000 x g for 5 min, remove most of supernatant and resuspend the pellet in a final volume of 15–30 µL by gently flicking the tube. In this condition, glucose is in excess and the small volume of depleting growth medium has little effect on the parameters of the experiment. When using BMB without added glucose, I dilute the 15–30 µL concentrated sample in 1.5 mL BMB and repeat the centrifugation to ensure the trace amounts of glucose are depleted before adding the cells to the experiment buffer.

I then dilute 1 µL of the concentrated sample in 1 mL PBS to measure the optical density of the sample, which typically reaches OD_{600} of 15–30, to calculate the appropriate amount of sample to add to the experiment buffer for the desired final concentration. I verified the accuracy of optical density measurement with such high dilution by comparing the measurements of 1000X and 100X dilutions of a sample. Once diluted in the experiment buffer to OD_{600} of 0.1–2, I load 3 µL into a 20 µm microchamber counting slide (Leja, Netherlands) and seal the chamber with petroleum jelly.

2.4.3 Data collection

I recorded 40 second phase contrast image series of swimming bacteria at 100 fps using a 10X objective and 2x2 binning to reduce the image size to 512x512 px to manage file size. For long experiments, I recorded at 3-minute intervals, and for

short time-scales, I recorded continuously. For experiments with a narrow, concentrated light beam, I used a Nikon Eclipse Ti inverted microscope with a SOLA SE II LED Light Engine (Lumencore, USA). The light partly shares the optical path of the microscope and passes through the FF01-554/23 filter (Semrock, USA) before reaching the sample plane at 260 mW/cm^2 at full power. For experiments with full sample illumination, I fixed a 1104 lm SP-03-L1 LED module (Quadica, Canada) with a SATU-S 18° circular beam integrated lens (LEDiL, Finland) and an HQ540/80m filter (Chroma, USA) at a 45° angle, 5 cm away from the sample on a Nikon Eclipse TE2000-U inverted microscope, achieving 208 mW/cm^2 illumination at full power.

2.4.4 Data analysis

Two images of moving bacteria separated by time become progressively less correlated as the time difference τ increases. This is because of the movement of bacteria over time, and this connection is exploited by DDM to extract information such as the swimming speed from a series of images. To do this, the intensity of each pixel of image n is subtracted from each pixel of image n+ τ. The same is done for each combination of images with a given τ. With 4000 frames, this produces 3999 difference images with τ = 1 frame (10 ms at 100 fps), 3998 difference images with $\tau = 2$ frames and so on. For each 512x512 px difference image, a 2D Fourier transform is performed, resulting in another 512x512 grid where the value of each pixel is a complex number, and the squared modulus of each complex number is taken.

The squared moduli for each pixel in Fourier space are then averaged among each group of difference images with the same τ, as swimming speed is assumed to

be constant throughout the image series. Further, since swimming speed is isotropic, i.e., not affected by direction, these values are further averaged among the values of the 512x512 grid that have the same distance in reciprocal space, q, from the center of the grid. Now, we have a differential image correlation function $g(q,\tau)$ (Martinez et al, 2012) which relates to a model of the intermediate scattering function of a population of swimming and diffusing cells (Stock, 1978) that the data can be fitted to, thus giving the parameters of diffusion, swimming speed, speed distribution and the fraction of motile and non-motile cells that best fit the data. The model is fitted for each value of q, and finally the average values for an appropriate q range are used.

To perform the DDM analysis, I used a DDM analysis program, written by Jochen Arlt (University of Edinburgh), that performs the above analysis and returns the model parameters separately for each value of q. For typical use, a single 40 s image series yields data for one time point, but for short time-scales, 10 s was enough to still get reliable data with better time resolution. To analyse the output of the DDM program, I wrote my own Python script (Table B.1) that, among trivial functions, filters model fits with impossible parameters, unsuitable q-values and whole time points with too large discrepancies along the q-axis, which typically happens when the cells swim too slowly and cannot reliably be distinguished from diffusing cells. The established default q-range for measuring the swimming speed of bacteria was 0.5–2.0 μm^{-1}, but for slowly swimming samples, I had to manually adjust this. To identify the reliable q-range, I compared the consistency of fit parameters between adjacent time points and between adjacent q-values. If the parameters fluctuate along both while they follow a sensible trend at a different area of the time-q axes, it is a sign of poor distinction of swimming from diffusion. For oxygen depletion measurements, I defined the depletion time as the time between

the two adjacent time points with the largest speed difference +/- half of the unrecorded time in between.

Chapter 3

Expressing microbial rhodopsins in *E. coli*

3.1 Introduction

The number of known microbial rhodopsins is large and ever-increasing. New variants emerge both through discovery in genomic sequencing studies (Rusch et al, 2007) and engineering of custom properties like altered action spectra or functions (Inoue et al, 2019; Vogt et al, 2019). However, microbial rhodopsins are mostly characterised in – and optimised for – mammalian systems for electrophysiological studies (Muir & Bagot, 2019). When they are expressed in *E. coli*, they are usually expressed in mutant strains, lacking proteases or components from metabolic pathways, in abnormal levels using phage T7 polymerase. To investigate the optogenetic manipulation of bacterial electrophysiology, I need to express microbial rhodopsins in a physiologically wild-type strain, such as MG1655, in quantities that do not alter cell physiology.

In this chapter, I will cover the cloning and expression of the rhodopsins PR, PoXeR, ArchT, NpHR, ChEF, ChIEF and Chrimson. Some of the rhodopsins expressed well, while others had varying degrees of problems. I will discuss the potential mechanisms behind the problems I encountered in the heterologous expression of microbial rhodopsins.

3.2 Cloning

While my cloning method would normally not be complicated, I encountered some curiosities of biological significance. To assemble my genetic construct, I needed to create complementary single-strand overhangs to promote ligation. To do this, I used restriction enzymes to trim the ends of PCR fragments, but cutting this close to the end of the DNA fragment can be problematic. Later, when introducing my genetic constructs to bacteria, I experienced how phenotypic changes caused by the construct can make it harder to find the bacteria harbouring them because of unconscious bias. In this section, I will briefly discuss these encounters.

3.2.1 Cleavage near the end of a DNA fragment

The short DNA sequence that constitutes a restriction site, the recognition sequence of a restriction enzyme, is not the only part of DNA involved in restriction digestion. Depending on the restriction enzyme, the recognition sequence needs to be flanked by a certain number of bases for efficient or any cleavage of DNA (NEB, n.d.). Because of this, I added 3 extra bases to the PCR fragments that I wanted to add into the pWR20 expression plasmid, as that was reported to be sufficient for efficient

cleavage using NdeI and BamHI-HF (NEB, USA). However, when I verified the success of the ligation and transformation of these digested fragments using colony PCR, only one of the rhodopsins was successful, while the other genes were not found in any of 36 transformants tested (Figure 3.1).

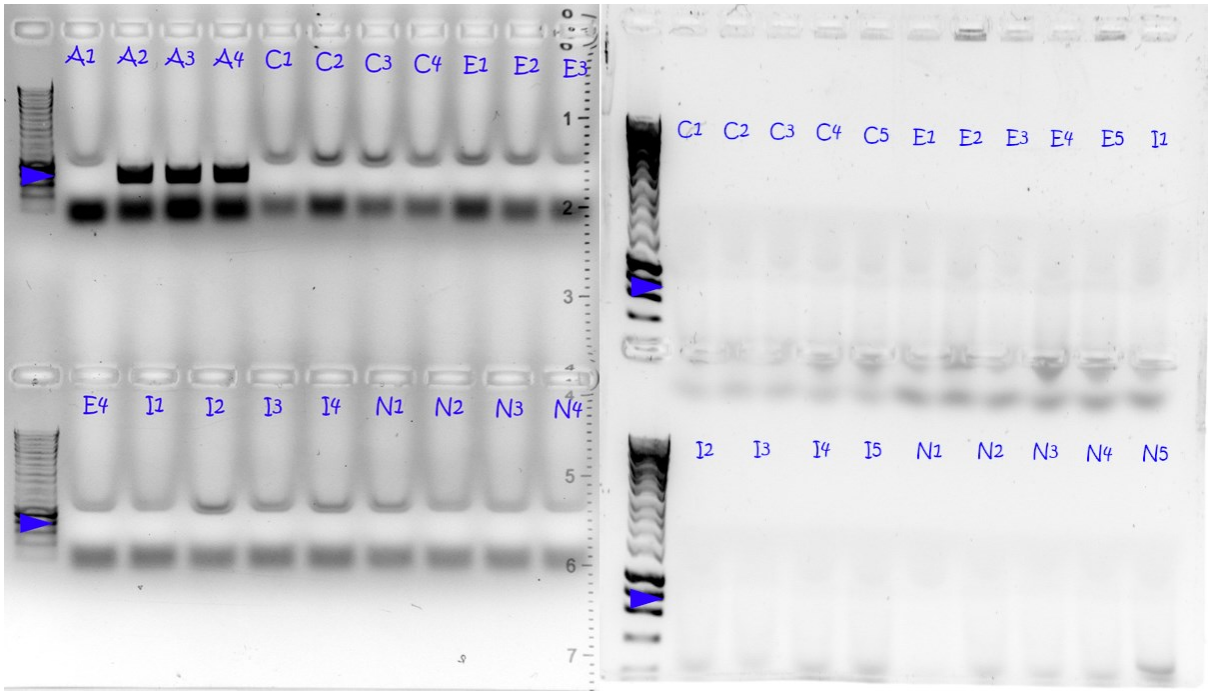

Figure 3.1: Results of two colony PCR experiments testing for the presence of rhodopsin genes. Blue arrows mark the location of the bands that indicate the presence of the gene. The letters indicate colonies that, if successful, express ArchT (A), Chrimson (C), ChEF (E), ChIEF (I), NpHR (N). The numbers distinguish individual colonies from the transformations.

Despite having purified the pWR20 backbone after cutting the GFP gene from it, a surprising amount of transformants contained the full pWR20 plasmid, evident from their green colour. To avoid these transformants, I repeated the ligation with a pWR20 fragment that I cut from a PCR product lacking the GFP gene rather than the full plasmid. This time, the transformation yielded a lot fewer colonies, all of which were white, that all were still missing the rhodopsin genes. To investigate the molecular mechanism behind the unsuccessful attempts, I sequenced one of the transformed plasmids and found that NdeI was not cleaving at the end of the plasmid

backbone (Figure 3.2). How it managed to cleave the end of the ArchT fragment whose last 9 base pairs were identical to the other rhodopsins, is still a mystery to me. However, adding another 3 bases, to a total of 6 bases after the recognition sequence, enabled successful cleavage for the rest of the genes.

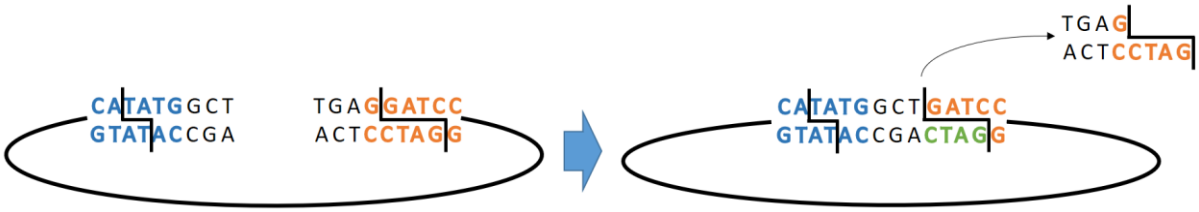

Figure 3.2: Sequencing result reveals unsuccessful NdeI cleavage at the end of a DNA fragment. The letters represent the DNA sequence at the ends of a linear plasmid backbone that was obtained through PCR. Blue letters indicate the NdeI and orange letters the BamHI recognition sequence. The line connecting the letters represents the rest of the linearised plasmid, and the lines going through the letters represent the cleavage site of the restriction enzymes. After restriction digestion and ligation (blue arrow), the DNA sequence in this region was as shown on the right, consistent with successful BamHI and unsuccessful NdeI cleavage. Green letters indicate bases that were likely inserted by DNA repair machinery.

3.2.2 Frameshift mutations provided a selective advantage

Though I had managed to fix NdeI cleavage and insert most of the rhodopsin genes into the pWR20 backbone, I encountered another problem: the ChEF and ChIEF genes had a deletion at the beginning of the gene causing a frameshift mutation. When I analysed the region with the deletion, I noticed a highly repetitive sequence that likely facilitated this deletion (Figure 3.3). To investigate the cause of this deletion, I first sequenced the original plasmids containing these genes and confirmed that the deletion was not already present. I then redesigned the PCR primers at the deletion site such that I moved their annealing site 9 bases upstream, to avoid the repetitive sequence. This meant I could not include the NdeI site as a primer overhang, as there was not enough complementary sequence between the

start of the gene and the repetitive sequence for sufficient primer annealing. Instead, I added the NdeI site as a mutation using PCR mutagenesis, meaning I added another complementary region to the primer after the 3 non-complementary bases required for the NdeI site.

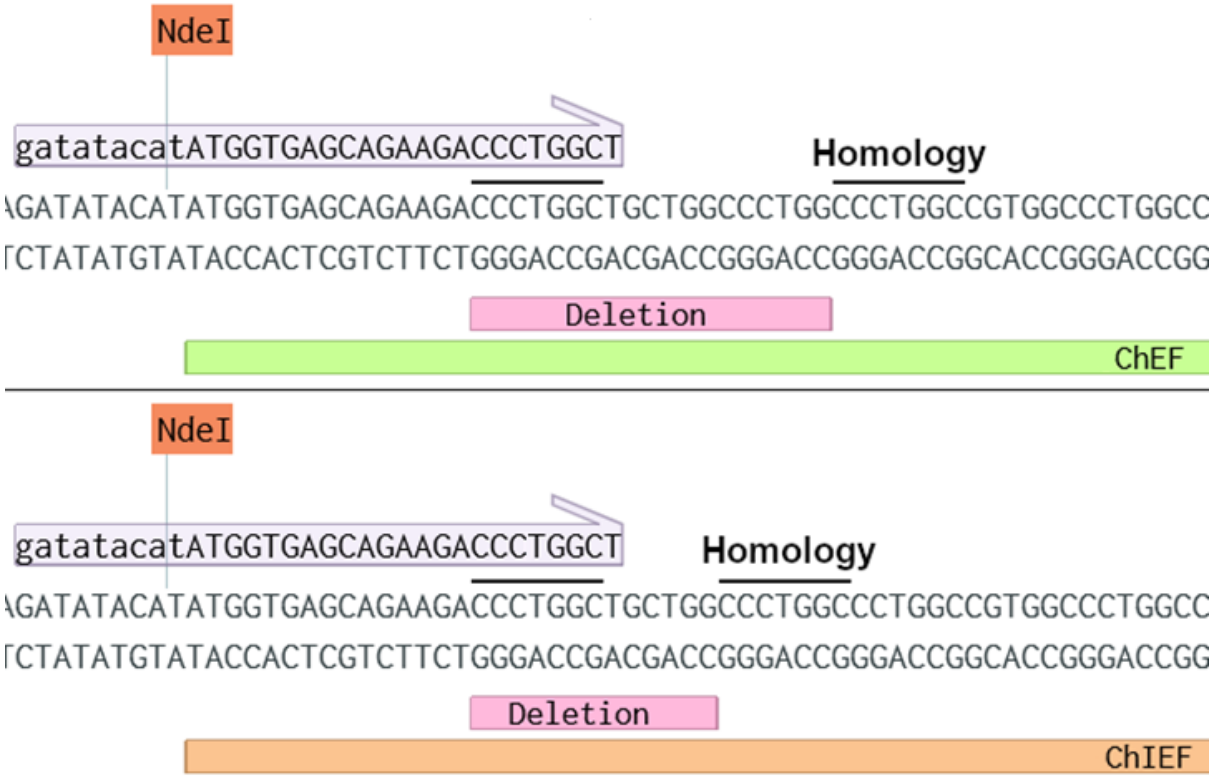

Figure 3.3: Deletion at a highly repetitive sequence. The sequencing result of the near identical ChEF (above) and ChIEF (below) genes revealed a deletion at the beginning of each gene, marked with the coloured boxes. The deletion is consistent with the newly synthesised strand annealing at the homologous sequence underlined above, causing the deleted region to form a loop that does not get replicated. This could happen either during PCR or natural DNA replication. The underlined sequence can be found several times in the sequence above, leading to varying deletion sizes. Though it seems more likely for the deletion to occur during PCR, the lack of the last thymine of the primer (grey box) in the DNA sequence suggests the deletion happened after PCR.

When I repeated the experiment with the new primers, I noticed that the ChEF transformant with the best PCR signal for the presence of the gene was slightly smaller than the others. This time I also tested the small colonies that I assumed

were satellite colonies, i.e., non-resistant bacteria that grow around resistant colonies after they degrade the surrounding antibiotics. The normal-sized ChIEF colony had yet again a deletion at the start of the gene, causing a frameshift. Surprisingly, the slightly smaller transformant only had a single base substitution, causing a valine-to-methionine substitution, while the small transformants had no mutations at all. So, the more mutated the ChEF and ChIEF gene was, the better the cells grew on the agar plate.

I concluded that the transformation yielded 3 different types of transformants: 1) colonies with an intact pWR20 plasmid with GFP, these grew normally and were green, 2) colonies with a pWR20 backbone containing disabled rhodopsin genes or no insert, these grew normally, were white and could only be distinguished through PCR or sequencing, 3) colonies with a pWR20 plasmid containing functional rhodopsin genes, these were white and their growth depended on the effect of the rhodopsin on the cell. When divided into these groups, all transformations with different rhodopsins seemed to yield the same amount of each type of transformant (Figure 3.4). I will discuss this phenomenon further in Sections 3.5 and 3.6, but for the topic of cloning, besides the literal selective advantage the mutations provided, they also provided an advantage to the chance of being selected by me for analysis. In other words, this phenomenon prevented me from finding the successfully cloned plasmids because of the unconscious bias for selecting healthy colonies.

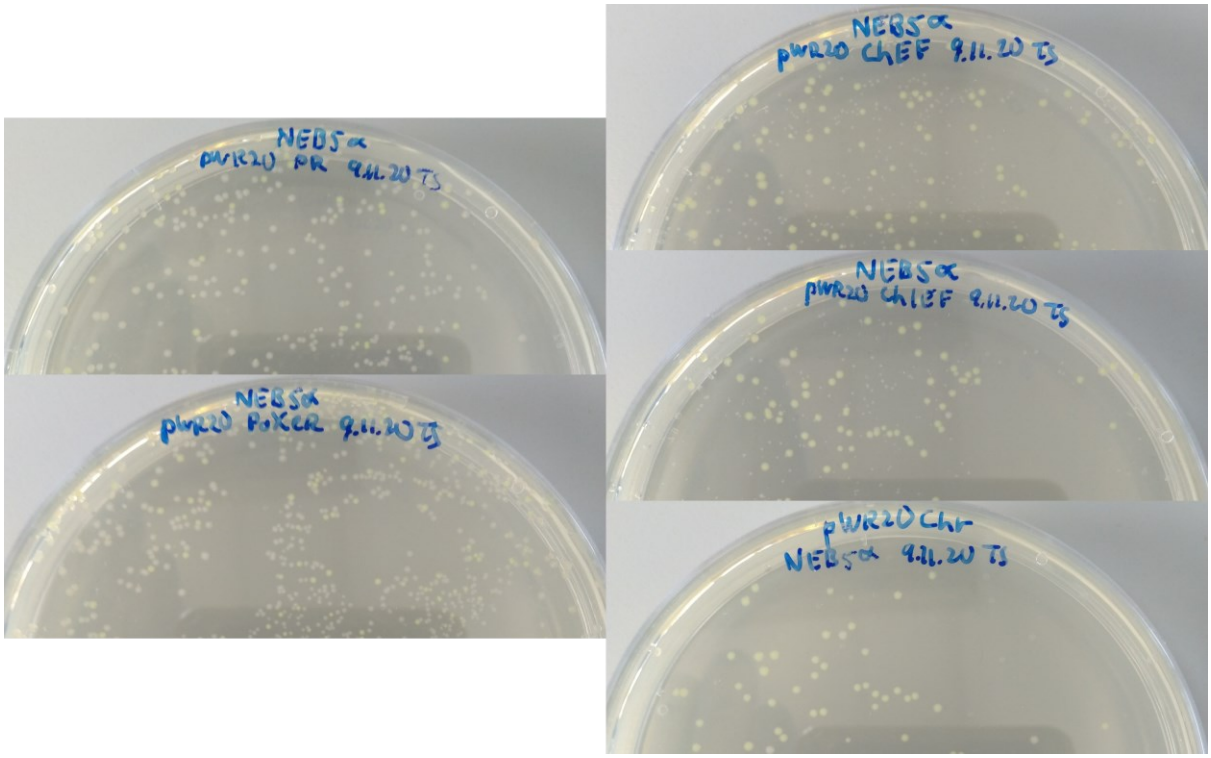

Figure 3.4: The fate of rhodopsin-expressing transformants depends on the rhodopsin species. NEB 5-alpha cells transformed with PR, PoXeR, ChEF, ChIEF and Chrimson ligated into pWR20 and plated on LB agar plates. The two halves of each plate contain different concentrations of bacteria, only top half is shown for clarity. The number of green and white transformants appears roughly equal in each plate, but the white (mutation-free) colonies grew either normally (PR, PoXeR), slower (ChEF, ChIEF) or not at all (Chrimson). The green transformants on the plates with ChEF, ChIEF and Chrimson are slightly larger due to reduced competition. This pattern suggests that the ligation and transformation efficiency of each rhodopsin was equal, and the observed differences are due to rhodopsin species-dependent growth difference.

3.3 PR expression in *E. coli*

PR was found in a genomic fragment of SAR86 γ-proteobacterium (Béjà et al, 2000) and has since been expressed in various *E. coli* strains including MG1655 (Schwarz-Linek et al, 2016). Unsurprisingly, I had no problems expressing PR myself. However, the expression level of PR in *E. coli* is highly variable based on multiple factors, the most obvious factor being the strain and expression system. The bright colours from highly overexpressed rhodopsins were not so bright in my strains, and

there are significant differences in hue between different strains and plasmids (Figure 3.5). Although it is possible that other studies have used different variants of PR, the gene in Figure 3.5 B and C is certainly the same, as I used the plasmid from the latter to make the plasmid for the former.

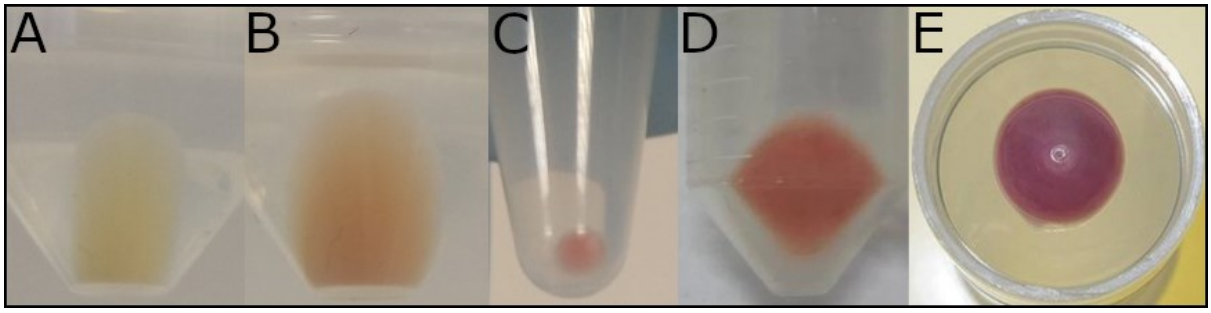

Figure 3.5: PR expression varies largely in different strains. Cell pellets of MG1655 expressing no PR (**A**), PR from pWR20 (**B**), PR from pBAD (**C**), BL21 expressing PR from pACYC-Duet1 (**D**; Kim et al, 2012) and from pBAD (**E**; Song et al, 2019).

PR expression within the same strain also varies (Figure 3.6). The expression in simultaneously grown cells is stronger when grown in a conical flask with better oxygenation than a centrifuge tube. The growth medium also had an effect, for example, the expression was stronger in LB than in RDM. This may be related to something in RDM causing stress to the cells, as seen later in Section 4.2.1. The most notable effect was the growth phase, where early stationary phase showed the best expression that then decreased in late stationary phase.

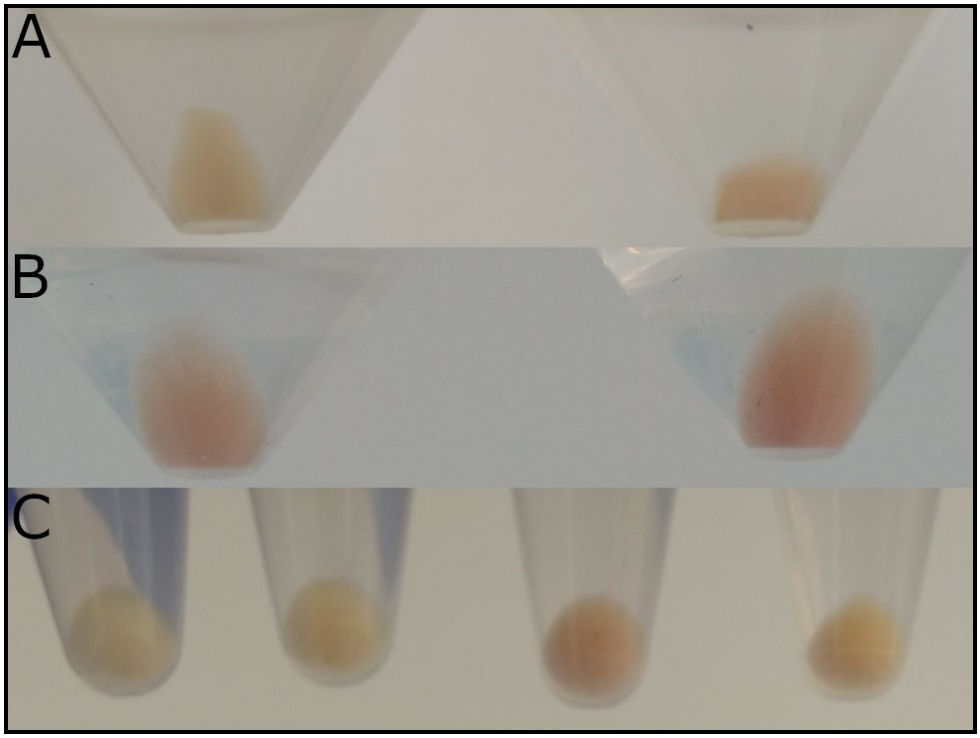

Figure 3.6: PR expression varies within the same strain. (**A**) Cells grown in a 125 mL conical flask (right) have a stronger PR pigment than cells grown in a 50 mL centrifuge tube (left). (**B**) Cells grown in LB (right) have a stronger PR pigment than cells grown in RDM (left). (**C**) Tubes from left to right contain a fixed number of cells grown to OD_{600} (1 cm path length) of 0.3, 0.9, 1.8 and 4.4.

Though early stationary phase gave the highest PR expression, I must also consider the motility of the expressing bacteria and the reproducibility of the cell physiology, which are better during exponential phase when PR expression is weaker. As seen in Figure 3.6 C, sometimes PR expression is barely noticeable, so I wanted a more sensitive way to detect expression. I did this by measuring the differential absorption spectrum of cells with and without rhodopsin expression. To measure the absorption accurately, I first lysed the cells to avoid the loss of light due to scattering from intact cells instead of absorption by cell components. In the end, I was able to detect PR expression even if I could not see the pigment visually (Figure 3.7), and these exponential phase cells also retained their PR activity in light, as seen in Chapter 4.

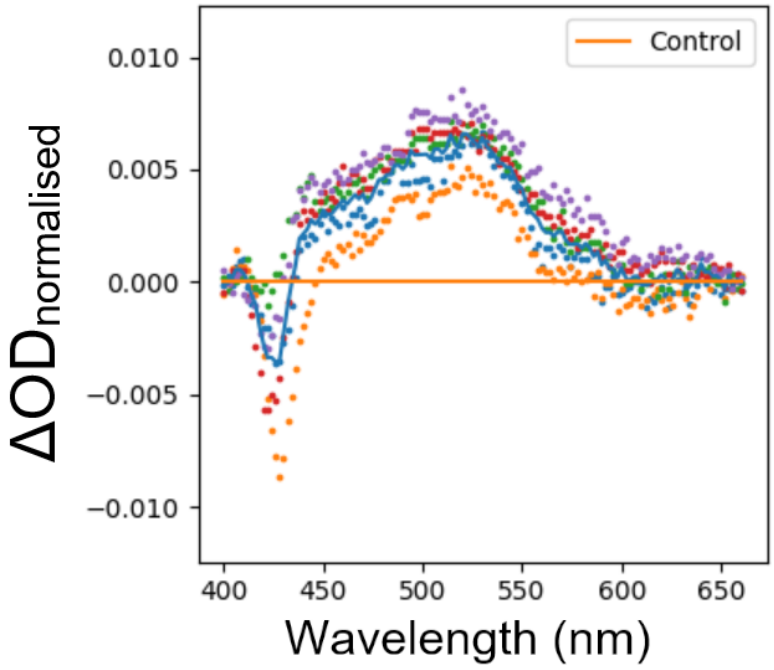

Figure 3.7: Absorption spectrum of PR-expressing cell lysate. The coloured dots are 5 replicates taken from the same lysate. The orange line is the average normalised OD of the cell lysate without PR, set as the frame of reference for all values. The blue line is the average of the 5 replicates.

PR also seems to be very stable once made. I left a liquid culture of PR-expressing cells in room temperature for several months out of curiosity, and the colour of the cells sedimented by gravity never faded at all. While the cells at the end of the experiment were likely no longer alive, PR was neither degraded by cell activity during starvation nor by environmental effects after cell death. This suggests that the decreased expression in late stationary phase is not due to the balance between degradation and decreased translation, but rather between dilution by cell division and decreased translation.

3.4 PoXeR expression in *E. coli*

PoXeR was found in *Parvularcula oceani*, a deep ocean marine bacterium, and has been expressed in *E. coli* C43, a BL21 derivative for overexpressing toxic proteins (Inoue et al, 2016). So, the ability to express PoXeR in a wild-type strain like MG1655 was not guaranteed. Fortunately, there was no problem expressing PoXeR in MG1655 – in fact, the expression of PoXeR was much stronger than that of PR, such that it could be easily seen without even pelleting the cells (Figure 3.8). The variation in PoXeR expression was still similar to PR.

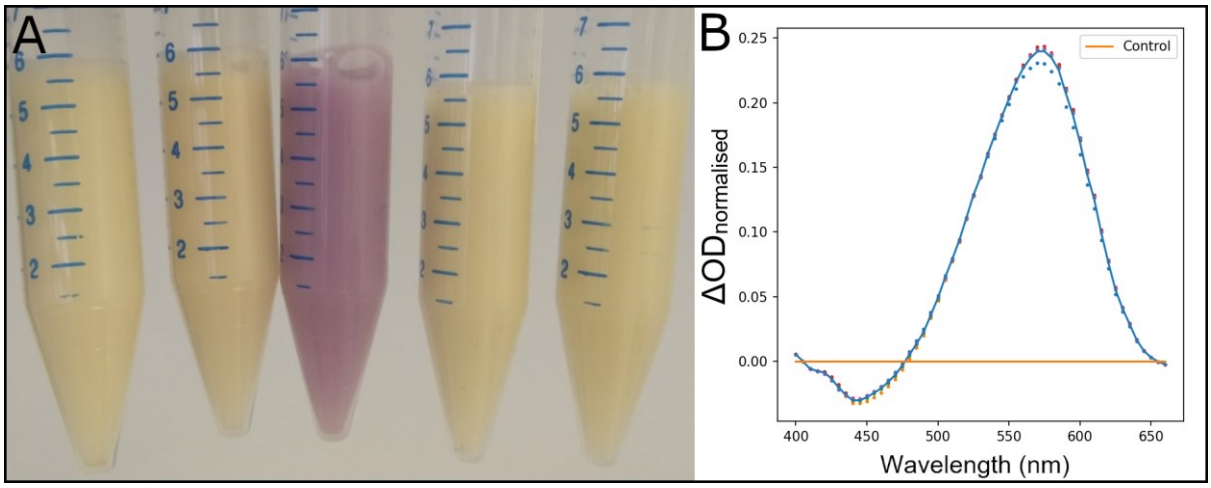

Figure 3.8: PoXeR has strong expression. (**A**) From left to right, cell suspensions of MG1655 expressing no rhodopsins, PR, PoXeR, ArchT and ChEF. The suspension with PR has a slight change in hue compared to no expression (more evident in person), but PoXeR expression is much stronger. (**B**) Absorption spectrum of PoXeR-expressing cell lysate. The absorption is much stronger than that of PR in Figure 3.7.

3.5 ChEF, ChIEF and NpHR expression in *E. coli*

ChEF and ChIEF are chimeric channelrhodopsins engineered from channelrhodopsins 1 and 2 from the green alga *Chlamydomonas reinhardtii* and have been expressed in mammalian cells (Lin et al, 2009). Very few eukaryotic channelrhodopsins (Doi et al, 2017) and rhodopsin pumps (Kikuchi, et al 2021) have been expressed in *E. coli* before, but whether this is due to a lack of trying or a specific biological reason is shrouded in mystery due to the lack of reporting negative results.

Based on correspondence with Georg Nagel, an author behind several rhodopsin studies, most microbial rhodopsins end up in inclusion bodies when expressed in *E. coli*. Among the many conditions that affect inclusion body formation, reducing protein expression rate has been shown to be able to reduce inclusion body formation and increase soluble protein levels (Jhamb & Sahoo, 2012). The vast majority of rhodopsin studies in *E. coli* use the BL21 or similar B overexpression strains, so my hypothesis was that expressing these rhodopsins at a more modest level avoids inclusion body formation and may lead to successful expression.

NpHR, in turn, was found in *Natronomonas pharaonis*, an extremophilic archaeon (Bivin & Stoeckenius, 1986), and has since been expressed in *E. coli* several times (Tsukamoto et al, 2012; Tu et al, 2018), but only in BL21 and BL21 derivatives. Trying to express these rhodopsins in MG1655, I could not observe any pigmentation, meaning there was either no or low functional expression (Figure 3.9). Likewise, I could see no sign of expression with a spectrophotometer when testing for ChEF expression (Figure 3.12).

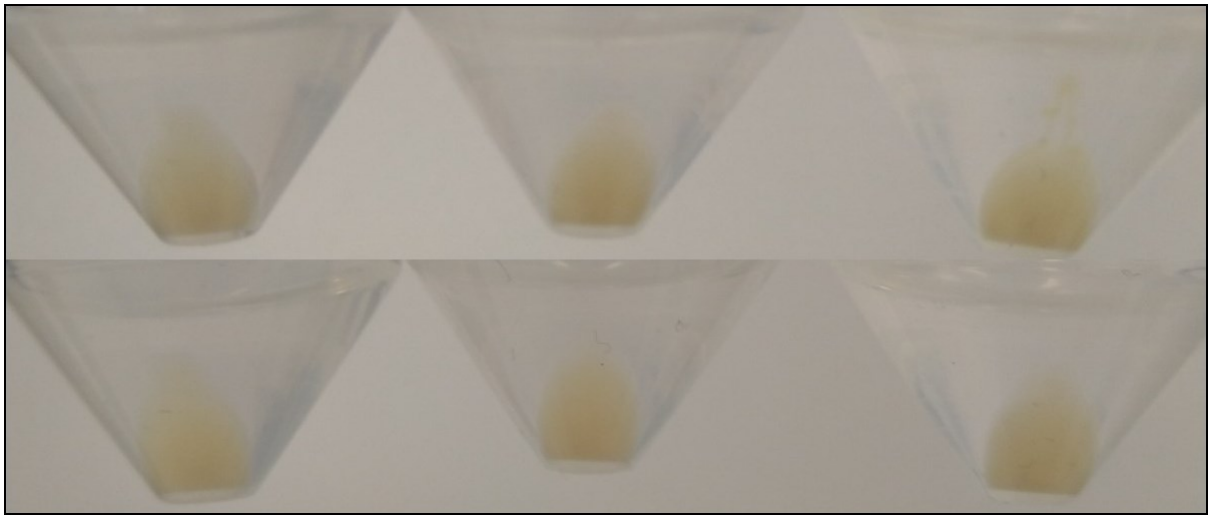

Figure 3.9: ChEF, ChIEF, ArchT and NpHR have no or low functional expression in MG1655. From left to right, pellets of MG1655 expressing no rhodopsins, ChEF, ChIEF (top), no rhodopsins, ArchT and NpHR (bottom). The lack of pigmentation indicates the lack of functional rhodopsins that absorb light.

As described in Section 3.2.2, due to the highly repetitive sequence at the beginning of ChEF and ChIEF leading to frequent frameshift mutations, I first noticed a difference in transformant colony sizes based on the presence of a functional rhodopsin gene (Figure 3.4). Later, I noticed that NpHR-expressing colonies also seemed to grow relatively small. To characterise this difference in growth, I set out to measure the growth rates of strains expressing each of the rhodopsins without mutations.

After a few inconclusive attempts, I grew each strain to the same density before inoculating liquid cultures and agar plates simultaneously. Surprisingly, each strain grew nearly identically and had same-sized colonies, with the exception of a single NpHR-expressing colony that was smaller than the others. Comparing this small colony to the other colonies from PR, NpHR, ChEF and ChIEF-expressing cells revealed a clear difference in growth curves (Figure 3.10). Although their exponential phase growth rates were similar, the small colony reached its growth capacity at a significantly lower density. This observation is consistent with the result

that PR expression is highest in early stationary phase (Figure 3.6 C): with low NpHR expression during exponential phase, there is no effect on growth rate, whereas at the optical density of OD_{600} > 1, around where PR and therefore NpHR expression peaks, cells become unable to grow.

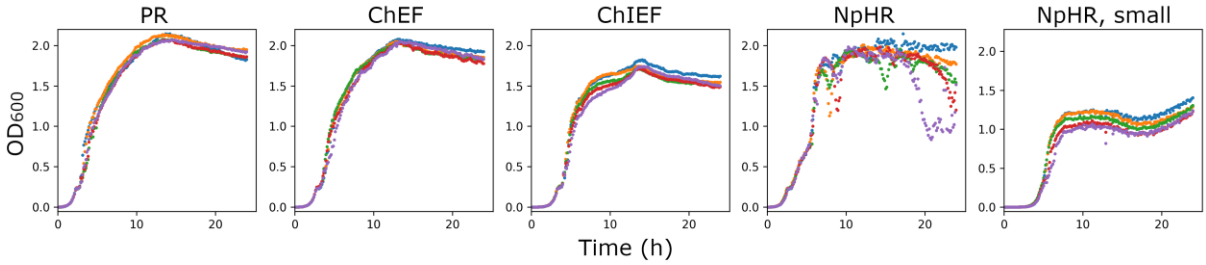

Figure 3.10: Growth curves of individual colonies of MG1655 expressing indicated rhodopsins grown in LB in a plate reader. The last sample is from a colony that grew smaller. Different colours correspond to 5 replicates. Exponential phase growth rates for samples from left to right are 1.80, 1.84, 1.85, 1.88 and 1.88 h^{-1}.

Sequencing these colonies confirmed my suspicions of what was happening: the large NpHR, ChEF and ChIEF-expressing colonies had severe mutations, disabling the gene while restoring their capacity for normal growth, while the PR-expressing colony had no mutations, as PR does not inhibit growth. The sequencing result from the small colony appeared unsuccessful at first glance. It started with a clear signal which abruptly became illegible shortly before the start codon. Upon closer inspection, I noticed that the signal was a superimposition of two different DNA sequences. By manually subtracting the expected NpHR DNA sequence from the chromatogram (Figure 3.11), I extracted a second DNA sequence perfectly matching an IS1 family transposase. This suggests that the progenitor of the colony had a non-mutated NpHR gene, and somewhere between the onset of the colony and plasmid extraction, a transposon insertion disabled NpHR, giving the host enough of a selective advantage to spread the mutation within the last group of cells expressing non-mutated NpHR. In summary, expressing ChEF, ChIEF and NpHR in

wild-type *E. coli* yields no functional rhodopsins but instead causes a growth defect, leading to spontaneous loss-of-function mutations that restore normal growth.

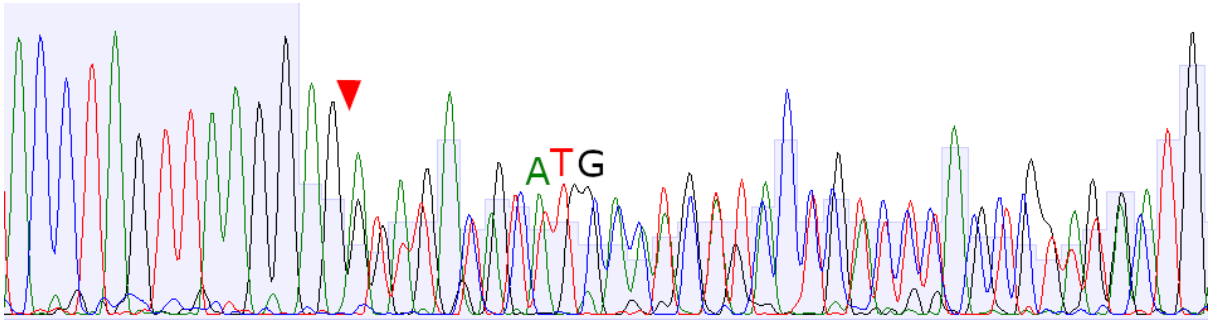

Figure 3.11: The chromatogram of the NpHR gene around the insertion site of an IS1 transposase. The presence of green, red, black, and blue peaks signifies adenine, thymine, guanine, and cytosine bases in the DNA sequence, respectively. The red arrow marks the insertion site, after which two superimposed signals are present. The start codon of the NpHR gene has been highlighted as “ATG”.

3.6 Chrimson expression in *E. coli*

Chrimson was found in the green alga *Chlamydomonas noctigama* and has been expressed in various eukaryotic cells (Klapoetke et al, 2014). Much like ChEF, ChIEF and NpHR, Chrimson seems to cause a growth defect in *E. coli* NEB 5-alpha. However, the growth of Chrimson-expressing cells could not be further analysed, as there was no growth to measure. At first glance, it seemed like the cloning of Chrimson was unsuccessful, with all transformants having no or a mutated Chrimson gene. But, as described in Section 3.2.2, I identified a pattern of different groups of transformants, where some rhodopsins, when transformed successfully, caused a growth defect. Transformation with Chrimson yielded the same number of normal-sized colonies as ChEF and ChIEF, and looking very closely at Figure 3.4, the only difference between the three is that the small colonies expressing non-mutated rhodopsins are completely absent with Chrimson. This suggests that out of the

hundreds of cells that received an intact Chrimson gene, none could grow well enough to establish a colony.

I did not settle for a mere assumption, of course, and probed for the presence of Chrimson in each of the 20 white colonies from the transformation, as well as let the cells grow for three times as long as the others to make sure there are no colonies that are growing very slowly. No new colonies appeared after the extended growth time, and based on colony PCR, only 5 of the 20 colonies contained Chrimson. Further, sequencing these 5 colonies revealed that all had an early frame shift mutation, reinforcing the hypothesis that Chrimson expression in *E. coli* is highly deleterious.

3.7 ArchT expression in *E. coli*

ArchT was found in *Halorubrum* strain TP009, a halophilic archaeon, and has been expressed in eukaryotic cells (Han et al, 2011). Although I could find no record of ArchT being expressed in bacteria, a close homologue, Archaerhodopsin-3 from *Halorubrum sodomense*, has been successfully expressed in *E. coli* BL21 (McIsaac et al, 2014), meaning the chance of functional expression in wild-type *E. coli* was at least higher than that of the algal rhodopsins that were never expressed in bacteria. Despite this, I could see no visible pigmentation from ArchT-expressing cells (Figure 3.9), meaning they had either no or low functional expression. However, unlike the other rhodopsins with no pigmentation, ArchT had no negative effect on growth, suggesting that there is still a chance that some of the rhodopsin is functional. Hence, I tried to detect ArchT using the differential absorption spectra.

Though I was able to detect sub-visible PR expression using this method, I was approaching the sensitivity limit of my protocol and equipment. In comparison to the signal from PoXeR, the signal from ArchT was suspiciously similar to the other rhodopsins that had no or low functional expression, although the signal was sometimes inverted (Figure 3.12 A, ArchT vs ChEF). In fact, the shape of this signal was also similar (but higher magnitude) to the individual control (no plasmid) replicates, further suggesting this signal was not real. The small differences in cell growth and sample preparation seemed to affect the absorption spectra of the samples in ways that could not be normalised for, and therefore made it difficult to identify the changes in absorption spectra that are caused by low rhodopsin expression. However, on a single occasion, the differential absorption spectrum of ArchT-expressing cells resembled the action spectrum of ArchT (Figure 3.12 B & C), even if the signal was very small and approaching the magnitude of the noise. Thus, the functional expression of ArchT in *E. coli* MG1655 remains inconclusive, although for the purpose of this work, ArchT does not seem suitable either way.

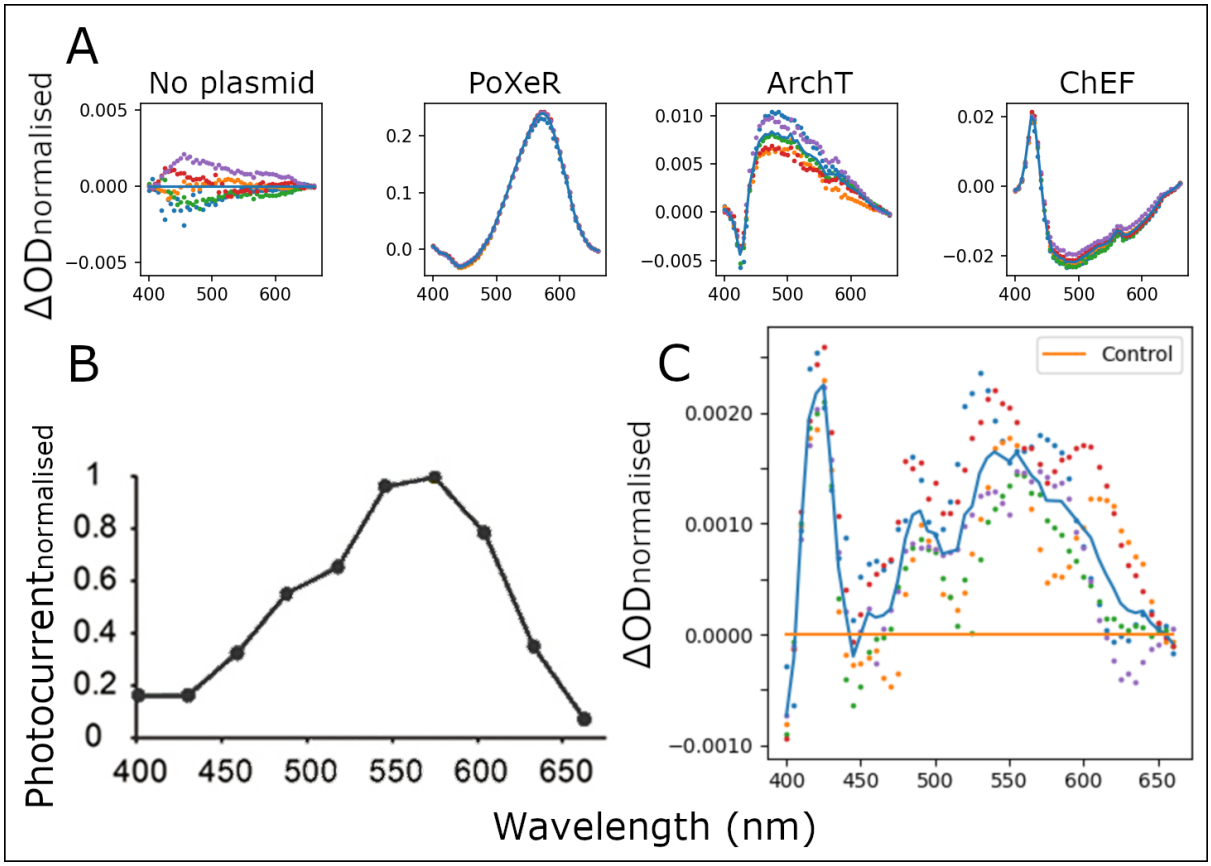

Figure 3.12: The functional expression of ArchT is inconclusive. (**A**) Typical differential absorption spectra (5 replicates plotted in different colours and mean plotted as a blue line) for indicated rhodopsins, normalised for sample concentration as described in Section 2.2.2. PoXeR serves as a form of positive control, while ChEF and the sample with no rhodopsin serve as negative controls. ArchT spectra resemble more the negative controls. (**B**) The action spectrum of ArchT (adapted from Han et al, 2011). (**C**) A single occasion of ArchT differential absorption spectra. Plotted as in (A) except the control, zero line is included. The spectra in (B) and (C) are similar, suggesting the possibility of functional ArchT expression and conflicting with the negative result in (A).

3.8 Discussion

I chose the rhodopsins for this work based on their biophysical characteristics, but the results here demonstrate the importance of choosing exogenous proteins based on their compatibility with the host before looking at their other characteristics, especially when it comes to membrane proteins. Failure to functionally express an

exogenous protein could stem from any process from transcription to protein folding and beyond.

When I first encountered the lack of expression of some of the rhodopsins, I started investigating from the beginning, looking at the frequency of rare *E. coli* codons in the genes. In theory, rare codons can halt the translation machinery that needs to wait for the rare tRNAs, which can lead to reduced gene expression (Chumpolkulwong et al, 2006). On the other hand, this pausing may facilitate the folding of certain proteins, thus increasing gene expression (Rosano & Ceccarelli, 2009). However, of all the rhodopsins in this work, PR had a significantly higher proportion of rare codons than the others, meaning the lack of expression was not due to a high content of rare codons. PoXeR, on the other hand, had the lowest fraction of rare codons, which could explain the higher expression level than PR. The other rhodopsins, that failed to express in *E. coli,* vary anywhere from a lower, near-native and higher levels of rare codons, suggesting the fraction of rare codons by itself is not responsible for the lack of expression.

To negatively affect growth, like most of the rhodopsins in this work, the gene at the very least manifests into an amino acid sequence. Hence, the most likely problem is with the proper folding of the protein, which could be affected by translation, the chemical composition of the cytoplasm, enzymes that act on the protein and the correct localisation of the protein (Rosano & Ceccarelli, 2014). Inefficient folding or poor stability of the folded protein leads to the accumulation of unfolded proteins, which may aggregate to form inclusion bodies or become targets for proteolysis (Balch et al, 2008). Further, even in its folded state, a heterologous protein may be toxic to its host.

ChEF, ChIEF and Chrimson are algal rhodopsins that have not been expressed in *E. coli* before. Algae, unlike bacteria, perform a wider range of post-translational protein modifications that play a role in folding and controlling their target proteins (Ahmad & Bano, 2019). Among algal post-translational modifications, glycosylation plays a crucial role in protein folding, possibly by destabilising the unfolded state, consequently reducing the free energy needed to exit the unfolded state (Shental-Bechor & Levy, 2008). It is likely that these algal rhodopsins require such post-translational modifications for efficient folding. Consistently, the predicted protein structures using AlphaFold (Jumper et al, 2021) show an increasing amount of disordered extracellular domains inversely proportional to the level of success in functionally expressing each protein (Figure 3.13). PR and PoXeR, with the smallest extracellular domains, expressed well in MG1655. ArchT, with slightly larger extracellular domains did not express well, but also did not inhibit the growth of the host. NpHR, with even more complex extracellular domains, caused a growth defect, but one that I did not notice as early as ChEF and ChIEF. NpHR has also been expressed in the more suitable expression strain BL21, unlike the algal rhodopsins. ChEF, ChIEF and Chrimson have the most complex extracellular domains in comparison and have had no successful expression in *E. coli* beyond this work. ChIEF and ChEF only differ by one amino acid, and although the structure prediction for Chrimson failed, the crystal structures of Chrimson and ChEF are highly similar (Oda et al, 2018). Hence, to express these algal rhodopsins in *E. coli*, the best strategy may be to engineer a strain that can perform simple glycosylation, although it may be easier to engineer a readily suitable rhodopsin to have the desired biophysical characteristics instead.

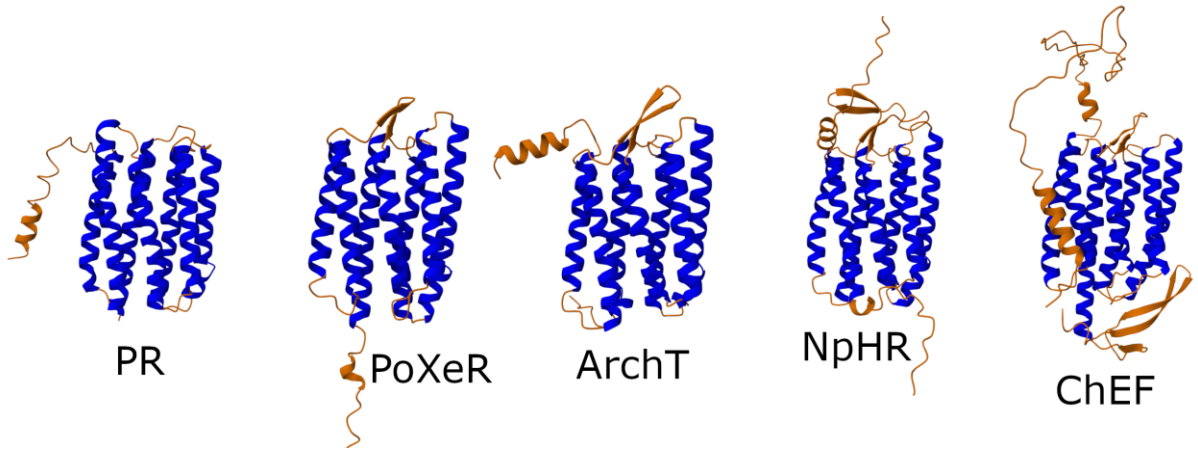

Figure 3.13: Predicted rhodopsin structures display a pattern of increasing extracellular domain complexity. The structures predicted with AlphaFold are coloured blue for the common seven transmembrane helices and orange for the rest of the protein. The structures are all displayed in roughly the same orientation, with the extracellular side facing up.

The archaeal rhodopsins NpHR and ArchT did not have good expression in MG1655, but NpHR and a close homologue of ArchT have been expressed in BL21 (Tsukamoto et al, 2012; McIsaac et al, 2014), meaning they do not require glycosylation. The main differences between MG1655 and BL21 proteome are the lack of Lon and OmpT proteases in BL21. These proteases preferentially degrade misfolded and foreign proteins, so their absence explains the increased expression in BL21, but not the toxicity of NpHR in MG1655 but not in BL21; the absence of a protease should not reduce the number of misfolded proteins. The formation of inclusion bodies can be associated with a reduced growth phenotype, but this association does not hold in all conditions (Hunke & Betton, 2003), so it is possible that BL21 does indeed have the same amount of misfolding and aggregation without experiencing a growth defect. It is unknown what exactly causes the growth defect, but overexpression of Lon, which is normally upregulated by the accumulation of misfolded proteins, has been shown to reduce growth in *E. coli* (Omnus et al, 2022). Hence, the continuous production of misfolding proteins in MG1655 may sustain an elevated Lon expression, causing Lon to degrade an increased amount of off-target,

functional proteins. The simpler structure of ArchT together with the absence of a growth defect suggest that a lower amount of ArchT misfolds – enough to activate the degradation of potentially folded proteins but not so much that Lon or another mechanism affects the growth of the cell.

Given that it is clearly not impossible for NpHR and ArchT to fold in *E. coli* (Tsukamoto et al, 2012; McIsaac et al, 2014), employing strategies to improve folding efficiency may yield functional expression in MG1655. The easiest way to improve the folding of difficult-to-express proteins is to give them more time to fold by reducing translation rate through a lower induction temperature (Shirano & Shibata, 1990). However, reducing the temperature to 25°C did not help expressing NpHR and ArchT. Another strategy that has been used to improve rhodopsin expression without strain engineering is to co-express the difficult rhodopsin with a highly expressing rhodopsin as a fusion protein, helping with the expression and stability of the target rhodopsin (Tu et al, 2018). While there are many strategies to improve the expression of exogenous proteins, the discovery and engineering of new rhodopsins is rapid, and looking into the diversity of bacterial rhodopsins, instead of more characterised algal or archaeal rhodopsins, may yield better rhodopsin expression and with less work.

Chapter 4

Optogenetic manipulation of cellular energetics

4.1 Introduction

As described in the previous chapter, the only rhodopsins from this work that yielded functional expression are SAR86 γ-proteobacterium proteorhodopsin (PR) and *Parvularcula oceani* xenorhodopsin (PoXeR), the bacterial light-driven proton pumps. PR pumps protons out of the cell, against the electrochemical gradient, while PoXeR pumps protons into the cell. This gives us the ability to study the effects of artificial enhancement and depletion of proton motive force (PMF). We already know that bacterial flagellar motor can be powered using PR (Walter et al, 2007), and this has been characterised in terms of controlling swimming speed, bacterial density pattern formation and the sharpness of speed transitions (Arlt et al, 2018). However, the effect of PR was only characterised in nutrient-depleted cells (no oxygen or carbon

source) in strains lacking chemotaxis and F_1F_o ATP synthase, of which the latter, as mentioned in Chapter 1, plays a crucial role in ATP and PMF homeostasis. What effects does light-driven proton pumping have on PMF in wild-type cells at different energetic states? What other effects besides altering PMF does this have? And what happens when we reverse the process to pump protons inward?

In this chapter, I will explore these questions using light to enhance and deplete PMF. I will use two different methods to quantify the PMF-driven flagellar rotation. In tethered cell assay, flagellar rotation results in the rotation of individual cells tethered to the slide from its flagella, which is detected from the cell orientation through a microscope. In differential dynamic microscopy (DDM), the average swimming speed of a large population of cells is accurately estimated by analysing differential image correlation of low-magnification images recorded under a microscope.

4.2 Tethered cell assay

The tethered cell assay is a very useful technique for studying flagellar motor activity, and has served its purpose numerous times (Silverman & Simon, 1974; Qian et al, 2013). However, as hinted by the use of another technique later in this chapter, I discovered that tethered cell assay was not suitable for my work. As such, this section will focus more on the experimental requirements for studying the effects of light-driven proton pumping on cell energetics and physiology, and how these are not all met using tethered cell assay.

4.2.1 Motility optimisation

As detailed in Section 2.3.1, I used three different growth conditions (using LB, TB and RDM) that have previously yielded motile cells. Unexpectedly, RDM, the only defined medium out of these, was the most inconsistent and unreliable growth medium. While it sometimes yielded sufficiently motile cells, the cells often had poor motility and displayed filamentation (Figure 4.1); a result of stress-induced block of cell division (Cayron et al, 2023). Numerous types of stress can be responsible for filamentation, but the most likely growth medium-related ones are pH and osmotic stress, and starvation. The growth conditions with LB and TB did not have these issues, and both yielded highly motile cells, LB performing better than TB. However, as explained in Section 2.3.1, LB and TB can lead to an unpredictable physiological state of the cells, leading to poor reproducibility, so their best use is for optimising the experiment.

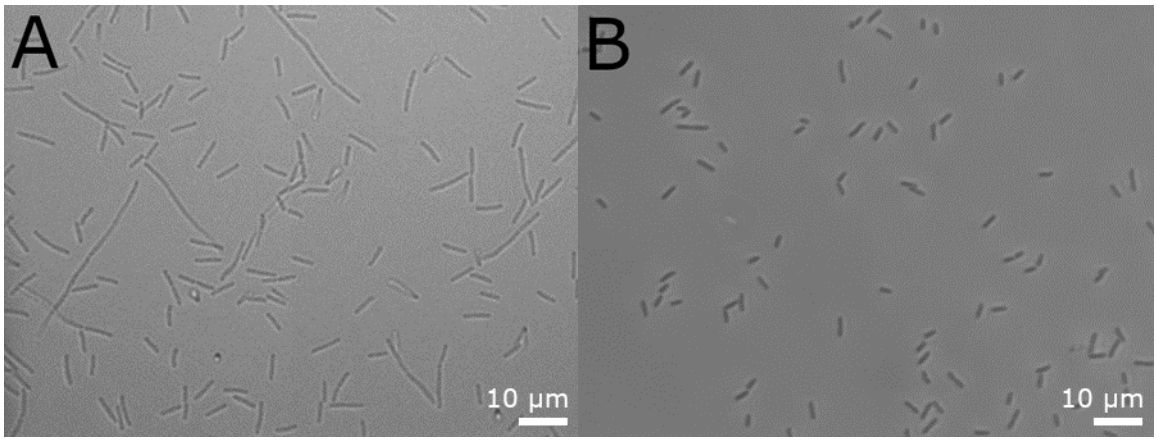

Figure 4.1: RDM causes stress-induced filamentation. (**A**) A microscope image of EK01 cells grown in RDM. Filamentation as seen in the image was present frequently but not always. (**B**) For comparison, a microscope image of healthy EK01 cells grown in LB.

The bacterial flagellar filament consists of thousands of fliC subunits (Nedeljković et al, 2021), so when the cell contains the fliC^{sticky} mutation, the flagella become “sticky” throughout the filament. Therefore, when this cell attaches to the

glass slide from its flagellum, the point of attachment can be anywhere along the filament, causing variability in the radius of rotation and hence the rotation frequency. To counter this, it is common practice to shear the flagellar filaments, as a shorter filament has fewer possible points of attachment. However, this seemed to reduce the motility of my cells. Investigating the ideal number of times to push the cells through the shearing device, not only did I notice that the cells easily became less motile, but that I could not observe significant differences between the cells that did rotate. Perhaps, the custom to shear the filaments originated from the bead assay, where flagellar motor rotation was detected using a polystyrene bead stuck to the sticky filament. A small bead can only attach to the filament from one, random point, whereas a glass slide might attach to the filament throughout its length, thus reducing the variability in the radius of rotation. Regardless, not shearing the filaments yielded better motility without compromising the experiment.

4.2.2 Light intensity requirement

To test the ability of PoXeR to deplete PMF, I just needed to illuminate the sample with wavelengths of the green spectrum and observe the decrease in flagellar rotation speed. However, doing so with the maximum light intensity of the microscope had no significant effect on flagellar rotation (Figure 4.2). I measured the intensity of the light source on the sample plane, getting 4.3 mW/cm^2 without filters, 2.9 mW/cm^2 after filtering wavelengths below 515 nm. Comparing this value with previous experiments using PR (Walter et al, 2007; Schwarz-Linek et al, 2016), 2.9 mW/cm^2 is not enough to gauge rhodopsin activity. So, besides finding a better

growth condition for the experiment, I also needed an optical setup with a stronger illumination.

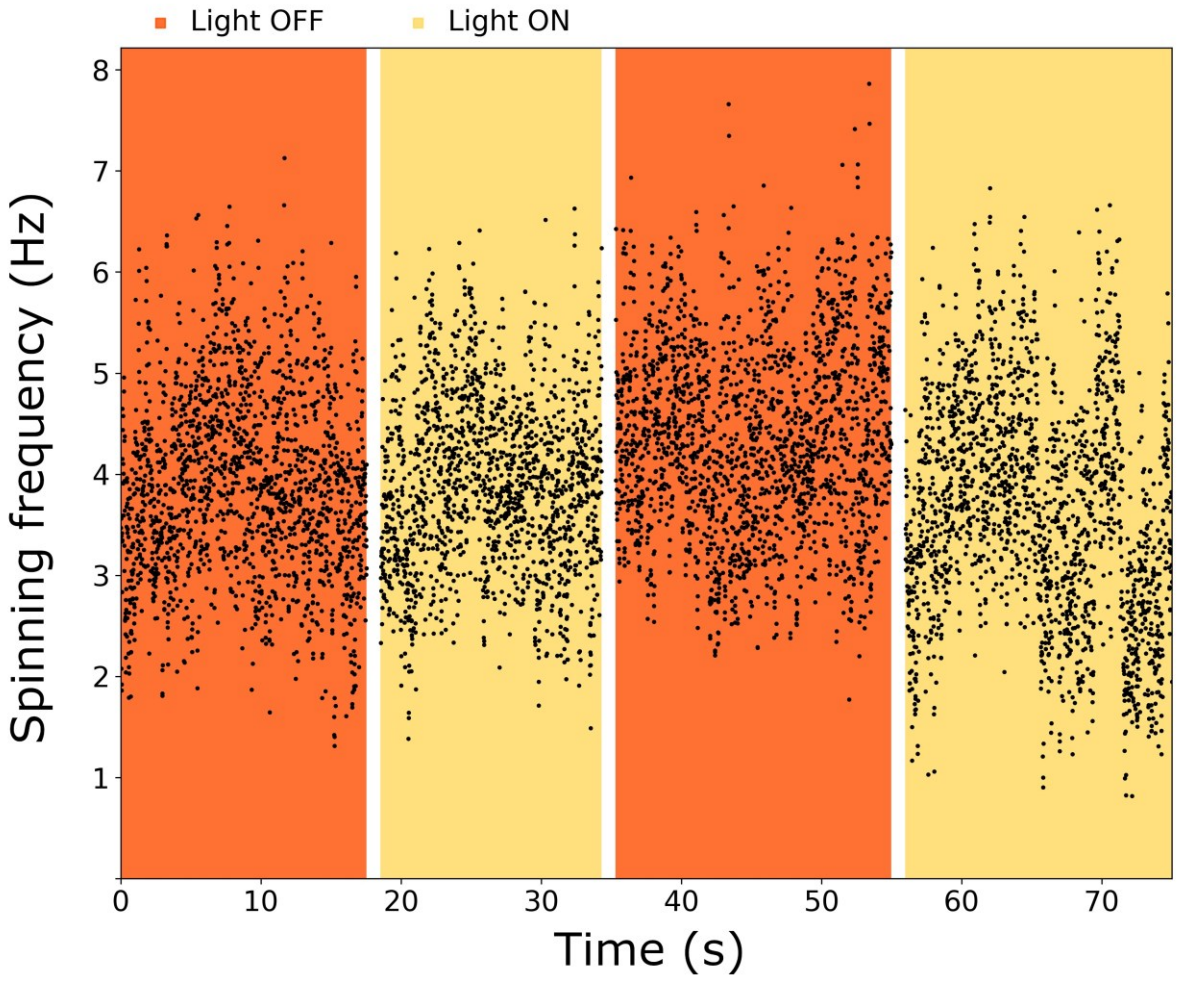

Figure 4.2: The effect of light on the spinning frequency of PoXeR-expressing EK01 cells in PBS + 0.1 mM glucose. 4.3 mW/cm^2 of light from a halogen lamp with either a 515 nm (yellow background) or 645 nm (orange background) longpass filter was used to illuminate the sample. The average spinning frequency of motile cells (grown in LB) is plotted for each time point (black dots). The 645 nm filter blocks the light utilised by microbial rhodopsins, leaving only the red light for imaging.

4.2.3 Oxygen depletion time

While solving the problems outlined so far, there was one further obstacle to overcome. To observe the effect of PR on cell energetics, the cells cannot undergo respiration, as the PMF maintained by respiration is higher than the maximum PMF

that PR can establish (Walter et al, 2007). One way to achieve this would be to use azide, a respiratory inhibitor. However, azide has effects on the wider physiology of the cell, such as inhibiting the F_1F_o ATP synthase (Noumi et al, 1987), so is not an ideal solution for studying the effects of proton pumping on cell physiology. The better approach to stop respiration is to deplete oxygen from the sample. By using previous experiments of oxygen and glucose depletion in *E. coli* (Schwarz-Linek et al, 2016), we can control, estimate and identify the depletion of oxygen and glucose to control whether the cells are undergoing respiration, fermentation or endogenous metabolism, i.e., recycling of endogenous carbon sources in the absence of external carbon.

Following the results from Schwarz-Linek et al (2016), I washed my cells in Berg's motility buffer (BMB) with limited oxygen and excess glucose, and followed their motility without any green light illumination. Even after 3 hours of consuming oxygen, I could not observe a motility drop characteristic of oxygen depletion (Figure 4.3). Prompted by this, I calculated the theoretical oxygen depletion time for my setup. Based on various experiments with excess glucose, oxygen depletion occurs in 14–20 minutes per 10^9 cells/mL (Schwarz-Linek et al, 2016). My image size is 640x480 px, so with 0.183 μm/px, the volume of the imaged sample is $117\mu m * 88\mu m * 100\mu m = 1.03 * 10^{-6} mL$. Since gravity ensures most cells attach on one side, and untethered cells are flushed out, most cells in this volume are on the image plane. With 100 cells in field of view, the cell concentration reaches roughly 10^8 cells/mL, which would take 140–200 minutes to deplete oxygen. In reality, the image will likely contain less than 100 cells, and with any more cells, the proportion of cells touching each other increases, thus reducing the number cells usable for analysis. Unable to increase the cell concentration, having to wait for more than 2 hours in the

best case poses its own problems. First, over long time periods, many cells become untethered, reducing the number of cells that can be followed throughout the experiment. Further, the physiology of the cells likely undergoes changes during the long wait, making this method non-ideal.

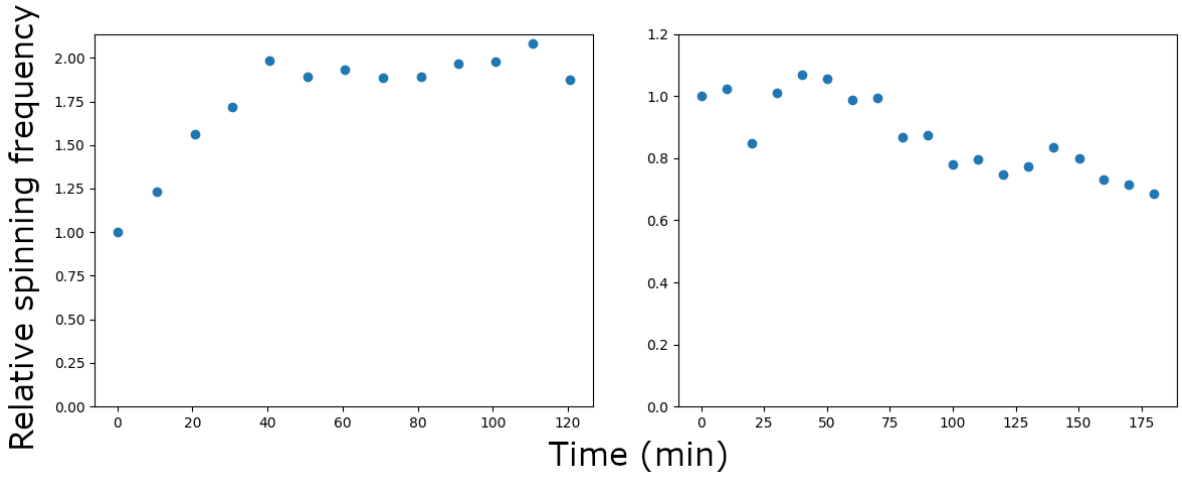

Figure 4.3: Oxygen depletion in tethered cell assay can take over 3 hours. The spinning frequency of each motile EK01 cell (grown in LB) relative to its initial frequency in PBS + 0.1 mM glucose (left) or BMB + 20 mM glucose (right) was averaged for each time point, and is plotted for two separate experiments. While both experiments show some trends in motility, neither trend is characteristic to oxygen depletion.

4.3 Differential dynamic microscopy

Taking everything from tethered cell assay into account, I changed my growth conditions, illumination setup and sample concentration. The MOPS-based medium from Cremer et al (2019) yielded high motility while avoiding the RDM-associated issues described in the previous section. The new illumination setup improved the maximum light intensity from 2.9 to over 200 mW/cm^2, and not having to distinguish individual cells gives more freedom to adjust cell densities to control oxygen depletion.

4.3.1 Optimising the experiment

As I began to measure the two key variables that I can probe, the swimming speed and oxygen depletion rate, I quickly noticed that there are additional parameters that needed to be controlled. The first, rather obvious parameter was the age of the sample since collection from its growth condition. The older the sample, the less motile it became (Figure 4.4 A). To create a constant supply of fresh samples, I started growing the cells in a microbioreactor with a turbidostat, periodically diluting it to maintain an OD_{600} of 0.3. The bioreactor could maintain a supply of fresh samples, but with the continuous requirement to dilute the sample, I sought out a growth medium with slower growth to expand the time window where the optical density can be maintained without running out of media. Using M63 minimal medium with glycerol as the carbon source indeed slowed the growth rate from 1.0–1.1 (slowest – fastest replicate) h^{-1} with the MOPS-based medium to 0.32–0.39 h^{-1}, but resulted in poor motility (Figure 4.4 B). The cells looked stressed, displaying an elongated phenotype (like in Figure 4.1 A), which is likely linked with the poor motility. Switching the carbon source to glucose resulted in a growth rate of 0.78–0.80 h^{-1} and a better motility than with glycerol, but not as good as with MOPS (Figure 4.4 C). However, when switching the sample from PoXeR-expressing cells to the control cell line expressing GFP instead, motility collapsed entirely (Figure 4.4 D). Growing these cells simultaneously in the bioreactor and a normal flask showed that the non-motility was exclusive to the sample grown in the bioreactor. A potential mechanism for the bioreactor-associated non-motility could be the shearing of flagella by the fast rotation of the magnetic stirrer, but why it happens only in one medium and one strain is a mystery.

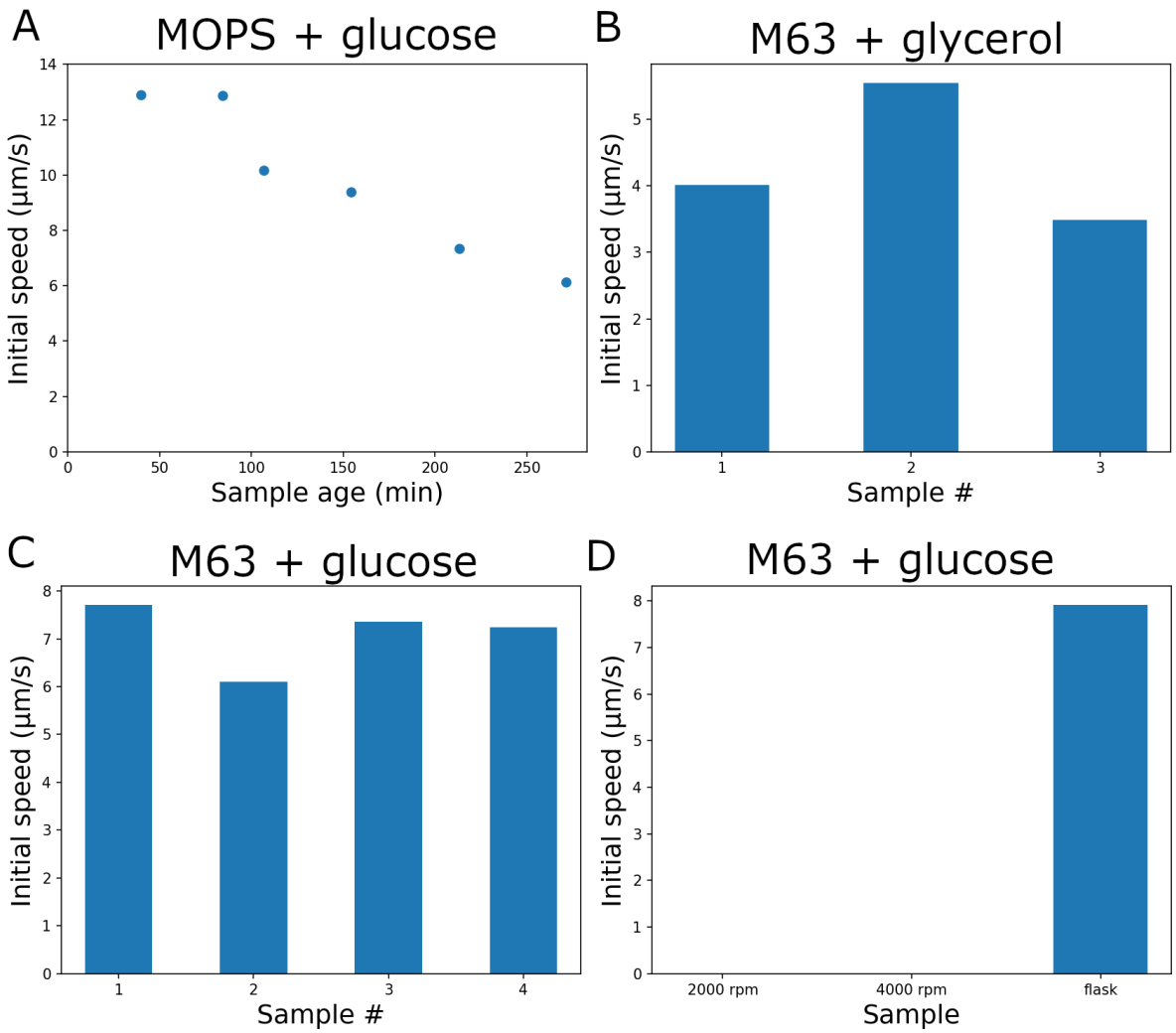

Figure 4.4: Bacterial motility at different stages of experiment optimisation. (**A**) The initial swimming speed of PoXeR-expressing (non-illuminated) cells decreases over time, where sample age indicates how long the cells have been in BMB at room temperature in a closed test tube. (**B**) The initial speed of different fresh samples of GFP-expressing cells grown in the microbioreactor. (**C**) The initial speed of different fresh samples of PoXeR-expressing cells grown in the microbioreactor. (**D**) The initial speed of fresh samples of GFP-expressing cells grown either in the microbioreactor at indicated stirring speeds or in a conical flask in a shaking incubator. The growth media for each experiment are indicated on top of the figure.

If I could not use the bioreactor turbidostat to maintain the sample at a constant optical density, I had to do it manually. I simply had to calculate how much the sample will grow during my next experiment and dilute accordingly. This worked out exceptionally well, and I could return to using the MOPS-based growth medium that gave the best motility. However, oxygen depletion time was still unpredictable. One of the hardest parts to perform consistently during my sample preparation was

concentrating the sample to an OD_{600} of 15–30 to allow the experiment buffer to be free of bacterial nutrient consumption until the very moment the experiment begins. I decided to test how the high optical density during this step affects the cells by purposefully concentrating the sample to different densities and waiting 10 minutes before diluting them in the experiment buffer at the same optical density. Although there was no difference between the oxygen depletion rate at low and medium concentrated densities, concentrating to the higher range of typical densities caused the sample to consume oxygen considerably slower (Figure 4.5). The stringent response, which I introduced in Section 1.4, is known to decrease respiration rate (Smirnova et al, 2018), so it is possible that the observed changes are a result of stringent response activation due to the rapid depletion of limited nutrients during the concentrated state.

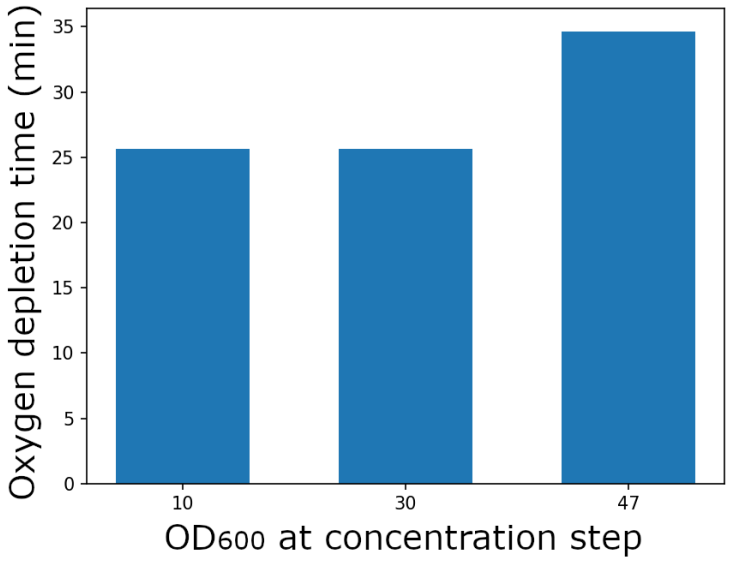

Figure 4.5: High concentration of cells reduces subsequent oxygen consumption rate. Samples of MG1655 were concentrated to above optical densities, kept in said concentration for 10 minutes and then diluted to OD_{600} of 0.5 in BMB + 1 mM glucose. Oxygen depletion time is the time between introducing the sample to BMB and the drop in swimming speed characteristic of oxygen depletion.

While minimising the time the sample spends in the concentrated state and avoiding the higher concentrations helped reduce the variability of the sample, it became clear that the precise physiological state of the sample was very sensitive to external, hard-to-control factors (Figure 4.6). One further factor that I could control, however, was the spatial homogeneity of the experiment environment.

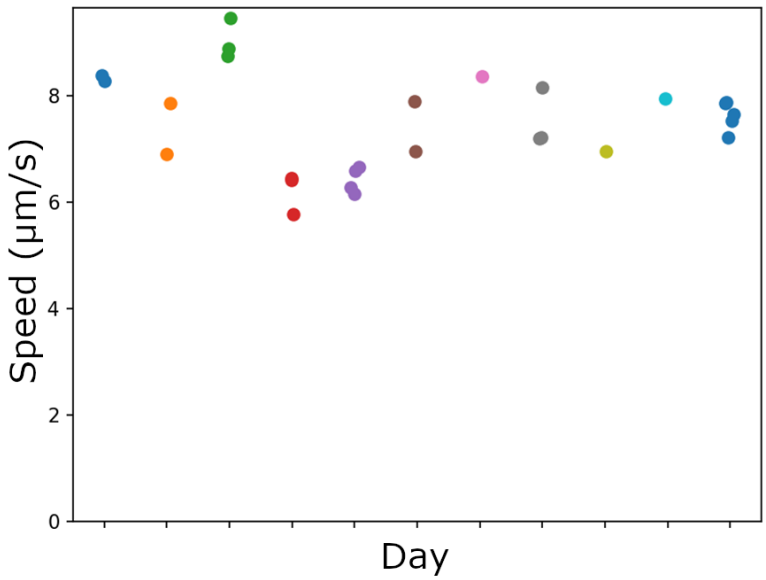

Figure 4.6: Cell motility displays considerable day-to-day and sample variability. The average (of multiple time points) swimming speed of fermenting non-illuminated populations is plotted for experiments conducted across 11 non-consecutive days. Each point represents an individual experiment.

As reported by Arlt et al (2018), a spatial pattern of cell motility results in an inverse pattern of cell density. This was visible to bare eyes, where previously illuminated areas of PR-expressing cells became clear due to decreased cell density (Figure 4.7), and the opposite was true with PoXeR. Having a spatial density pattern due to differential motility makes it hard to control the cell density in the area of interest, creates a physiological bias within the sample population, where motile cells migrate to dense areas and less motile cells stay behind, and leads to non-illuminated areas affecting the measurements in the illuminated area due to free movement between the two. The simple solution was to illuminate the entire sample.

To maintain the required high light intensity over a much larger area, however, was not trivial due to the sheer increase in required power. To meet the power requirements, I acquired an LED module consisting of 3 LED units (Figure 4.8 A), but due to the off-center location of each individual LED in the module, paired with physical limitations, I could not produce a bright and wide enough beam of collimated light on the sample plane because light from off-center points collimated by a lens travel in different directions. By giving up the collimation of light, I achieved the required illumination by simply bringing the LED module close to the sample with a minimal optical setup (Figure 4.8 B). With this, I had now eliminated variation due to sample age, sample preparation – as much as possible – and due to spatial heterogeneity.

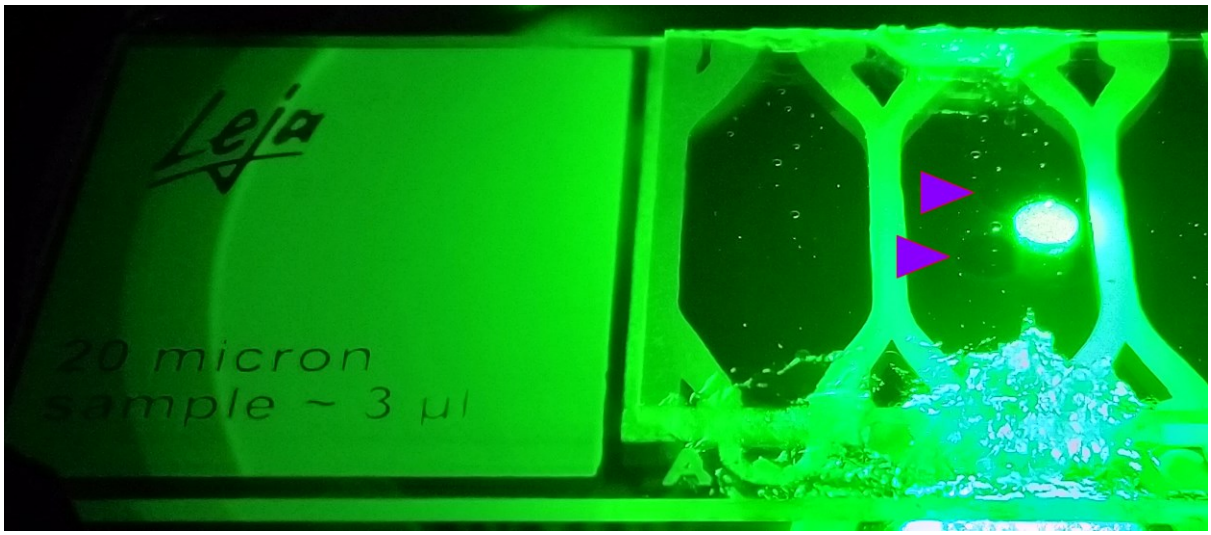

Figure 4.7: A spatial pattern of light-powered swimming results in a corresponding spatial density pattern. An image of a microchamber counting slide under a beam of green light. Purple arrows point at areas of visibly lower cell densities that were previously illuminated by the beam of light.

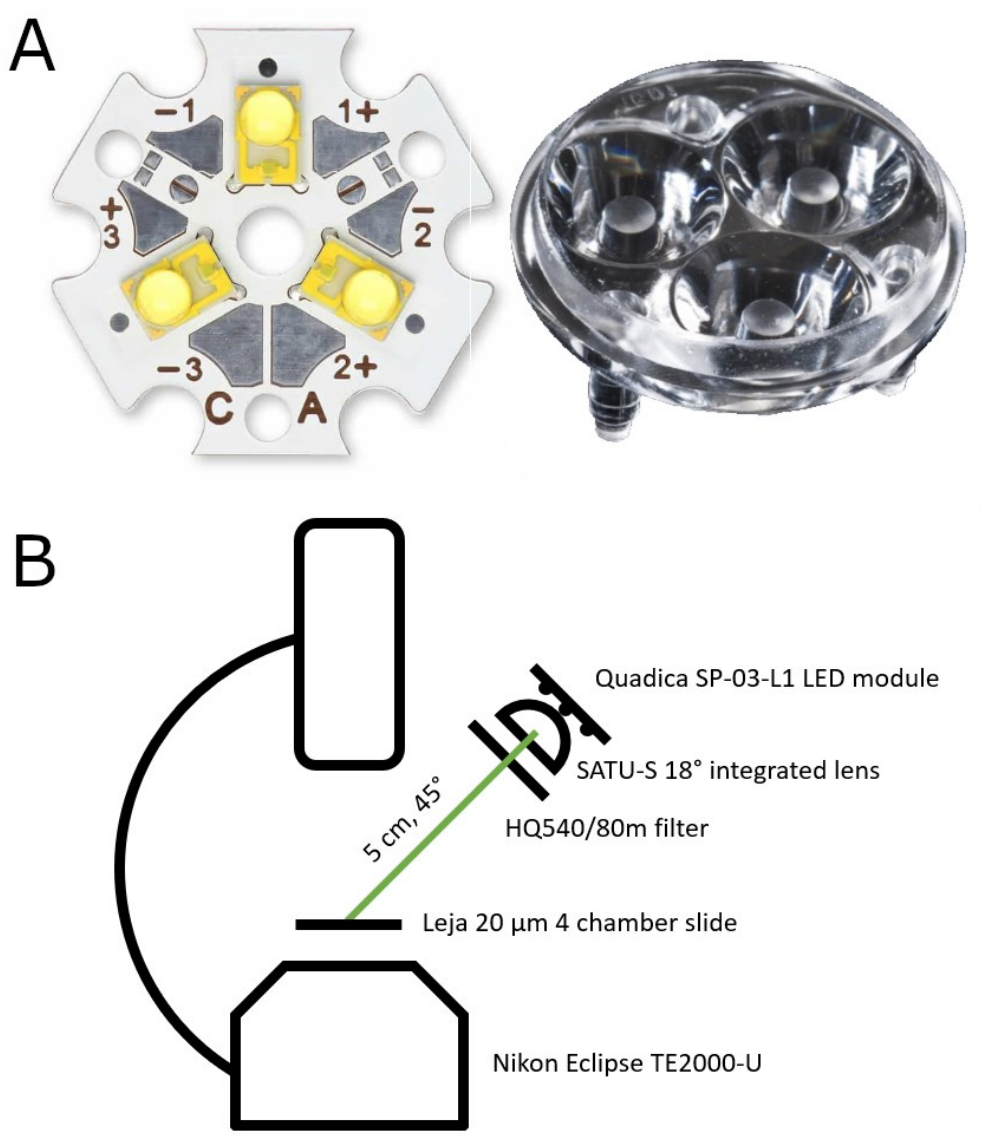

Figure 4.8: Full sample illumination was achieved using an LED module and a minimal optical setup. (**A**) An image of the LED module consisting of three LED units (left) and the integrated lens that collects the light from the LED units into a narrower light beam (right). (**B**) A schematic of the light path (green line) with the relevant components.

4.3.2 Rhodopsins affect the oxygen consumption rate of *E. coli*

During protocol optimisation, after oxygen depletion of illuminated PoXeR-expressing cells, I noticed that cells in the non-illuminated area were still swimming while freely looking around the sample. While I now know that the oxygen in the illuminated area depleted faster due to the higher cell density resulting from the spatial illumination pattern mentioned in the previous section, it gave me a hypothesis that the cell increases its respiration rate to maintain a constant PMF during inward proton pumping.

To test this hypothesis, I recorded the oxygen depletion times of samples with different rhodopsins, cell concentrations and illumination intensities. Starting with inward proton pumping of PoXeR and no rhodopsin activity, two clearly distinct patterns emerged (Figure 4.9 A), appearing as though the inward proton pumping by PoXeR did indeed increase the respiration rate. However, as I continued to record oxygen depletion times with different light intensities and opposing proton pumping directions, there were no significant differences between these conditions, including in the absence of illumination, indicating that proton pumping was not responsible for the increased respiration rate (Figure 4.9 B). Instead, looking at all the samples that either contained rhodopsins or not, it appears that the presence of any rhodopsin, regardless of illumination, causes the cells to respire roughly 50% faster (Figure 4.9 C).

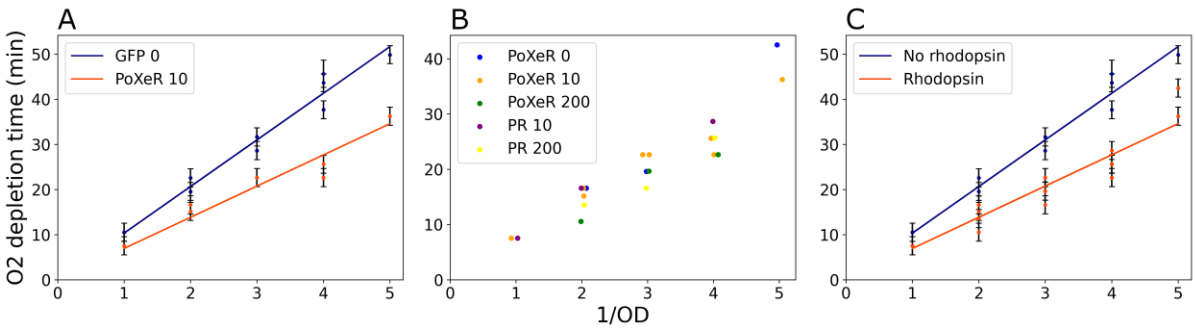

Figure 4.9: The light-independent effects of both PR and PoXeR increase the oxygen consumption rate of the cell. The oxygen depletion time of MG1655 expressing PoXeR, PR and GFP (control) in BMB + 1 mM glucose was measured at different cell concentrations and light intensities. The expressed protein and light intensity (in mW/cm^2) are indicated in legends. (**A**) Control sample plotted against the first rhodopsin condition. (**B**) All rhodopsin conditions plotted in different colours. (**C**) Control sample plotted against all rhodopsin conditions in (B). The best fit through the above data using a uniform probability distribution between the error bars indicates an oxygen depletion time of 10.33 ± 0.13 (SD) min·OD_{600} in the absence of rhodopsins and 6.92 ± 0.08 (SD) min·OD_{600} when expressing rhodopsins.

If illumination does not affect respiration rate and other potential sources of PMF, then any significant proton pumping by rhodopsins should be reflected by a corresponding change in swimming speed. The fact that illumination affected neither the respiration rate nor swimming speed of respiring cells gives us information about the activity of the rhodopsins. First, we already know that PR cannot establish a higher PMF than respiration (Walter et al, 2007), but would PR contribute to PMF maintenance or simply do nothing in respiring cells? If PR contributed to the maintenance of a constant PMF, respiration would equally contribute less through a reduced rate, suggesting that PR does not have significant contribution. Second, while PoXeR is not hindered by a high PMF due to pumping protons inward along the electrochemical gradient, the fact that we do not observe a change in swimming speed despite no increase in respiration rate implies that its inward proton pumping is orders of magnitude lower than the outward proton pumping by respiration.

4.3.3 PR and PoXeR have light-dependent effects on the PMF of non-respiring wild-type *E. coli*

Once respiration stops, we can start observing the effects of light-driven proton pumping. Since PR increases PMF, I first let the cells enter a low energy state caused by the lack of both oxygen and an external carbon source. Consistent with previous work, the swimming speed of PMF-depleted cells increases with light intensity, saturating at higher intensities (Figure 4.10 A). To test the same with PoXeR, we need a slightly different approach. Since PoXeR decreases PMF, I chose the intermediate energy state of fermenting cells, as the slower outward proton pumping by fermentation might allow us to see the effect of inward proton pumping by PoXeR, and because we cannot decrease the PMF if it is already zero due to lack of nutrients. Like the PMF increase with PR, the decrease in PMF with PoXeR increases with light intensity in a similar manner (Figure 4.10 B). These results are expected, and show that both rhodopsins have functional expression and proper light-driven proton pumping activity.

Using PR in fermenting cells also results in light-dependent effects, but the increase is smaller, as the cells already swim at 6.70 ± 1.44 (SD; n = 5) μm/s without light, and 200 mW/cm^2 illumination does not bring the speed, 8.53 ± 1.48 (SD; n = 6) μm/s, above the nutrient-depleted light-powered speed in Figure 4.10 A. Cells undergoing endogenous metabolism are at an even higher energy level and swim at a speed of 8.66 ± 0.51 (SD; n = 7) μm/s in the absence of illumination, and would therefore likely display an even smaller light-dependent increase. Using PoXeR in respiring cells had no significant effect, with swimming speeds of 16.45 ± 0.16 (SD; n = 14) and 16.30 ± 0.28 (SD; n = 12) μm/s under 0 and 200 mW/cm^2 illumination, respectively.

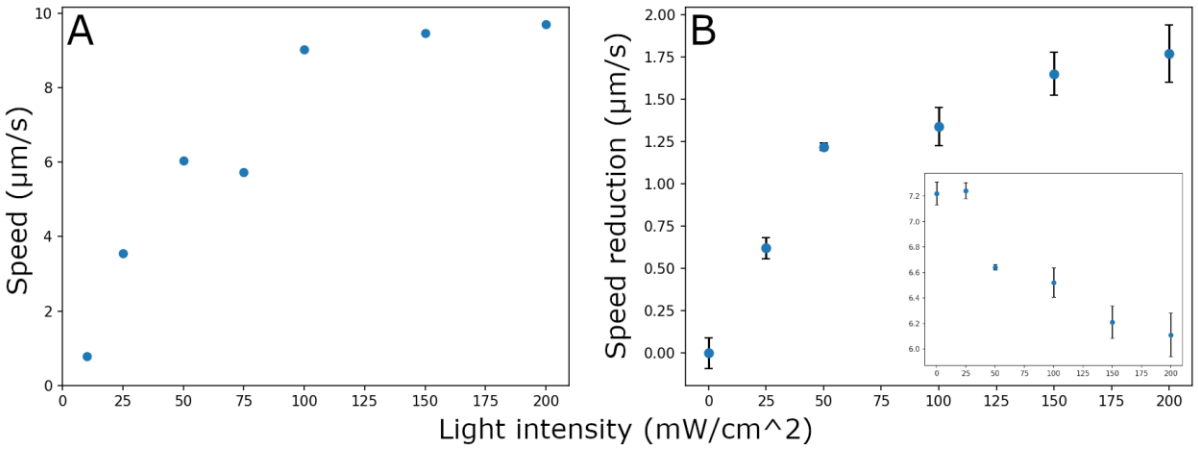

Figure 4.10: PR and PoXeR have a light-dependent effect on PMF in non-respiring cells. (**A**) PR-expressing cells were kept in BMB until oxygen depletion and then re-energised by green light illumination. After the initial boost, the swimming speed slowly increases even after an hour of illumination. Due to time constraints, I gave each sample 30 minutes of illumination, after which the speed increases very little. The swimming speed after 30 minutes of illumination is plotted (each point is one experiment). (**B**) PoXeR-expressing cells were kept in BMB + 1 mM glucose until oxygen depletion and then illuminated at various light intensities. The swimming speed quickly stabilises at a new level, and the mean ± SD of at least 3 time points (from one experiment) is plotted in inset. The pattern becomes more apparent when the swimming speeds are subtracted from the initial swimming speed after oxygen depletion in the absence of light.

4.3.4 Nutrient-depleted cells down-regulate their PMF usage

Since nutrient-depleted cells energised by PR illumination did not reach their maximum swimming speed even after an hour of illumination, I decided to test if this was a function of PR illumination time or something else. So, I energised one sample by an hour of continuous illumination while had another sample where I briefly reset PMF in between by having a brief pause in illumination. Curiously, the PMF after resuming illumination jumped straight back up to the level of the continuously illuminated sample instead of restarting the slow increase from the beginning (Figure 4.11). This implies that PR only needs a brief moment of illumination to reach its PMF equilibrium, and that the slow increase over time depends on the age of the sample instead. More specifically, if the proton pumping speed of PR does not

change, the only way to shift the equilibrium upwards is by either increasing other sources of PMF or decreasing the usage of PMF. As I never observed an increase of this magnitude without PR illumination, it seems more likely that this shift is caused by the downregulation of PMF-consuming functions such as ATP synthesis. While F_1F_o ATP synthase is capable of consuming ATP to pump protons out at low PMF, the light-powered cells do not have low PMF after illumination, making this an unlikely explanation. Instead, if F_1F_o ATP synthase was a target of regulatory activity due to nutrient depletion, inhibitory activity seems more plausible, consistent with Smirnova et al (2018).

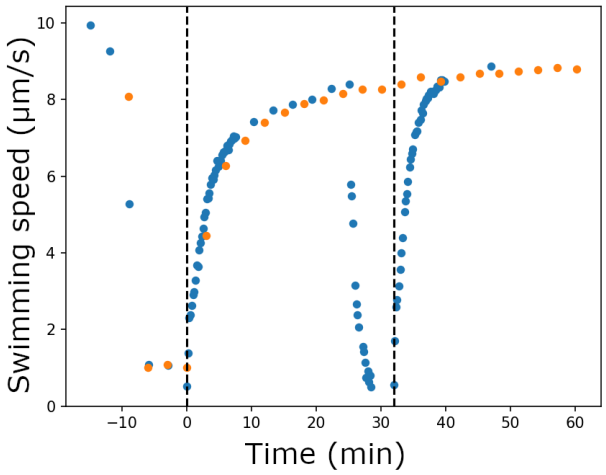

Figure 4.11: PR reaches its equilibrium within minutes while the cell undergoes a slow change shifting the equilibrium. Nutrient-depleted PR-expressing cells were powered with 200 mW/cm^2 green light either continuously (orange) or in two pulses (blue). The dashed lines indicate the illumination start times.

4.3.5 Low PR activity appears to be more efficient at maintaining than establishing a PMF

After successfully powering cells with PR a number of times, I decided to investigate the energetics when cells are illuminated from the start rather than after nutrient depletion. While studying lower light intensities, I made a rather curious observation:

while the light intensity was not enough to recover much PMF from depleted cells, it helped the cells maintain a PMF well above that which it could establish by itself for a significant duration (Figure 4.12). Ironically, this is somewhat contradictory to the hypothesis from the previous section, where nutrient depletion seems to help achieving a higher PMF by reducing PMF consumption. However, this does not necessarily refute the hypothesis, but may instead be a consequence of another mechanism more relevant to low PMF conditions. The PMF maintained by PR is still continuously dropping, so PR could help the cell preserve its last resources more efficiently or delay the time to reach the new equilibrium. This observation indicates the presence of a mechanism worth investigating closer in a future study, but by itself is insufficient to make any conclusive statements.

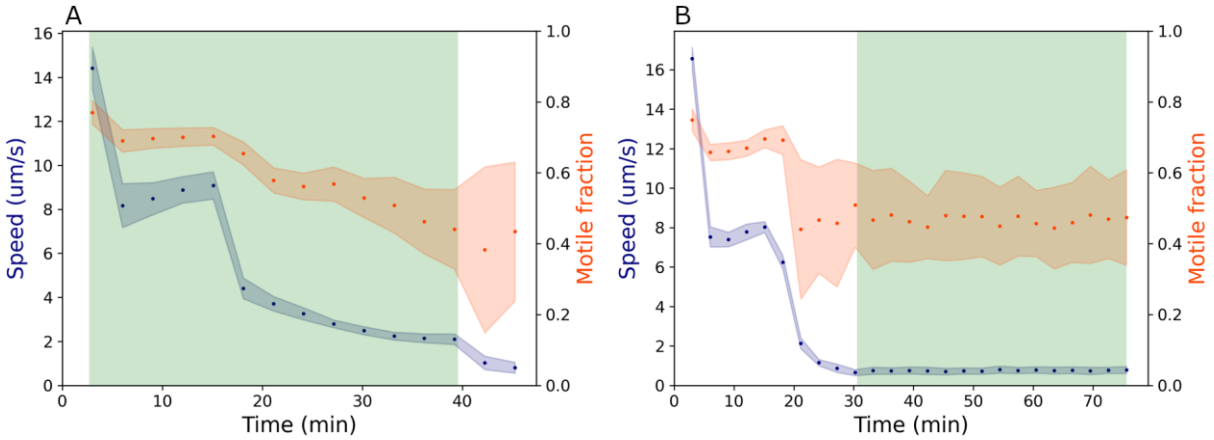

Figure 4.12: Low PR activity can maintain PMF at a greater level than it can establish. PR-expressing cells in BMB were illuminated with 10 mW/cm^2 green light from either (**A**) before or (**B**) after oxygen depletion. The first speed drop is due to depletion of residual glucose from the growth medium and the second due to oxygen depletion. To confirm that the sample was not simply more motile in (A), the speed decrease after stopping illumination is much greater than the speed increase gained from illumination in (B). Speed is plotted in blue, the motile fraction in orange and the green background indicates illumination. The error bars represent the SD of fitted parameters across different q values. Each experiment was conducted once.

4.3.6 Rhodopsin activity changes the dynamics of PMF crash due to oxygen depletion

Although light-driven PR and PoXeR activity had no significant effect on the PMF or oxygen depletion rate of respiring cells, their effects can be seen from the moment respiration stops. The PMF crash after oxygen depletion follows a fairly consistent pattern, but with the added proton pumping by PR or PoXeR, the dynamics of reaching the new electrochemical equilibrium become noticeably different. Under no rhodopsin activity, the switch from respiration to fermentation in BMB + 1 mM glucose follows a rapid drop in PMF that quickly stabilises (Figure 4.13 B). Similar to Figure 4.12 A, PR activity slows down and extends this decay (Figure 4.13 A), although this effect is much more subtle at the higher-PMF conditions of respiration to fermentation, due to the maximum PMF that PR can generate (Figure 4.10 A), than in the lower-PMF conditions of endogenous metabolism to nutrient depletion. PoXeR, unsurprisingly, makes this PMF drop steeper (Figure 4.13 C). More surprisingly, PoXeR typically drops the PMF slightly below the new equilibrium, followed by a partial PMF recovery. It appears as though the cell sometimes responds to the PMF insult from inward proton pumping and returns its PMF to a regulated level.

4.3.7 PoXeR can cause brief destabilisation of PMF in cells undergoing endogenous metabolism

While PoXeR activity in respiring cells did not display significant changes in PMF, and in fermenting cells the PMF drops and remains stable, the inward proton pumping by PoXeR sometimes displays an interesting response in cells undergoing

endogenous metabolism, i.e., in the presence of oxygen but no external carbon source. Upon illumination, PoXeR-expressing cells sometimes undergo a sharp drop in PMF and the fraction of motile cells (Figure 4.14). The PMF quickly recovers and continues to follow the usual trend in the absence of illumination, but the motile fraction remains low for as long as the cells are illuminated.

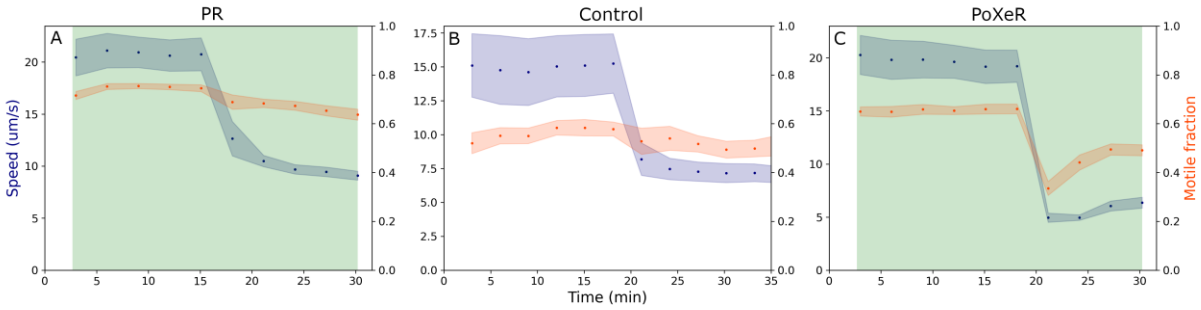

Figure 4.13: PR and PoXeR decrease and increase, respectively, the PMF decay rate after oxygen depletion. Typical motility over time curves of PR- and PoXeR-expressing cells in BMB + 1 mM glucose under 200 mW/cm^2 illumination (A & C). PoXeR-expressing cells without illumination were used as a control (B). All samples above are at an optical density of OD_{600} = 0.33. Speed (blue), motile fraction (orange), SD (error bars) and illumination times (green background) are shown. Each experiment was conducted at least three times (at OD_{600} = 0.25, 0.33 and 0.50) and showed consistent behaviour except the characteristic drop for PoXeR was missing at OD_{600} = 0.50, likely due to the early oxygen depletion.

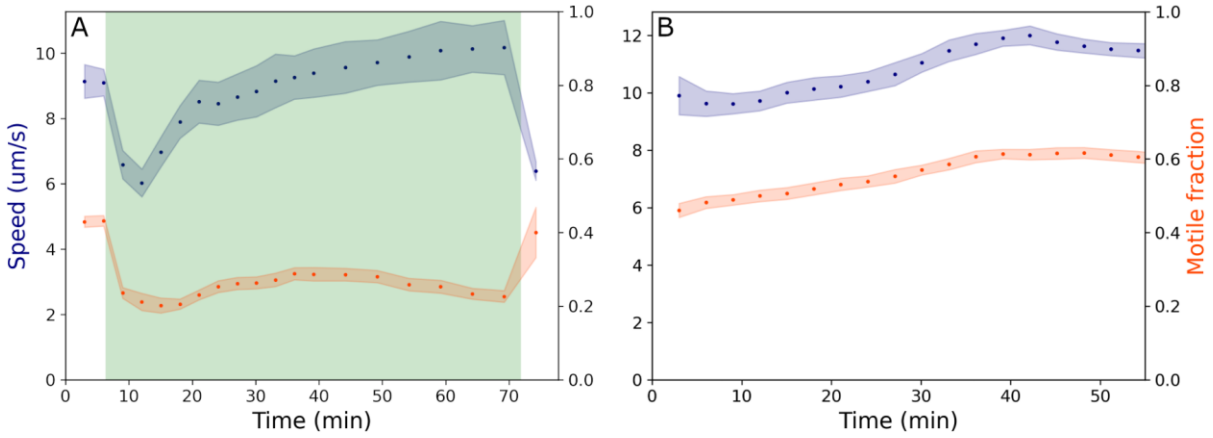

Figure 4.14: Cells undergoing endogenous metabolism may display a brief drop and recovery of PMF upon PoXeR activation. The motility of PoXeR-expressing cells in BMB at OD_{600} = 2 was monitored with (**A**) or without (**B**) 260 mW/cm^2 green light illumination (green background). Coincidentally, oxygen depletion in (A) occurs at the same time as the end of illumination, explaining the decrease in speed but not the increase in motile fraction.

This decoupling between PMF and motile fraction suggests a heterogeneous response to the decreased PMF. The fraction of cells that remain motile can clearly recover their PMF, while the non-motile fraction either stay non-motile due to not recovering their PMF or because the motility machinery has become inactive. As the motile fraction recovers after illumination ends, it seems more likely that the temporary non-motile state is due to low PMF. When interpreting these data, it is essential to acknowledge the heterogeneity among populations. Rather than having a random chance of recovery, there likely exists a fraction of the population whose PMF is below a threshold value required to stay motile and recover. Given that conditions with different energy levels result in different responses to PoXeR activity, the response is likely to be PMF-dependent.

4.3.8 The fraction of motile respiring and fermenting cells is strongly correlated with average swimming speed

Following the hypothesis that the response of individual cells depends on PMF, I collated the average swimming speeds and motile fractions of all samples within certain parameters and found a surprisingly strong correlation between the two variables (Figure 4.15). This correlation holds for samples within the same energetic environments, at least in the case of respiration and fermentation, where I had enough data to test correlation. With energetic environment, I mean the conditions that determine the dynamics of PMF homeostasis, i.e., which mechanisms act directly on PMF. In our case, the main environmental factors are the presence or absence of glucose, oxygen and light-driven ion pumping, and changing any of these broke the correlation.

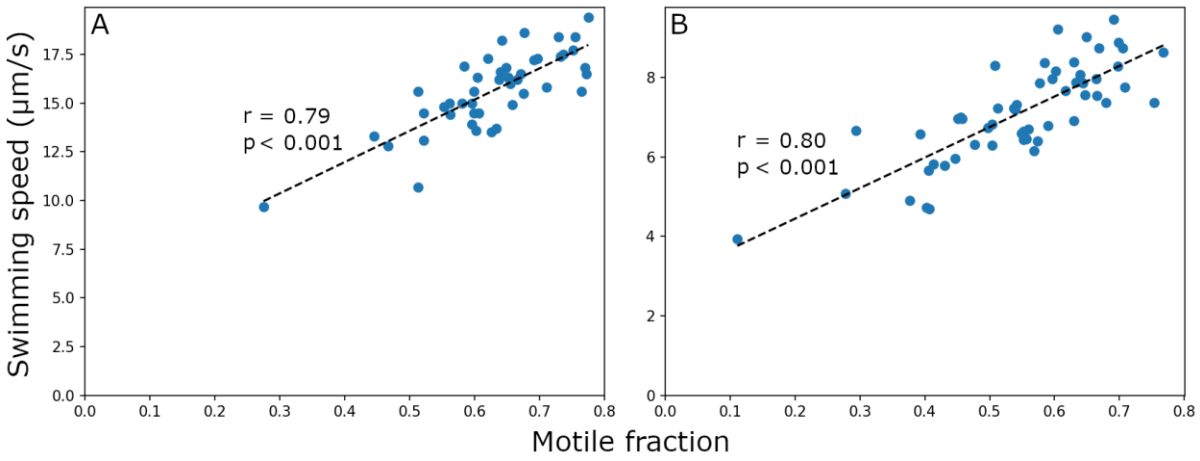

Figure 4.15: Motile fraction and PMF display strong correlation. (**A**) Respiring samples, n = 45. (**B**) Fermenting samples, n = 56. Samples expressing PR, PoXeR and GFP with 0 or 10 mW/cm^2 illumination were used. Pearson's correlation coefficient (r) and the probability that the correlation is false (p) was calculated.

To further understand the observed correlation, I looked into a recent study that investigated swimming speed and the fraction of motile cells in terms of flagellar gene expression and the number of flagella per cell (Honda et al, 2022). They used an inducer to control flagellar gene expression and found that, while PMF only varied by up to 13% across growth rates, the average swimming speed of motile cells and the fraction of motile cells correlated with the expression level of *fliA*, a sigma factor required for the expression of flagellar components, per cell (Figure 4.16 A). Although the fraction of motile cells is more affected by flagellar gene expression than the average speed of motile cells (as seen from the steeper relative slope), they are also correlated with each other (Figure 4.16 B).

So, could the variation I observed (Figure 4.15) result from differential flagellar gene expression? To look at this from another angle, I used data from an experiment where I controlled the PMF of a single PoXeR-expressing sample using several different light intensities, such that I can be confident that the changes in motility are due to proton pumping rather than gene expression (Figure 4.16 C). Plotting

swimming speed against motile fraction, although the data does not contain as many points and cover a large area, it seems like the two parameters are still correlated (Figure 4.16 D). However, when motility is controlled by gene expression (Figure 4.16 B), like the variation I observed (Figure 4.15), the motile fraction changes more than the swimming speed, displaying a similar relative slope. Conversely, when motility is controlled by PMF (Figure 4.16 D), swimming speed changes more than the motile fraction, resulting in a steeper slope. Therefore, the variation I observed resembles more the effect of differential gene expression than the effect of varying PMF. Further, this would explain why correlation between the two parameters break when including both, samples from different experiments and samples with different energetic environments: because the former changes in gene expression while the latter changes in PMF, and the two have differing effects on motility. Flagellar gene expression or flagellar integrity is likely also the reason for why the highest population swimming speeds for fermenting and respiring cells were roughly 9 and 18 μm/s instead of 15 and 25 μm/s, respectively, as seen in Schwarz-Linek et al (2016). A different gene expression could be a result of using a different cell culture protocol, while my sample preparation, which focuses on avoiding physiological changes by minimising the preparation time, may have caused more damage on motor integrity in exchange. For example, pipetting can reduce the motility of the sample (Schwarz-Linek et al, 2016).

If the variability in motility depends on gene expression rather than PMF, we must be critical in our interpretation of swimming speed as PMF. If we can control the variability of gene expression, then the relationship between swimming speed and PMF between different samples holds. But as it stands, the best comparison of PMF is within one sample at different time points. Another way to take this variability

into account is to measure the swimming speed of the sample at a defined energetic environment that can act as a reference to the gene expression level, or to use a subset of the sample to directly measure gene expression.

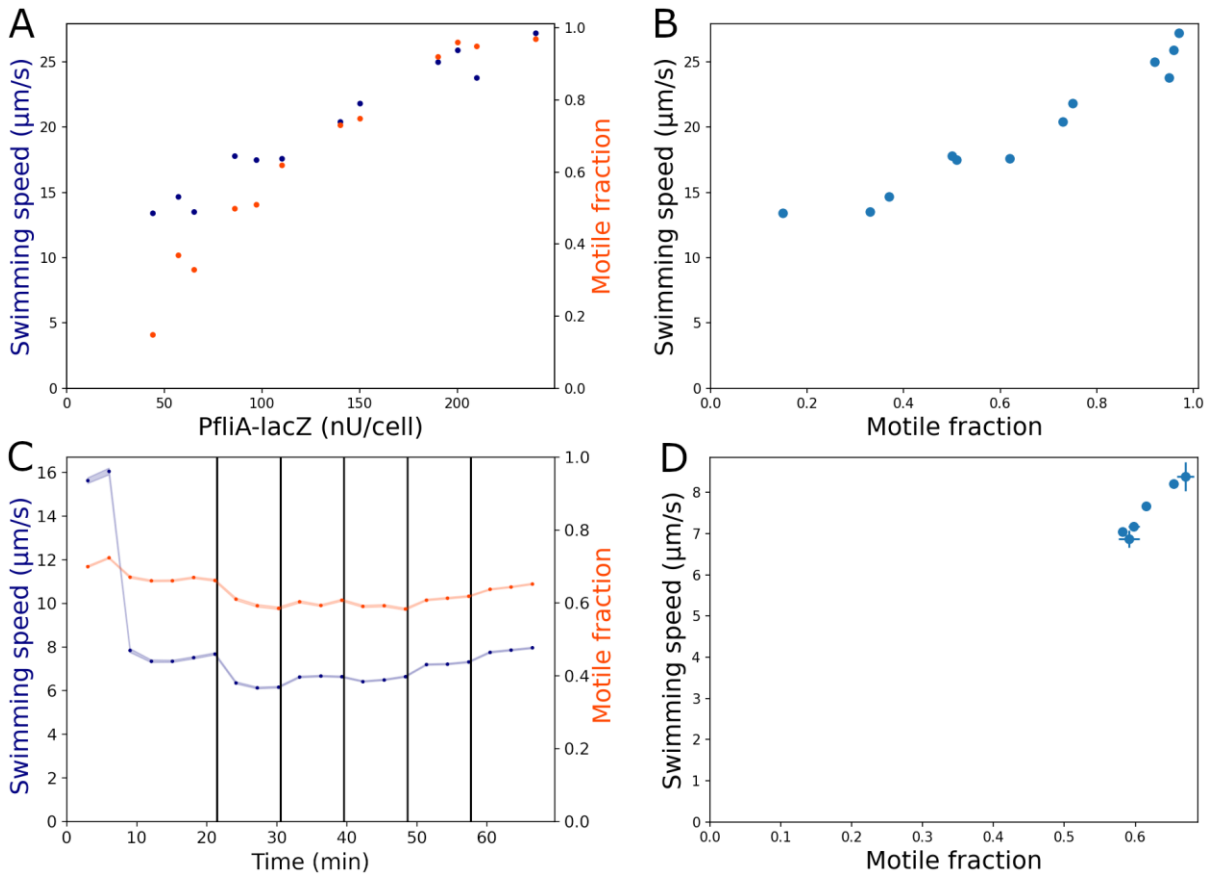

Figure 4.16: Motile fraction and average swimming speed show linear correlation when either flagellar gene expression or PMF changes. (**A**) Average swimming speed of motile respiring cells (blue) and the fraction of motile cells (orange) plotted against motility gene expression measured as LacZ reporter activity per cell encoded from the *fliA* promoter. (**B**) The data from A plotted in terms of speed against motile fraction. A and B were constructed using data from Honda et al (2022). (**C**) Average swimming speed of motile PoXeR-expressing cells (blue) and the fraction of motile cells (orange) plotted against time. The first decrease in motility results from the depletion of oxygen, after which swimming is powered by fermentation. Black vertical lines indicate changes in illumination intensity from 0 to 150, 50, 100, 25 and back to 0 mW/cm^2. (**D**) The data from C plotted in terms of speed against motile fraction. Error bars represent the SD among adjacent data points with the same illumination intensity.

4.4 Discussion

The light-independent increase in oxygen depletion rate by both PR and PoXeR was unexpected. Light-independent effects of PR have previously been reported by Song et al (2019) who observed light-independent benefits of PR on the long-term viability of *E. coli*. This seems somewhat counterintuitive, as we have just observed that PR can increase oxygen depletion rate, which sounds like a negative effect. They theorise that the increased viability could be due to PR physically stabilising the membrane through intermolecular contacts, but does oxygen consumption potentially play a role in this increased viability?

It has been observed that respiration in stationary phase causes cell damage (Cesar et al, 2022a) and induces dormancy as ATP levels decrease (Pu et al, 2019), and that respiration after sudden depletion of nutrients leads to cytoplasmic shrinkage and cell lysis (Cesar et al, 2022b). Respiration is known to be a major source of reactive oxygen species (ROS), which can damage the cell membrane, DNA and proteins (Kussmaul & Hirst, 2006). Though respiration enables the fastest growth, the cell needs to spend additional resources to avoid the damage from ROS. Correspondingly, one of the effects of the stringent response triggered by nutrient depletion is the inhibition of respiration (Smirnova et al, 2018). Smirnova et al (2018) theorise that an increase in PMF can prolong the duration of the respiration pathway, increasing the chance of ROS generation.

Thus, leakage of protons through PoXeR and PR could decrease the PMF independent of nutrient depletion, increasing the rate of respiration while reducing ROS generation per reaction. Further, if respiration is not the sole carbon sink, a faster respiration rate will consume more of the oxygen before it becomes poisonous

due to lack of nutrients. It is worth noting that Song et al (2019) only mixed the cells once every 2 days, meaning that the cells probably underwent a series of oxygen depletion events and spent most of their time in anaerobic conditions. This means that oxygen is limited, and an increased respiration rate will shorten the duration of aerobic conditions rather than increase the total amount of respiration.

Another possible explanation for the increased viability relates to lipid transport. Increasing the rate of lipid transport from the inner to the outer membrane was found to accelerate the cytoplasmic shrinkage and cell lysis caused by sudden nutrient depletion (Sutterlin et al, 2016), while inhibiting the transport delayed lysis (Grimm et al, 2020). Grimm et al (2020) speculated this transport to be diffusive, meaning the rate of transport would be slowed down by membrane crowding (Frick et al, 2007).

It has been said that a typical cell membrane contains 30,000 proteins per μm^2 (Guigas & Weiss, 2016). Whether or not this number is accurate for *E. coli*, the 40,000 PR per μm^2 that Song et al (2019) expressed take up 47% of the surface area of the cell membrane, enough to significantly increase membrane crowding. Hence, the increased viability could be the result of decreased lipid transport due to membrane crowding. Or, perhaps, this high content of inactive membrane proteins helps soak up the damage from ROS that are generated near the membrane, and since they have no specific function in the dark, it may neutralise ROS without losing any important functionality.

In any case, why do PR and PoXeR increase oxygen depletion rate in a light-independent manner? The most intuitive answer would have been that PMF homeostasis increases oxygen consumption rate to counter the inward proton pumping by PoXeR. However, further experiments revealed that both PR and

PoXeR, with and without light caused the same increase in respiration rate. Perhaps the increased membrane protein content significantly increased membrane permeability, as previously observed by Dilger et al (1979), especially since these proteins have a path for protons to pass through. Leakage of protons through the pumps at high PMF seems reasonable considering that respiration generates a PMF higher than the maximum PMF that PR can generate. But for PoXeR to have the same effect with and without light, the leakage at high PMF must be higher than the active pumping powered by light. Indeed, looking at the biophysical characteristics of PoXeR, its photocycle appears to be 91 seconds long, meaning each protein can pump a proton once every 91 seconds (Inoue et al, 2016). Given the slow pumping, a lower energetic state may be more permissive to testing whether active proton pumping can increase the metabolic rate of the cell, such as endogenous metabolism where the cell appears to counter PoXeR activity (Figure 4.10 A). The use of stronger pumps or channelrhodopsins could still yield light-dependent changes in respiration rate.

Chapter 5

Conclusions and future work

The development of optogenetic tools have allowed precise spatiotemporal control of various biological processes, such as gene expression, protein activity and neural signalling, and have been vital parts of various research and biotechnological applications. To expand the optogenetic toolkit with the ability to control the bacterial physiology surrounding cell energetics, the aim of this work was to characterise the expression of different microbial rhodopsins in wild-type *E. coli* and their effects on cell energetics and physiology in different conditions.

While the expression of non-bacterial rhodopsins is easier in B-strains engineered for exogenous protein expression, strong expression in wild-type *E. coli* was exclusive to the bacterial rhodopsins of this work. The difficulty of expression likely stems from the added structural complexity of the non-bacterial rhodopsins that may require a specific intracellular environment, such as the presence of glycosylation, for efficient folding. Though it may be possible to achieve expression through strain engineering or as a fusion protein with a highly expressing membrane protein (Tu et al, 2018), the number of known bacterial rhodopsins is constantly

increasing, and the modification of the biophysical characteristics of existing rhodopsins through protein engineering is possible. For the sake of future applications, it is better and likely faster to find a rhodopsin that was evolved in bacteria than to modify bacteria to accommodate non-bacterial rhodopsins. While proteorhodopsin (PR) works well for the manipulation of proton motive force (PMF) in non-respiring cells, *Parvularcula oceani* xenorhodopsin (PoXeR) was able to decrease the PMF of fermenting cells by only 23% on the account of its long 91 s photocycle (Inoue et al, 2016), limiting it to pumping only one proton per 91 s per molecule.

For future studies involving inward proton pumping, I would investigate other rhodopsins in the xenorhodopsin or schizorhodopsin family. Schizorhodopsins are light-driven inward proton pumps with putative photocycles as short as 3.4 ms, currently only discovered in archaea but have been expressed in B-strain *E. coli* (Inoue et al, 2020). Xenorhodpsins are also predominantly found in archaea, but like PoXeR, *Rubricoccus marinus* xenorhodopsin is another bacterial xenorhodopsin with a putative photocycle of 2.1 s (Inoue et al, 2018), being significantly faster than PoXeR. To expand the toolkit beyond proton pumps, the marine bacterium *Nonlabens marinus* strain S1-08^{T} has been found to contain an outward Na^{+} pump and an inward Cl^{-} pump that have been expressed in B-strain *E. coli* (Yoshizawa et al, 2014). As for light-gated ion channels, all currently known natural channelrhodopsins originate from eukaryotes, mostly algae, and are thus of limited utility in bacterial systems. There are, however, a limited number of channelrhodopsins that have been expressed in B-strain *E. coli*. *Guillardia theta* anion channelrhodopsin-2 is such light-gated algal anion channel (Doi et al, 2017), while ChrimsonR, a derivative of Chrimson (cation channel), appears to have been

successfully expressed in B-strain *E. coli* during the 2023 International Genetically Engineered Machine (iGEM) competition (Blaise et al, 2023). Although the light-driven outward proton pump Archaerhodopsin-3 (Arch or AR3) is from *Halorubrum sodomense*, an archaeon, just three mutations were enough to convert it into a light-gated proton channel that can be expressed in B-strain *E. coli* (Inoue et al, 2015), demonstrating the possibility of engineering a bacterial channelrhodopsin that can express in wild-type *E. coli*.

Overall, I learned several things about the optogenetic control of cell energetics and about cell physiology. It has been previously reported that PR cannot increase the PMF in respiring cells and hypothesised that PR does not pump protons in this condition because the energy required to pump a proton against the high PMF is larger than the free energy from photon absorption (Walter et al, 2007). I confirmed that not only does PR not increase PMF, but it also does not seem to participate maintaining the existing PMF and lessen the burden on respiration by doing so. Unexpectedly, PoXeR did not display any signs of light-driven proton pumping in respiring cells either, showing neither a direct effect on PMF nor a light-dependent effect on respiration rate. However, both PR and PoXeR seem to cause a light-independent increase in respiration rate. This may be a homeostatic response to maintain a constant PMF in response to proton leakage through the rhodopsins, or perhaps the rate of respiration is limited by PMF or the local proton concentration, both of which a change in proton leakage would affect. An interesting future experiment would be to test if a stronger inward proton pump or an ion channel could induce a higher ion current than the suspected leakage, and consequently cause a light-dependent increase in respiration rate. Further, I would test if the rhodopsins can affect the cells' fermentation rate by measuring glucose depletion rate. These

would allow us to control the energy efficiency of the cell in their respective conditions, and to probe the capacity of the homeostatic system to maintain PMF in different conditions.

Going down in energy levels, PoXeR could not maintain a stable decrease in PMF in cells undergoing endogenous metabolism, but was able to decrease PMF for a short duration, accompanied by a decrease in the proportion of motile cells that, unlike PMF, did not recover during illumination. The lower energy level of fermenting cells allowed PoXeR to display a 23% light-dependent PMF decrease at the highest illumination intensity, while nutrient-depleted cells are already below the detection threshold of my method. In contrast, PR displays the largest light-dependent effect in nutrient-depleted cells. While it was already known that PR cannot increase PMF in respiring cells (Walter et al, 2007), I showed that PR-driven PMF does not benefit from the additional PMF generation of fermenting compared to nutrient-depleted cells, consistent with the theory that PR stops pumping protons above a certain PMF.

The dynamics of reaching equilibria in my experiments were particularly interesting. Activating PR for the second time, after a 7-minute pause in illumination, caused the cells to reach the previous PMF significantly faster than the first time, suggesting that the slow increase in PMF, that does not plateau even after 60 minutes of illumination, depends on cellular processes rather than the duration of PR illumination. Extending the pause in illumination to 60 minutes results in an opposite effect, where swimming speed accelerates slower and to a lower maximum speed (Arlt et al, 2018), more in line with my results where sample age reduces the swimming speed of the cells. These could be different processes that act on different time scales, or perhaps the decrease after 60 minutes is due to stator dissociation.

Stator units are the parts of the flagellar motor that couple proton flow to rotation, and extended periods of PMF depletion have been shown to lead to the dissociation of stators from the motor (Tipping et al, 2012). In my experiments, the duration of PMF depletion before the first and second illumination is the same, whereas Arlt et al (2018) keep the cells PMF-depleted significantly longer before the second illumination, which could lead to a slower recovery of flagellar motor integrity.

Reaching the PMF equilibrium in dimly illuminated PR-expressing nutrient-depleted cells is fast from a low energy state but slow from a high energy state, shedding light on the proton pumping dynamics of the cell in low PMF. I hypothesise that the combined proton pumping by PR and ATP-hydrolysing F_1F_o ATP synthase sustain PMF at a higher level and deplete ATP slower than in the absence of PR activity. This could be tested using a strain lacking the F_1F_o ATP synthase, such as in Arlt et al (2018). Finally, the way illumination of PoXeR-expressing cells overshoots and then returns to equilibrium PMF suggests that homeostatic activity responds to the decreased PMF caused by inward proton pumping.

There is still much to learn from the light-driven manipulation of ion motive forces. For instance, how long can PMF be maintained by PR, and when it starts to decrease, which components of the cell are failing? Much research has focused on the role of PR in its native hosts, and while it seems its proton pumping often does not confer a growth advantage (Giovannoni et al, 2005), in some conditions it can increase the host's growth rate slightly (Chen et al, 2019). Less is known about the effect of heterogenous expression of PR in non-phototrophic bacteria like *E. coli* on its growth rate, but a 10% growth advantage during the first three hours has been demonstrated in respiration-incapable *E. coli* grown in minimal medium with lactate (Wang et al, 2015). This should be investigated further: are there conditions where

light can confer a larger increase in growth rate that remains stable for more than three hours? And how does this growth benefit affect the competitive fitness of the cell, essential for evolution experiments? Further, why do some cells seem to be able to recover their swimming speed while others become non-motile? Studying optogenetic manipulation of cell energetics on single-cell level can shed light on this from a different angle. Although oxygen depletion via cell consumption was not viable for tethered cell assay, there are alternative ways with different limitations, for instance, using nitrogen to remove oxygen before the experiment or using azide to block respiration (Walter et al, 2007). Finally, it would be interesting to combine optogenetic manipulation of energetics with various sensors measuring other physiological parameters such as ATP, membrane potential or a secondary ion not directly controlled by the rhodopsin.

Appendix A

DNA sequences

A.1 PCR primers

Table A.1: A list of PCR primers used to generate the fragments for plasmid construction. Upper- and lower-case letters represent complementary and non-complementary bases, respectively. Only the final, successful primers are listed.

Fragment	Forward primer	Reverse primer	Annealing temperature
PR	ggacatatac atATGGGTAA ATTATTACTG ATATTAGGTA GTG	attaccggat cCTCAATGGT GATGGTGATG ATG	62°C
PoXeR	CTTCCCCATC GGTGATGTCG GCGATA	atcaccggat ccttaCTCGA GCACCGGGCG TTCCA	72°C
ArchT	atacatATGG ACCCCATCGC TCTGCA	accggatcct tatGGtTCtG GtGCtTCGGT GTCGCCCAGG ATGG	69°C

NpHR	gatatacata tgACTGAGAC CCTCCCACCC GTG	attaccggat ccttaaTCAT CtGCtGGTGT GCCGCTGGCG GAT	71°C
ChEF	AGGATCCACC GGTGcatATG GTGAGCAGAA G	atcaccggat ccttaGCTGC TCTCGTACTT GCCGGT	70°C
ChIEF	CTAGCAAGGA TCCGcatATG GTGAGCAGAA GA	atcaccggat ccttaGCTGC TCTCGTACTT GCCGGT	70°C
Chrimson	ggacatatac atATGGCaGA aCTGATCAGC AGCGCCACCA GA	attaccggat ccttaCACTG TGTCCTCGTC CTCCTCCTC	70°C
pWR20 backbone	TGAGGATCCG GTGATTGATT	AGCCATATGT ATATCTCCTT AACTAGG	61°C

A.2 Plasmids

Table A.2: A list of plasmids with a link to their corresponding annotated plasmid maps. Addgene plasmids can be found using their plasmid numbers provided in Table 2.1.

Plasmid	Link to plasmid map
pBAD-PR	http://tinyurl.com/pBAD-PR
pET21a-PoXeR	http://tinyurl.com/pET21a-PoXeR
pWR20	http://tinyurl.com/pWR20-GFP
pWR20-PR	http://tinyurl.com/pWR20-PR
pWR20-PoXeR	http://tinyurl.com/pWR20-PoXeR

pWR20-ArchT	http://tinyurl.com/pWR20-ArchT
pWR20-NpHR	http://tinyurl.com/pWR20-NpHR
pWR20-ChEF	http://tinyurl.com/pWR20-ChEF
pWR20-ChIEF	http://tinyurl.com/pWR20-ChIEF
pWR20-Chrimson	http://tinyurl.com/pWR20-Chrimson

A.3 IS1 transposase sequence

The following DNA sequence created a superimposed signal on the chromatogram of NpHR starting shortly before the start codon (Figure 3.11). Since I compiled it manually from a noisy chromatogram, there may be some errors compared to the real DNA sequence.

GGTGATGCTG CCAACTTCCT GATTTAGTGT ATGATGGTGT TTTTGAGGTG CTCCAGTGGC TTCTTGTTTC TATCAGCTGT CCCTCCTGTT CAGCTACTGA CGGGGTGGTG CGTAACGGCA AAAGCACCGC CGGACATCAG CGCTATCTCT GCTCTCACTG CCGTAAAACA TGGCAACTGC AGTTCACTTA CACCGCTTCT CAACCCGGTA CGCACCAGAA AATCATTGAT ATGGCCATGA ATGGCGTTGG ATGCCGGGCA ACAGCCCGCA TTATGGGCGT TGGCCTCAAC ACGATTTTAC GTCACTTAAA AAACTCAGGC CGCAGTCGGT AACTCGCGCA TACAGCCGGG CAGTGACGTC ATCGTCTGCG CGGAAATGGA CGAACAGTGG GGCTATGTCG GGGCTAAATC GCGCCAACGC TGGCTGTTTT ACGCGTATGA CAGTCTCCGG AAGACGGTTG TTGCGCACGT ATTCGGTGAA CGCACTATGG CGACGCTGGG GCGTCTTATG AGCCTGCTGT CACCCTTTGA CGTGGTGATA TGGATGACGG

ATGGCTGGCC GCTGTATGAA TCCCGCCTGA AGGAAAAGCT GCACGTAATC AGCAAGCGAT ATACGCACGG AATTTG

Appendix B

Code

Table B.1: A list of software developed for this project.

Purpose	Link to code
Cell tracking for tethered cell assay	https://github.com/tsSchmidi/Cell_tracker
Analysis of DDM output	https://github.com/tsSchmidi/DDM-summary
Analysis of absorption spectra	https://github.com/tsSchmidi/Absorption-spectra
Analysis of growth curves	https://github.com/tsSchmidi/Growth-curves
Simulating establishment probability	https://github.com/tsSchmidi/Establishment-probability

Bibliography

Ahmad P & Bano F (2019) Chapter 12 – Posttranslational Modifications in Algae: Role in Stress Response and Biopharmaceutical Production. In Protein Modificomics p 313–337. Academic Press.

Arlt J, Martinez V, Dawson A, et al (2018) Painting with light-powered bacteria. *Nature Communications* 9:768.

Arlt J, Martinez V, Dawson A, et al (2019) Dynamics-dependent density distribution in active suspensions. *Nature Communications* 10:2321.

Balch W, Morimoto R, Dillin A, et al (2008) Adapting proteostasis for disease intervention. *Science* 319:916–919.

Bamann C, Bamberg E, Wachtveitl J, et al (2014) Proteorhodopsin. *Biochimica et Biophysica Acta (BBA) - Bioenergetics* 1837:614–625.

Baym M, Lieberman T, Kelsic E, et al (2016) Spatiotemporal microbial evolution on antibiotic landscapes. *Science* 353:1147–1151.

Béjà O, Aravind L, Koonin E, et al (2000) Bacterial rhodopsin: Evidence for a new type of Phototrophy in the sea. *Science* 289:1902–1906.

Berg J, Tymoczko J & Stryer L (2002) Section 18.4 - A Proton Gradient Powers the Synthesis of ATP. In *Biochemistry* 5th ed. New York: W.H. Freeman.

Bisschop K, Mortier F, Etienne R, et al (2019) Transient local adaptation and source–sink dynamics in experimental populations experiencing spatially heterogeneous environments. *Proceedings of the Royal Society B* 286:20190738.

Bivin D & Stoeckenius W (1986) Photoactive retinal pigments in Haloalkaliphilic Hacteria. *Microbiology* 132:2167–2177.

Blaise D, et al (2023) ChrimsonR expression cassette in the Evolution.T7 mutational region. *iGEM Registry of Standard Biological Parts*. Available at: https://parts.igem.org/Part:BBa_K4601201 [Accessed December 30, 2023].

Cantón R & Morosini M-I (2011) Emergence and spread of antibiotic resistance following exposure to antibiotics. *FEMS Microbiology Reviews* 35:977–991.

Cayron J, Dedieu-Berne A & Lesterlin C (2023) Bacterial filaments recover by successive and accelerated asymmetric divisions that allow rapid post-stress cell proliferation. *Molecular Microbiology* 119:237–251.

Cesar S, Willis L & Huang K (2022a) Bacterial respiration during stationary phase induces intracellular damage that leads to delayed regrowth. *iScience* 25:103765.

Cesar S, Sun J, Huang K (2022b) Cellular memory of rapid growth is sensitive to nutrient depletion during starvation. *Frontiers in Microbiology* 13.

Chen Q, Arents J, Schuurmans J, et al (2019) Combining retinal-based and chlorophyll-based (oxygenic) photosynthesis: Proteorhodopsin expression increases growth rate and fitness of a ΔPSI strain of *Synechocystis* sp. PCC6803. *Metabolic Engineering* 52:68–76.

Chen X & Berg H (2000) Torque-Speed Relationship of the Flagellar Rotary Motor of *Escherichia coli*. *Biophysical journal* 78:1036–1041.

Chumpolkulwong N, Sakamoto K, Hayashi A, et al (2006) Translation of ‘rare’ Codons in a Cell-free Protein Synthesis System from *Escherichia coli*. *Journal of Structural and Functional Genomics* 7:31–36.

Cremer J, Honda T, Tang Y, et al (2019) Chemotaxis as a navigation strategy to boost range expansion. *Nature* 575:658–663.

Deisseroth K & Hegemann P (2017) The form and function of Channelrhodopsin. *Science* 357:eaan5544.

Deng Y, Beahm D, Ionov S, et al (2021) Measuring and modeling energy and power consumption in living microbial cells with a synthetic ATP reporter. *BMC Biology* 19:101.

Dibrov P, Lazarova R, Skulachev V, et al (1986) The sodium cycle. II. Na+-coupled oxidative phosphorylation in *Vibrio alginolyticus* cells. *Biochimica et Biophysica Acta (BBA) - Bioenergetics* 850:458–465.

Dilger J, McLaughlin S, McIntosh T, et al (1979) The dielectric constant of phospholipid bilayers and the permeability of membranes to ions. *Science* 206:1196–1198.

Doi S, Tsukamoto T, Yoshizawa S, et al (2017) An inhibitory role of ARG-84 in anion channelrhodopsin-2 expressed in *Escherichia coli*. *Scientific Reports* 7:41879.

Foster K, Saranak J, Patel N, et al (1984) A rhodopsin is the functional photoreceptor for phototaxis in the unicellular eukaryote *Chlamydomonas*. *Nature* 311:756–759.

Frangipane G, Dell'Arciprete D, Petracchini S, et al (2018) Dynamic density shaping of photokinetic *E. coli*. *eLife* 7:e36608.

Frenoy A & Bonhoeffer S (2018) Death and population dynamics affect mutation rate estimates and evolvability under stress in bacteria. *PLOS Biology* 16:e2005056.

Frick M, Schmidt K & Nichols B (2007) Modulation of lateral diffusion in the plasma membrane by protein density. *Current Biology* 17:462–467.

Fung D & Berg H (1995) Powering the flagellar motor of *Escherichia coli* with an external voltage source. *Nature* 375:809–812.

Gabel C & Berg H (2003) The speed of the flagellar rotary motor of Escherichia coli varies linearly with protonmotive force. *Proceedings of the National Academy of Sciences* 100:8748–8751.

Giovannoni S, Bibbs L, Cho J-C, et al (2005) Proteorhodopsin in the ubiquitous marine bacterium SAR11. *Nature* 438:82–85.

Gonzalez A, Ronce O, Ferriere R, et al (2013) Evolutionary rescue: an emerging focus at the intersection between ecology and evolution. *Philosophical Transactions of the Royal Society B* 368:20120404.

Grimm J, Shi H, Wang W, et al (2020) The inner membrane protein YhdP modulates the rate of anterograde phospholipid flow in *Escherichia coli*. *Proceedings of the National Academy of Sciences* 117:26907–26914.

Guigas G & Weiss M (2016) Effects of protein crowding on membrane systems. *Biochimica et Biophysica Acta (BBA) – Biomembranes* 1858:2441–2450.

Guyer M, Reed R, Steitz J, et al (1981) Identification of a sex-factor-affinity site in E. coli as gamma delta. *Cold Spring Harbor Symposia on Quantitative Biology* 45:135–140.

Han X, Qian X, Stern P, et al (2009) Informational lesions: Optical perturbation of spike timing and neural synchrony via microbial opsin gene fusions. *Frontiers in Molecular Neuroscience* 2:12.

Han X, Chow B, Zhou H, et al (2011) A high-light sensitivity optical neural silencer: development and application to optogenetic control of non-human primate cortex. *Frontiers in Systems Neuroscience* 5:18.

Hermsen R, Deris J & Hwa T (2012) On the rapidity of antibiotic resistance evolution facilitated by a concentration gradient. *Proceedings of the National Academy of Sciences* 109:10775–10780.

Heyes D (2019) Translational and rotational diffusion of rod shaped molecules by molecular dynamics simulations. *The Journal of Chemical Physics* 150:184503.

Honda T, Cremer J, Mancini L, et al (2022) Coordination of gene expression with cell size enables *Escherichia coli* to efficiently maintain motility across conditions. *Proceedings of the National Academy of Sciences* 119:e2110342119.

Hunke S, Betton J-M (2003) Temperature effect on inclusion body formation and stress response in the periplasm of *Escherichia coli*. *Molecular Microbiology* 50:1579–1589.

Inoue K, Tsukamoto T, Shimono K, et al (2015) Converting a light-driven proton pump into a light-gated proton channel. *Journal of the American Chemical Society* 137:3291–3299.

Inoue K, Ito S, Kato Y, et al (2016) A natural light-driven inward proton pump. *Nature Communications* 7:13415.

Inoue S, Yoshizawa S, Nakajima Y, et al (2018) Spectroscopic characteristics of *Rubricoccus marinus* xenorhodopsin (RmXeR) and a putative model for its inward H^+ transport mechanism. *Physical Chemistry Chemical Physics* 20:3172–3183.

Inoue K, del Carmen Marín M, Tomida S, et al (2019) Red-shifting mutation of light-driven sodium-pump rhodopsin. *Nature Communications* 10:1993.

Inoue K, Tsunoda S, Singh M, et al (2020) Schizorhodopsins: A family of rhodopsins from Asgard archaea that function as light-driven inward H^+ pumps. *Science Advances* 6:eaaz2441.

Irving S, Choudhury N & Corrigan R (2020) The stringent response and physiological roles of (pp)pGpp in bacteria. *Nature Reviews Microbiology* 19:256–271.

Jain R & Sebastian K (2017) Diffusing diffusivity: Rotational diffusion in two and three dimensions. *The Journal of Chemical Physics* 146:214102.

Jhamb K & Sahoo D (2012) Production of soluble recombinant proteins in *Escherichia coli*: Effects of process conditions and chaperone co-expression on cell growth and production of xylanase. *Bioresource Technology* 123:135–143.

Jumper J, Evans R, Pritzel A, et al (2021) Highly accurate protein structure prediction with AlphaFold. *Nature* 596:583–589.

Kikuchi M, Kojima K, Nakao S, et al (2021) Functional expression of the eukaryotic proton pump rhodopsin OMR2 in *Escherichia coli* and its photochemical characterization. *Scientific Reports* 11:14765.

Kim J, Jo B, Jo Y, et al (2012) Improved production of biohydrogen in light-powered *Escherichia coli* by co-expression of proteorhodopsin and heterologous hydrogenase. *Microbial Cell Factories* 11.

Klapoetke N, Murata Y, Kim S, et al (2014) Independent optical excitation of distinct neural populations. *Nature Methods* 11:338–346.

Kojima K & Sudo Y (2023) Convergent evolution of animal and microbial rhodopsins. *RSC Advances* 13:5367–5381.

Krasnopeeva E, Lo C-J & Pilizota T (2019) Single-cell bacterial electrophysiology reveals mechanisms of stress-induced damage. *Biophysical Journal* 116:2390–2399.

Kudrin P, Dzhygyr I, Ishiguro K, et al (2018) The ribosomal A-site finger is crucial for binding and activation of the stringent factor RelA. *Nucleic Acids Research* 46:1973–1983.

Kuniyoshi T, Balan A, Schenberg A, et al (2015) Heterologous expression of proteorhodopsin enhances H2 production in *Escherichia coli* when endogenous HYD-4 is overexpressed. *Journal of Biotechnology* 206:52–57.

Kussmaul L & Hirst J (2006) The mechanism of superoxide production by NADH:ubiquinone oxidoreductase (complex I) from bovine heart mitochondria. *Proceedings of the National Academy of Sciences* 103:7607–7612.

Kühlbrandt W (2016) Three in a row—how sodium ions cross the channel. *The EMBO Journal* 35:793–795.

Le J (2019) Drug Distribution to Tissues. *MSD Manual Professional Edition*. Available at: https://www.msdmanuals.com/en-gb/professional/clinical-pharmacology/pharmacokinetics/drug-distribution-to-tissues [Accessed November 30, 2023].

Lin W-H & Jacobs-Wagner C (2022) Connecting single-cell ATP Dynamics to overflow metabolism, cell growth, and the cell cycle in *Escherichia coli*. *Current Biology* 32:3911–3924.e4.

Lin J, Lin M, Steinbach P, et al (2009) Characterization of engineered channelrhodopsin variants with improved properties and kinetics. *Biophysical Journal* 96:1803–1814.

Lindsey H, Gallie J, Taylor S, et al (2013) Evolutionary rescue from extinction is contingent on a lower rate of environmental change. *Nature* 494:463–467.

Loveland A, Bah E, Madireddy R, et al (2016) Ribosome•RelA structures reveal the mechanism of stringent response activation. *eLife* 5:e17029.

Magariyama Y, Sugiyama S, Muramoto K, et al (1995) Simultaneous measurement of bacterial flagellar rotation rate and swimming speed. *Biophysical Journal* 69:2154–2162.

Mancini L & Pilizota T (2023) Environmental conditions define the energetics of bacterial dormancy and its antibiotic susceptibility. *Biophysical Journal* 122:3207–3218.

Mao F & Leung W (2015) *Methods of using dyes in association with nucleic acid staining or detection and associated technology*. United States patent US9102835B2.

Martinez V, Besseling R, Croze O, et al (2012) Differential Dynamic Microscopy: A high-throughput method for characterizing the motility of Microorganisms. *Biophysical Journal* 103:1637–1647.

McIsaac R, Engqvist M, Wannier T, et al (2014) Directed evolution of a far-red fluorescent rhodopsin. *Proceedings of the National Academy of Sciences* 111:13034–13039.

Method of the Year 2010 (2010) *Nature Methods* 8:1.

Meyrat A & von Ballmoos C (2019) ATP synthesis at physiological nucleotide concentrations. *Scientific Reports* 9:3070.

Michels P, Michels J, Boonstra J, et al (1979) Generation of an electrochemical proton gradient in bacteria by the excretion of metabolic end products. *FEMS Microbiology Letters* 5:357–364.

Moriya H (2015) Quantitative nature of overexpression experiments. *Molecular Biology of the Cell* 26:3932–3939.

Moser C & Bell G (2010) Genetic correlation in relation to differences in dosage of a stressor. *Journal of Evolutionary Biology* 24:219–223.

Mouery K, Rader B, Gaynor E, et al (2006) The stringent response is required for *Helicobacter pylori* survival of stationary phase, exposure to acid, and aerobic shock. *Journal of Bacteriology* 188:5494–5500.

Muir J & Bagot R (2019) Chapter 14 – Optogenetics: Illuminating the Neural Circuits of Depression. In Neurobiology of Depression p 147–157. Academic Press.

Nagel G, Brauner M, Liewald J, et al (2005) Light activation of channelrhodopsin-2 in excitable cells of Caenorhabditis elegans triggers rapid behavioral responses. *Current Biology* 15:2279–2284.

Nagel G, Szellas T, Huhn W, et al (2003) Channelrhodopsin-2, a directly light-gated cation-selective membrane channel. *Proceedings of the National Academy of Sciences* 100:13940–13945.

NEB (n.d.) Cleavage Close to the End of DNA Fragments. Available at: https://international.neb.com/tools-and-resources/usage-guidelines/cleavage-close-to-the-end-of-dna-fragments [Accessed September 13, 2023].

Nedeljković M, Sastre D & Sundberg E (2021) Bacterial flagellar filament: A supramolecular multifunctional nanostructure. *International Journal of Molecular Sciences* 22:7521.

Neidhardt F, Bloch P & Smith D (1974) Culture Medium for Enterobacteria. *Journal of Bacteriology* 119:736–747.

Noumi T, Maeda M & Futai M (1987) Mode of inhibition of sodium azide on H^+-ATPase of *Escherichia coli*. *FEBS Letters* 213:381–384.

Oda K, Vierock J, Oishi S, et al (2018) Crystal structure of the red light-activated channelrhodopsin Chrimson. *Nature Communications* 9:3949.

Omnus D, Fink M, Kallazhi A, et al (2022) The heat shock protein LarA activates the Lon protease at the onset of proteotoxic stress. *bioRxiv* 2022.10.10.511565.

Perron G, Gonzalez A & Buckling A (2007) Source–sink dynamics shape the evolution of antibiotic resistance and its pleiotropic fitness cost. *Proceedings of the Royal Society B* 274:2351–2356.

Pilizota T & Shaevitz J (2012) Fast, multiphase volume adaptation to hyperosmotic shock by Escherichia coli. *PLoS ONE* 7:e35205.

Pinner E, Padan E & Schuldiner S (1992) Cloning, sequencing, and expression of the nhaB gene, encoding a Na+/H+ antiporter in Escherichia coli. *Journal of Biological Chemistry* 267:11064–11068.

Pu Y, Li Y, Jin X, et al (2019) ATP-dependent dynamic protein aggregation regulates bacterial dormancy depth critical for antibiotic tolerance. *Molecular Cell* 73:143–156.e4.

Qian C, Wong C, Swarup S, et al (2013) Bacterial tethering analysis reveals a “run-reverse-turn” mechanism for pseudomonas species motility. *Applied and Environmental Microbiology* 79:4734–4743.

Radoš D, Donati S, Lempp M, et al (2022) Homeostasis of the biosynthetic *E. coli* metabolome. *iScience* 25:104503.

Rosano G & Ceccarelli E (2009) Rare codon content affects the solubility of recombinant proteins in a codon bias-adjusted *Escherichia coli* strain. *Microbial Cell Factories* 8:41.

Rosano G & Ceccarelli E (2014) Recombinant protein expression in *Escherichia coli*: advances and challenges. *Frontiers in Microbiology* 5.

Roy P, Laprise R & Gachon P (2016) Sampling errors of quantile estimations from finite samples of data. *arXiv*. Available at: https://doi.org/10.48550/arXiv.1610.03458 [Accessed December 30, 2023].

Royant A, Nollert P, Edman K, et al (2001) X-ray structure of sensory rhodopsin II at 2.1-Å Resolution. *Proceedings of the National Academy of Sciences* 98:10131–10136.

Rusch D, Halpern A, Sutton G, et al (2007) The Sorcerer II Global Ocean Sampling Expedition: Northwest Atlantic through Eastern Tropical Pacific. *PLoS Biology* 5:e77.

Schneider D & Gourse R (2004) Relationship between growth rate and ATP concentration in *Escherichia coli*. *Journal of Biological Chemistry* 279:8262–8268.

Schwarz-Linek J, Arlt J, Jepson A, et al (2016) *Escherichia coli* as a model active colloid: A practical introduction. *Colloids and Surfaces B: Biointerfaces* 137:2–16.

Scott M, Gunderson C, Mateescu E, et al (2010) Interdependence of cell growth and gene expression: Origins and consequences. *Science* 330:1099–1102.

Sezonov G, Joseleau-Petit D & D’Ari R (2007) *Escherichia coli* physiology in Luria-Bertani broth. *Journal of Bacteriology* 189:8746–8749.

Shental-Bechor D & Levy Y (2008) Effect of glycosylation on protein folding: A close look at thermodynamic stabilization. *Proceedings of the National Academy of Sciences* 105:8256–8261.

Silverman M & Simon M (1974) Flagellar rotation and the mechanism of bacterial motility. *Nature* 249:73–74.

Shirano Y & Shibata D (1990) Low temperature cultivation of *Escherichia coli* carrying a rice lipoxygenase L-2 cDNA produces a soluble and active enzyme at a high level. *FEBS Letters* 271:128–130.

Smirnova G, Tyulenev A, Muzyka N, et al (2018) The sharp phase of respiratory inhibition during amino acid starvation in *Escherichia coli* is RelA-dependent and associated with regulation of ATP synthase activity. *Research in Microbiology* 169:157–165.

Song Y, Cartron M, Jackson P, et al (2019) Proteorhodopsin overproduction enhances the long-term viability of *Escherichia coli*. *Applied and Environmental Microbiology* 86:e02087–19.

Stock G (1978) The measurement of bacterial translation by photon correlation spectroscopy. *Biophysical Journal* 22:79–96.

Sutterlin H, Shi H, May K, et al (2016) Disruption of lipid homeostasis in the gram-negative cell envelope activates a novel Cell Death pathway. *Proceedings of the National Academy of Sciences* 113:E1565–E1574.

Terradot G, Krasnopeeva E, Swain P, et al (2021) The proton motive force determines *Escherichia coli*'s robustness to extracellular pH. *bioRxiv* 2021.11.19.469321.

Tipping M, Steel B, Delalez N, et al (2012) Quantification of flagellar motor stator dynamics through *in vivo* proton-motive force control. *Molecular Microbiology* 87:338–347.

Tsukamoto T, Sasaki T, Fujimoto K, et al (2012) Homotrimer Formation and dissociation of *pharaonis* Halorhodopsin in Detergent System. *Biophysical Journal* 102:2906–2915.

Trchounian K, Blbulyan S & Trchounian A (2012) Hydrogenase activity and Proton-motive force generation by *Escherichia coli* during glycerol fermentation. *Journal of Bioenergetics and Biomembranes* 45:253–260.

Tu C-H, Yi H-P, Hsieh S-Y, et al (2018) Overexpression of different types of microbial rhodopsins with a highly expressible bacteriorhodopsin from *Haloarcula marismortui* as a single protein in *E. coli*. *Scientific Reports* 8:14026.

Verstraeten N, Knapen W, Kint C, et al (2015) Obg and membrane depolarization are part of a microbial bet-hedging strategy that leads to antibiotic tolerance. *Molecular Cell* 59:9–21.

Vogt A, Silapetere A, Grimm C, et al (2019) Engineered Passive Potassium Conductance in the KR2 Sodium Pump. *Biophysical Journal* 116:1941–1951.

Walter J, Greenfield D, Bustamante C, et al (2007) Light-powering *Escherichia coli* with proteorhodopsin. *Proceedings of the National Academy of Sciences* 104:2408–2412.

Wang B, Dai P, Ding D, et al (2019) Affinity-based capture and identification of protein effectors of the growth regulator ppGpp. *Nature Chemical Biology* 15:141–150.

Wang Y, Li Y, Xu T, et al (2015) Experimental evidence for growth advantage and metabolic shift stimulated by photophosphorylation of proteorhodopsin expressed in *Escherichia coli* at anaerobic condition. *Biotechnology and Bioengineering* 112:947–956.

West I & Mitchell P (1974) The proton-translocating ATPase of *Escherichia coli*. *FEBS Letters* 40:1–4.

Wittmann T, Dema A & van Haren J (2020) Lights, cytoskeleton, action: Optogenetic control of cell dynamics. *Current Opinion in Cell Biology* 66:1–10.

Yoshizawa S, Kumagai Y, Kim H, et al (2014) Functional characterization of Flavobacteria rhodopsins reveals a unique class of light-driven chloride pump in bacteria. *Proceedings of the National Academy of Sciences* 111:6732–6737.

Zhuo J-M, Tseng H, Desai M, et al (2016) Young adult born neurons enhance hippocampal dependent performance via influences on Bilateral Networks. *eLife* 5:e22429.